

MASTER'S DISSERTATION

NUMERICAL STUDY OF COMPLEX FLUID-INTERFACE SYSTEMS: FROM IONIC SURFACTANT-COVERED DROPLETS TO ELECTROHYDRODYNAMIC PHENOMENA

Ву,

Juan Linhares Barbosa

Brasília, 28 de maio de 2025

UNIVERSITY OF BRASÍLIA

FACULTY OF TECHNOLOGY
Mechanical Sciences

UNIVERSITY OF BRASÍLIA FACULTY OF TECHNOLOGY Department of Mechanical Engineering

MASTER'S DISSERTATION

NUMERICAL STUDY OF COMPLEX FLUID-INTERFACE SYSTEMS: FROM IONIC SURFACTANT-COVERED DROPLETS TO ELECTROHYDRODYNAMIC PHENOMENA

Ву,

Juan Linhares Barbosa

In Partial Fulfillment of the Requirements for the Degree of Master in Mechanical Sciences

Examiners

Taygoara Felamingo de Oliveira, PhD - ENM/UnB (Supervisor)	
Rodrigo Bento Rebouças, PhD - ENM/UnB (Co-Supervisor)	
Alexandre Pereira dos Santos, PhD - IF/UFRGS, (External Examiner)	
Alysson Martins Silva, PhD - PPG-CM/UnB (Internal Examiner)	
Yuri Dumaresq Sobral,	
PhD - MAT/UnB (Internal Examiner) Adriano Possebon Rosa,	
PhD - ENM/UnB (Alternate Examiner)	

Brasília, 28 de maio de 2025

FICHA CATALOGRÁFICA

Barbosa, J. L.

Numerical Study of Complex Fluid-Interface Systems: From Ionic Surfactant-Covered Droplets to Electrohydrodynamic Phenomena

[Distrito Federal] 2025.

xxviii, 103p. (ENM/FT/UnB, Mestre, Ciências Mecânicas, 2025.

Master's Dissertation - University of Brasília - UnB Faculty of Technology .

Faculdade de Tecnologia.

Departamento de Engenharia Mecânica.

Palavras-chave:

1. Surfactant 2. Droplet

3. Surface Charge 4. Electrohydrodynamics

I. ENM/FT/UnB II. Título (série)

REFERÊNCIA BIBLIOGRÁFICA

Barbosa, J. L.(2025). Numerical Study of Complex Fluid-Interface Systems: From Ionic Surfactant-Covered Droplets to Electrohydrodynamic Phenomena. Master's Dissertation, Departamento de Engenharia Mecânica, University of Brasília - UnB

Faculty of Technology, Brasília, Distrito Federal, xxviii, 103p.

CESSÃO DE DIREITOS

NOME DO AUTOR: Juan Linhares Barbosa.

TÍTULO DA DISSERTAÇÃO DE MESTRADO: Numerical Study of Complex Fluid-Interface Systems: From Ionic Surfactant-Covered Droplets to Electrohydrodynamic Phenomena.

GRAU / ANO: MESTRE / 2025

É concedida à Universidade de Brasília permissão para reproduzir cópias desta dissertação de mestrado e para emprestar ou vender tais cópias somente para propósitos acadêmicos e científicos. O autor reserva outros direitos de publicação e nenhuma parte desta dissertação de mestrado pode ser reproduzida sem a autorização por escrito do autor.

Juan	Linhares	Barbosa		

Acknowledgements

I'm extremely grateful for all the people who were part of my master's journey. I'd like to start by thanking my supervisor, Prof. Taygoara Felamingo de Oliveira, the person who introduced me to the world of academic research and made my eyes shine since my undergraduate course, when he delighted me with his exceptional teaching ability, charisma, and guidance in my final thesis. Over these years, thank you for your support, understanding, and the opportunity to work alongside you.

I also thank my co-supervisor, Prof. Rodrigo Bento Rebouças, who began working with me remotely via online meetings, giving me constant feedback. I'm glad we met in person and collaborated at UnB these past seven months—your presence elevated my work immensely. Even though you're at a different academic level, we shared great times over coffees, macchiatos, and lunches at UnB's restaurant.

Special thanks to Prof. Paulo Henrique Neves Pimenta for sharing his numerical code and support, and to Prof. Yuri Dumaresq Sobral for teaching me the beauty of applied mathematics and numerical methods. You encouraged me to keep exploring research and teaching. Thank you, Prof. Ricardo da Cunha, for the intense learning in your classes—though brief, it left a mark. To all professors who shaped me: thank you.

To my friends and colleagues at UnB—Paulo Henrique, Leonardo, Kaajal, Arthur, Raysa, Tayná, Luis, Amanda, Nicolas, Jackson, Ramiro, and Filipe—thank you for the laughs, conversations, and coffee breaks.

My mother, Elizabeth Linhares, deserves endless gratitude for always pushing me to chase my dreams and caring for me my whole life. Thank you for every sacrifice, for giving me an education and a life worth living. To my girlfriend, Vitória Gomes—almost my fiancée—thank you for standing by me through highs and lows, loving me through it all. My godmother, Jane Ferreira, and her family in Brasília: your kindness made living alone easier.

I would also like to thank my friends and neighbors—Carmen, Carliene, Rita, Loreni, Ms. Graça, and Sônia—for their support, delicious food, and good conversations that provided much-needed distraction and warmth during this journey.

I express my sincere gratitude to Coordenação de Aperfeiçoamento de Pessoal de Nível Superior (Capes) and Conselho Nacional de Desenvolvimento Científico e Tecnológico (CNPq) for their financial support. The scholarships granted by these institutions were instrumental in making this academic journey possible and complete this master's program.

Resumo

Estudo numérico de interfaces líquidas complexas: de gotas recobertas por surfactantes iônicos a fenômenos eletro-hidrodinâmicos

Autor: Juan Linhares Barbosa

Orientador: Taygoara Felamingo de Oliveira, Prof. Dr., UnB

Coorientador: Rodrigo Bento Rebouças, Prof. Dr., UnB

Mestrado em Ciências Mecânicas

Brasília, 2025

A estabilidade e o controle de escoamento de emulsões são fundamentais para o design de produtos em diversas indústrias, como engenharia ambiental, recuperação de petróleo, indústria alimentícia e farmacêutica. A estabilidade de emulsões depende de fenômenos interfaciais, nos quais surfactantes iônicos—moléculas anfifílicas com grupos eletricamente carregados—desempenham um papel crucial ao se adsorverem nas interfaces de gotas, reduzindo a tensão superficial e proporcionando repulsão eletrostática o que pode evitar a coalescência. Esses surfactantes se redistribuem na interface das gotas sob escoamento, acoplando o balanço de forças na interface com mecanismos de transporte de carga. Este estudo investiga dois aspectos interconectados da eletrohidrodinâmica de gotas: (1) o efeito da carga e do campo elétrico dos surfactantes iônicos na dinâmica de gotas sob ação de escoamentos de cisalhamento simples, e (2) a resposta eletrohidrodinâmica de gotas sob campos elétricos aplicados, com foco na advecção de carga e no regime de eletrorotação.

Na primeira parte, exploramos por meio de simulações numéricas gotas cobertas por surfactantes em cisalhamento simples, empregando uma metodologia unificada que integra efeitos elétricos e hidrodinâmicos. Uma metodologia numérica acoplada combina o método de projeção para resolver as equações de Navier-Stokes, a técnica de Level-Set para capturar a interface e o método do *Closest Point* para resolver a equação de transporte de surfactante. Essa abordagem captura a competição entre advecção induzida pelo cisalhamento, difusão de surfactante e eletro-migração de íons na interface da gota. Demonstramos que a deformação da gota é ditada pelo número de Mason (razão entre forças viscosas e elétricas), pela razão de mobilidade (eficiência do transporte de carga), pelo número de Peclet (razão entre transporte advectivo e difusivo), pela cobertura de surfactante e pelo

parâmetro de elasticidade da interface. A densidade de carga superficial, linearmente dependente da concentração de surfactante, leva ao acúmulo de carga em regiões de alta curvatura via advecção do escoamento, enquanto a difusão redistribui as cargas e a eletromigração desloca as concentrações máximas para longe das extremidades da gota.

A segunda parte examina a eletrohidrodinâmica de gotas, sem surfactantes ou imposição de escoamento externo, apenas sob campos elétricos uniformes. Aqui, a convecção de carga superficial e a rotação de Quincke—uma rotação espontânea devido ao torque induzido pela distribuição de carga em relação à direção do campo elétrico aplicado—são analisadas. A estrutura numérica é estendida com o método de Ghost Fluid para lidar com descontinuidades interfaciais (por exemplo, permissividade, condutividade) e um modelo de interface difusiva que suaviza as transições na interface. Ao comparar os tratamentos de interface do tipo "sharp" (via Ghos fluid) e difusiva, identificamos regimes em que a convecção de carga domina a deformação e desencadeia a rotação de Quincke. O ângulo de inclinação durante a rotação alinha-se com a teoria para esferas rígidas em baixos números de capilaridade elétrica, mas apresenta uma leve divergência sob campos elétricos fortes, destacando o papel da mobilidade interfacial da gota. Comparações quantitativas com dados experimentais e modelos teóricos validam nossa metodologia, reforçando sua capacidade de unir paradigmas de interface "sharp" e difusiva.

Os resultados destte estudo avançam a compreensão da dinâmica de gotas em ambientes multifísicos, oferecendo insights para otimizar a estabilidade de emulsões e a manipulação eletrohidrodinâmica em aplicações industriais.

Palavras-chaves: emulsões, surfactantes iônicos, eletrohidrodinâmica, Level set, Ghost fluid.

Abstract

Numerical Study of Complex Fluid-Interface Systems: From Ionic Surfactant-Covered Droplets to Electrohydrodynamic Phenomena

Author: Juan Linhares Barbosa

Supervisor: Taygoara Felamingo de Oliveira, Prof. Dr., UnB

Co-Supervisor: Rodrigo Bento Rebouças, Prof. Dr., UnB

MSc in Mechanical Sciences

Brasília, 2025

The stability and control of emulsion flows are key aspects in designing products across industries such as environmental engineering, oil recovery, food processing, and pharmaceuticals. Emulsion stability hinges on interfacial phenomena, where ionic surfactants—amphiphilic molecules with charged head and tail groups—play a critical role by adsorbing at droplet interfaces, reducing surface tension, and imparting electrostatic repulsion to hinder coalescence. Surfactants redistribute over the droplet surface under imposed flow, coupling interfacial mechanics with charge transport mechanisms. This study investigates two interconnected aspects of droplet electrohydrodynamics: (1) the interplay among the effect of surfactant charge, induced electric field, and bulk flow stresses on the interfacial force balance and droplet dynamics, and (2) the electrohydrodynamic response of droplets under applied electric fields, focusing on charge convection and Quincke rotation.

In the first part, we numerically study surfactant-laden droplets in shear flow, employing a unified framework that integrates electric, interfacial and hydrodynamic effects. A coupled numerical methodology combines the projection method to solve the Navier-Stokes equations, the level-set technique to capture the interface, and the closest-point method to resolve surfactant transport. This approach captures the balance among shear-driven advection, surfactant diffusion, and electromigration of ionic charges on the droplet on droplet interface. We demonstrate that droplet deformation is governed by the Mason number (ratio of viscous to electric forces), the mobility ratio (charge transport efficiency), the capillary number (ratio of viscous and capillary forces), the Peclet number (ratio of convective and diffusive transport of surfactant), the surface surfactant coverage, and surfactant elasticity. Surface charge density depend linearly on surfactant concentration, the flow field advects charges to high-curvature regions, while diffusion redistributes

charges along the interface and electromigration shifts peak concentrations away from droplet tips.

The second part examines electrohydrodynamics of clean droplets (without surfactants or imposed shear flow) under uniform electric fields. Surface charge convection and Quincke rotation—a spontaneous rotation due to charge-induced torque—are analyzed. The numerical framework is extended with the ghost fluid method to handle interfacial discontinuities (e.g., permittivity, conductivity) and a diffusive interface model that smoothens transitions across the interface. By comparing sharp (ghost fluid) and diffuse interface treatments, we identify regimes where charge convection dominates droplet deformation and triggers Quincke rotation. The tilt angle during rotation agrees with rigid sphere theory at low electric capillary numbers but shows a slight mismatch under strong electric fields, highlighting the role of droplet deformation and interfacial mobility. Quantitative comparisons with experimental data and theoretical models validate our methodology, underscoring its capability to bridge the gap between sharp and diffuse interface paradigms.

This work advances the current understanding of droplet dynamics in multifield environments, offering insights for optimizing emulsion stability and electrohydrodynamic manipulation in industrial and biophysical applications.

Keywords: emulsions, ionic surfactants, electrohydrodynamics, Level set, Ghost fluid.

List of Figures

rigure 1 –	pended in another fluid. Note that the illustration is not to scale	11
Figure 2 –	Surface element used to derive equations at surface. $\hat{\mathbf{b}}$ is the unit bi-	11
	normal vector, $\hat{\mathbf{t}}$ is the unit tangential vector and $\hat{\mathbf{n}}$ is the unit normal	
	vector. $d\Gamma$ represents the contour and dS is the finite surface element .	14
Figure 3 -	Schematic diagram of the problem of a droplet suspended in another	
1100100	fluid and subjected to an applied uniform electric field with accumula-	
	tion of surface charge at the interface; the outer fluid is more conducting	
	than the inner one	21
Figure 4 –	Schematic representation of a equidistant separated points sequence	26
	Staggered grid proposed by Kim and Moin (1985)	28
	Representation of the level set function.	28
_	Geometric representation of the closest point method. The black dots	
110010	represent points in the grid, while the blue squares indicate their cor-	
		32
Figure 8 -	Schematic representation of interface models used: (a) Diffusive inter-	-
0	face: blue dots represent inner region grid points, red dots represent	
	outer region grid points, and black dots represent diffusive interface	
	grid points (2ε thickness). (b) Sharp interface: similar colors to dif-	
	fusive interface, with light blue and light red dots representing grid	
	points with at least one neighboring grid point on the opposite side of	
	the interface. The blue and red squares represent ghost grid points	34
Figure 9 –	Subcell resolution	35
	Top and bottom boundaries representation. The red dots represent	
	points outside the domain (ghost points), while the black dots rep-	
	resent points inside the domain	40
Figure 11 –	Normal derivative computed by one-side extrapolation using values of	
	ψ calculated at $\mathbf{cp}_1(x_{i,j})$, $\mathbf{cp}_2(x_{i,j})$ and $\mathbf{cp}_3(x_{i,j})$	44
Figure 12 –	Top and bottom boundaries representation. The red symbols represent	
-	points outside the domain (ghost points), while the black symbols rep-	
	resent points inside the domain.	45

Figure 13 –	Representation of left and right periodic boundaries. Ghost points (red symbols) on the left match the domain points (black symbols) on the	
	right, and vice versa, to ensure periodic behavior	47
Figure 14 -	Geometrical representation of the droplet measure. Each yellow dot on	
	the surface corresponds to an angle θ_i (Pimenta, 2023)	51
Figure 15 -	Convergence analysis for simulations with Re = 0.01, Ca = 0.1, λ = 1,	
	Pe = 10, $X = 0.6$, and $E = 0.2$. Surfactant concentration c_h obtained	
	at $t = 0.5$	53
Figure 16 –	Comparison between the numerical electric potential field in y-direction	
	with the analytical 1D solution for a circular geometry. The inset de-	
	picts a circular droplet with concentric electric potential contours and	
	radial electric field vectors	55
Figure 17 –	Taylor deformation as a function of the Capillary Number for Re =	
	$0.01, E = 0.1, X = 0.6, \text{ and } \alpha = \frac{Pe}{Ca} = 10.$	56
Figure 18 –	Droplet shape comparison for $Re = 0.01$, $E = 0.1$, $X = 0.6$, $Pe = 2.5$,	
	Ca = 0.25	56
Figure 19 –	Simulations for Re = 0.01, Ca = 0.1, Pe = 10, and $E = 0.2$. The	
	steady-state Taylor deformation and inclination for the Non-Ionic case	
	are $D_{NI} = 0.12$ and $\theta_{NI} = 37.8^{\circ}$ for $X = 0.1$, and $D_{NI} = 0.149$ and	
	$\theta_{NI} = 35.8^{\circ} \text{ for } X = 0.6. \dots$	57
Figure 20 –	Simulations for Re = 0.01, Ca = 0.5, Pe = 10, and $E = 0.2$. The	
	steady-state Taylor deformation and inclination for the Non-Ionic case	
	are $D_{NI}=0.58$ and $\theta_{NI}=15.5^{\circ}$ for $X=0.1$, and $D_{NI}=0.66$ and	
	$\theta_{NI} = 13.3^{\circ} \text{ for } X = 0.6. \dots$	58
Figure 21 –	Pressure contour and electric force vector field in steady-state for $Re =$	
	0.01, Ca = 0.5, Pe = 10, X = 0.1, E = 0.2, Mn = 0.2 and $R_{\mathcal{M}}$ = 0.1	58
Figure 22 –	Streamlines and pressure field for Re = 0.01, Pe = 10, $E = 0.2$, Mn =	
	0.2, and $R_{\mathcal{M}} = 0.1$	60
Figure 23 -	Streamlines and surfactant concentration for Re = 0.01, Pe = 10, $E =$	
	0.2, $Mn = 0.2$, and $R_{\mathcal{M}} = 0.1$	61
Figure 24 -	Electric field magnitude for Re = 0.01, Pe = 10, E = 0.2, Mn = 0.2,	
	and $R_{\mathcal{M}} = 0.1$	62
$Figure\ 25\ -$	Droplet elongation, represented by the aspect ratio L/B , as a function	
	of 1/Mn for Re = 0.01, Ca = 0.1, Pe = 10, $E = 0.2$, and $R_{\mathcal{M}} = 0.1$.	
	The parameter C_0 in the analytical expression accounts for the pressure	
	jump across the interface	63
$Figure\ 26\ -$	Surfactant concentration as a function of the normalized arc length for	
	Re = 10, Ca = 0.1, Pe = 10, X = 0.6, and E = 0.2, captured at	
	t=9. The insets show the surfactant concentration contours on the	
	droplet surface, pointing out regions with higher and lower surfactant	
	concentrations	63

Figure 27 –	Peak-to-peak amplitude of the surfactant concentration as a function	
	of the Mobility ratio for Re = 10, Ca = 0.1, Pe = 10, $X = 0.6$, $E = 0.2$,	
	and $Mn = 5$ for different instant times	64
Figure 28 -	Interfacial tension and forces for Re = 10, Ca = 0.1, Pe = 10, $X = 0.6$,	
	E=0.2, and Mn = 5.0 captured at $t=9$	65
Figure 29 –	Surfactant concentration as a function of the normalized arc length for	
	$\mathrm{Re}=0.01,\mathrm{Ca}=0.1,\mathrm{Pe}=10,X=0.6,\mathrm{and}~E=0.2$ at steady-state.	66
Figure 30 -	Peak-to-peak amplitude of the surfactant concentration as a function of	
	the Mobility ratio for Re = 0.01, Ca = 0.1, Pe = 10, $X = 0.6$, $E = 0.2$,	
	and $Mn = 5$ for different instant times	66
Figure 31 -	Position of the first peak in surfactant concentration as a function of	
	the Mobility ratio for Re = 0.01, Ca = 0.1, Pe = 10, $X = 0.6$, $E = 0.2$,	
	and $Mn = 5$ for different instant times	67
Figure 32 –	Behavior of droplet pairs in simple shear flow for $Re = 0.01$, $Ca = 0.2$,	
	$\lambda = 1, X = 0.1, E = 0.2, Pe = 10.0, and R_{\mathcal{M}} = 2.0. \dots$	68
Figure 33 –	Minimum interface-to-interface distance (d_{\min}) between droplets over	
	time. Coalescence occurs at Mn = 10.0 (green curve), where $d_{\rm min} \to 0$.	68
Figure 34 -	Pressure contour and evolution of droplet pairs in simple shear flow at	
	different timestamps Re = 0.01, Ca = 0.2, λ = 1, X = 0.1, E = 0.2,	
	$Pe = 10.0, Mn = 5.0, and R_{\mathcal{M}} = 2.0. \dots$	69
Figure 35 –	Effects of Ca_E and R on droplet's deformation at $S=3.5$ and $Re_E=$	
	0.01, and comparison with previous numerical results of Cui, Wang and	
	Liu (2019)	72
Figure 36 -	Deformation regime diagram for a single droplet subjected to an applied	
	electric field. The contour red line representing $f_d = 0$ delineates the	
	transition between the prolate and oblate droplet shapes, depending on	
	the values of S and R. The dashed blue line separates regions where the	
	circulation flows from the equator to the poles (Region I) from regions	
	where the circulation flows from the poles to the equator (Regions II	
	and III)	72
Figure 37 –	Pressure contours for electrohydrodynamic flow for $S=3.5,R=1.75,$	
	and $Ca_E = 0.5$. Results are shown for both sharp and smoothed inter-	
	face models	73
Figure 38 –	Electric charge density contours and streamlines for electrohydrody-	
	namic flow for S = 3.5, R = 1.75, and $\mathrm{Ca_E} = 0.5$. Results are shown	
	for both sharp and smoothed interface models	74
Figure 39 –	Electric field magnitude contours for electrohydrodynamic flow for $S=$	
	$3.5,\ R=1.75,\ and\ Ca_E=0.5.$ Results are shown for both sharp and	
	smoothed interface models	74

Figure 40 –	Taylor deformation as a function of the electric conductivity ratio for	
	$S=10, Ca_E=0.18, Re_E=0.01$ and $\lambda=1.$ The insets show droplet	
	contour for both interface models at $R=1.8$ and $R=14.5.$	75
Figure 41 –	Normalized deformation as a function of the electric Reynolds number	
	for S = 3.5, R = 1.75, $Ca_E = 0.5$ and $\lambda = 1$. The deformations of the	
	case without surface charge convection are $D_0 = 0.093$ and $D_0 = 0.096$	
	for the Sharp and Smoothed interface models, respectively. The inset	
	presents the shape contour of the droplet for both interface models at	
	$Re_E = 5$	76
Figure 42 –	Normalized deformation as a function of the electric Reynolds number	
	for $S = 0.5$, $R = 2.0$, $Ca_E = 0.5$ and $\lambda = 1$. The deformations of the	
	case without surface charge convection are $D_0 = 0.102$ and $D_0 = 0.106$	
		77
Figure 43 –	Transient deformation for two configurations: oblate droplet (red) with	
	$S = 3.5$, $R = 1.75$, and $Ca_E = 0.5$; prolate droplet (blue) with $S = 0.5$,	
	$R = 2.0$, and $Ca_E = 0.5$	78
Figure 44 -	Surface charge density as a function of the angular position θ for differ-	
	ent time instants. Results are shown for $S=3.5,R=1.75,Ca_E=0.5$	
	and $Re_E = 5$ for an oblate droplet. The inset defines θ around the droplet.	79
Figure 45 –	Surface charge density as a function of the angular position θ for dif-	
	ferent time instants. Results are shown for $S=0.5,R=2,Ca_E=0.5$	
	and $Re_E = 1$. The inset defines θ around the droplet	80
Figure 46 –	Illustration of a single droplet subjected to an applied electric field \mathbf{E}_0 .	
	The misalignment of the induced dipole moment ${f P}$ generates a torque,	
	leading to the droplet's electrohydrodynamic rotation. (Adapted from	
	Dong and Sau (2023))	81
Figure 47 –	Flow pattern transition between quadrupolar flow to circular flow dur-	
	ing Quincke regime of a droplet for S = 0.5, R = 0.01, $Ca_E = 0.6$,	
	$\mathrm{Re_E} = 6.0$ and $\lambda = 20$. The streamlines are plotted in black and droplet	
	contour in blue	82
Figure 48 –	Transient deformation during Quincke rotation of Fig. 47	83
Figure 49 -	Both numerical and experimental results correspond to the system de-	
	scribed in Table 3. The experimental data from Salipante and Vla-	
	hovska (2010) were obtained at $Ca_{MW} = 1.58$, whereas the present	
	work and the simulations of Das and Saintillan (2017) were conducted	
	at $Ca_{MW} = 0.44$	85
Figure 50 –	Schematic representation of the droplet model under elongation, where	
	the total electric charge Q is assumed to be concentrated as two point	
	charges at the tips, each with $Q/2$. The resulting electric force is mod-	
	eled as a Coulombic interaction between the charges	.03

List of Tables

Table 1 -	Typical values of physical parameters in the problem	19
Table 2 -	Typical dimensionless groups	19
Table 3 -	Material properties corresponding to the system used in experiments of	
	Salipante and Vlahovska (2010) and other dimensional parameters	84
Table 4 -	Dimensionless parameters calculated using the material properties shown	
	in Table 3	84

List of abbreviations and acronyms

SSOR Symmetric Successive Over-Relaxation

TVD Total Variation Diminishing

ENO Essentially Non-Oscillatory

WENO Weighted Essentially Non-Oscillatory

PDE Partial Differential Equation

 ${\bf SPDE} \qquad \qquad {\it Surface \ Partial \ Differential \ Equation}$

VOF Volume of Fluid

BEM Boundary Element Method

 $EHD \qquad \qquad Electrohydrodynamics$

GFM Ghost Fluid Method

List of symbols

Latin Symbols

a Droplet radius

 $a_{i,j}$ Coefficient of the left node of the five-points stencil

b Surface binormal vector

c Surfactant concentration

 c_0 Initial uniform surfactant concentration

 c_{∞} Maximum packing surfactant concentration

C Surface perimeter

 $c(\phi)$ Cut-off function

 $\mathbf{cp}(\mathbf{x})$ Function returning the closest point to \mathbf{x} on the interface

D Taylor deformation

 D_0 Deformation disregarding surface charge convection

 D_{NI} Deformation (Non-Ionic surfactant case)

 D_s Surfactant surface diffusion coefficient

e Elementary electric charge

E Droplet's elasticity; Extension operator

E Electric field

E₀ Applied electric field intensity

 E_{0x} Applied electric field component in x-direction

 E_{0y} Applied electric field component in y-direction

 \mathbf{E}_{s} Surface tangential electric field

 \mathscr{F} Generic higher-order function

f Generic first-order function

f_d	Discriminating function
\mathbf{F}	Generic vector function
\mathbf{F}_{γ}	Interfacial tension force vector
\mathbf{F}_{E}	Electric force vector
F	Faraday's constant
F_B	Source term from the bottom arm of the five–points stencil
F_c	Capillary force at the interface
F_e	Electric force at the interface
F_L	Source term from the left arm of the five–points stencil
F_m	Marangoni force at the interface
F_R	Source term from the right arm of the five–points stencil
F_T	Source term from the top arm of the five–points stencil
F_s	Surface force
g	Gravitational acceleration
g	Gravitational acceleration vector
h	Uniform grid spacing
H(x)	Heaviside function
I	Identity matrix
i	Index for discretization in the x -direction
j	Index for discretization in the y -direction
\mathbf{j}_s	Surface Nernst–Planck flux vector
K	Molecular interaction factor
L	2D droplet perimeter
L_x	Domain length in the x -direction
L_y	Domain length in the y -direction
\mathcal{M}	Ion mobility
\mathcal{M}_f	Flow–driven velocity

 \mathbf{M}_{E} Maxwell stress tensor

 N_x Number of nodes in the x-direction

 N_y Number of nodes in the y-direction

p Pressure field

 q_s Surface charge density

 q_{Γ} Surface charge density at the interface

 q_v Volumetric charge density

R Universal gas constant

r Richardson extrapolation convergence rate

s Arc length position of the droplet

 $S(\phi)$ Sign function of the level–set

t Time

 T_i ith tube region

T Absolute temperature

 U_d Drift velocity of the ion

 $U_{\rm EHD}$ Electrohydrodynamics-induced velocity

 U_x Velocity intensity of the top and bottom boundaries in x-direction

 U_{north} Velocity of the upper boundary

 $U_{
m bottom}$ Velocity of the lower boundary

u Velocity component in the x-direction

u Velocity field vector

 u^* Trial velocity component in the x-direction

 \mathbf{u}^* Trial velocity field vector

 $\tilde{\mathbf{u}}$ Extrapolated in time velocity field vector

v Velocity component in the y-direction

 v^* Trial velocity component in the y-direction

x Position in the x-direction

X	Position vector
\mathbf{x}_{Γ}	Droplet's interface position
X	Surfactant coverage factor
y	Position in the y -direction
z_1	Ionic surfactant valence
z_i	ith element of a generic sequence
n_x	x-component of the normal vector
n_y	y-component of the normal vector
ĥ	Surface normal vector
$\hat{\mathbf{t}}$	Surface tangential vector
P	Dipole moment of the droplet in EHD
	Greek Symbols
α	Tilt angle of the droplet in EHD
β	Tilt angle of a rigid sphere in EHD
β	Tilt angle of a rigid sphere in EHD Auxiliary pressure field; Generic material property
,	
χ	Auxiliary pressure field; Generic material property
χ $\delta(x)$	Auxiliary pressure field; Generic material property Dirac delta function
χ $\delta(x)$ $\delta_{arepsilon}(\phi)$	Auxiliary pressure field; Generic material property Dirac delta function Smoothed Dirac delta function
χ $\delta(x)$ $\delta_{arepsilon}(\phi)$	Auxiliary pressure field; Generic material property Dirac delta function Smoothed Dirac delta function Dielectric permittivity
χ $\delta(x)$ $\delta_{arepsilon}(\phi)$ ϵ	Auxiliary pressure field; Generic material property Dirac delta function Smoothed Dirac delta function Dielectric permittivity Half of interface thickness
χ $\delta(x)$ $\delta_{arepsilon}(\phi)$ ϵ $\hat{\epsilon}$	Auxiliary pressure field; Generic material property Dirac delta function Smoothed Dirac delta function Dielectric permittivity Half of interface thickness Effective dielectric permittivity
χ $\delta(x)$ $\delta_{\varepsilon}(\phi)$ ϵ $\hat{\epsilon}$ γ	Auxiliary pressure field; Generic material property Dirac delta function Smoothed Dirac delta function Dielectric permittivity Half of interface thickness Effective dielectric permittivity Interfacial tension
χ $\delta(x)$ $\delta_{\varepsilon}(\phi)$ ϵ $\hat{\epsilon}$ γ γ_0	Auxiliary pressure field; Generic material property Dirac delta function Smoothed Dirac delta function Dielectric permittivity Half of interface thickness Effective dielectric permittivity Interfacial tension Clean droplet interfacial tension
χ $\delta(x)$ $\delta_{\varepsilon}(\phi)$ ϵ ϵ $\hat{\epsilon}$ γ γ_0 $\dot{\gamma}$	Auxiliary pressure field; Generic material property Dirac delta function Smoothed Dirac delta function Dielectric permittivity Half of interface thickness Effective dielectric permittivity Interfacial tension Clean droplet interfacial tension Shear rate

 λ_m Function of virtual time for re–initialization of the level–set function

 λ_{ε} Smoothed viscosity ratio funtion

 μ Dynamic viscosity

 ϕ Level—Set function

 Φ_q Gravitational scalar potential

 ψ Electric potential field

 ρ Density

au Virtual time

 au_e Charge relaxation time scale

 τ_f Flow time scale

 θ Droplet inclination; Subcell resolution

 θ_{NI} Droplet inclination (Non–Ionic surfactant case)

 Ω^+ Domain outside the droplet

 Ω^- Domain inside the droplet

Dimensionless Groups

Ca Capillary number

Ca_E Electric capillary number

Ca_{MW} Maxwell-Wagner capillary number

Mn Mason number

Pe Peclet number

Re Reynolds number

Re_E Electric Reynolds number

R Electric permittivity ratio

 $R_{\mathcal{M}}$ Mobility ratio

S Dielectric permittivity ratio

Mathematical Operators

 \mathcal{D} Differential operator

 $\frac{D}{Dt}$ Material derivative

 δ_0 Mean operator

 \mathcal{I} Identity operator

 ∇ Gradient operator

 ∇_s Surface gradient operator

 ∇_+ Forward difference operator

 ∇_{-} Backward difference operator

 ∇_0 Central difference operator

 ξ Shift operator

 ∞ Infinity symbol

Summary

	1 INTRODUCTION 1	
1.1	On Ionic Surfactant-Covered Droplets	
1.2	On the Electrohydrodynamics of Droplet Flow	
1.3	Objectives	
1.3.1	For Ionic Surfactant-laden Droplets	
1.3.2	For the Electrohydrodynamics of Droplets Flow	
1.4	Scope of the work	
	2 FORMULATION FOR IONIC SURFACTANT-COVERED DROPLETS	11
2.1	Problem Statement	
2.2	Governing Equations	
2.2.1	Hydrodynamics equations	
2.2.2	Interfacial force	
2.2.3	Electrostatics equations	
2.2.4	lonic surfactant model	
2.2.5	Surfactant transport	
2.3	Nondimensionalization	
2.4	Dimensional Analysis	
	3 FORMULATION FOR ELECTROHYDRODYNAMICS OF DROPLETS	2 1
3.1	Problem Statement	
3.2	Governing Equations	
3.2.1	Hydrodynamics equations	
3.2.2	Electrostatic equations	
3.2.3	Leaky Dielectric Model	
3.2.4	Nondimensionalization	
	4 NUMERICAL METHODOLOGY	
4.1	Finite Difference method	
4.1.1	Finite difference operators	
4.1.2	Differential operator	
4.1.3	Staggered grid	
4.2	Level Set method	
4.2.1	Re-initialization of the level set function	

4.2.2 4.2.3	Local Level Set
4.2.3 4.3	Closest Point method
4.4	Interface models
4.4 .1	Sharp interface model (Ghost Fluid method)
4.4.2	Smoothed interface model (Continuum surface force)
4.5	Spatial discretization of the electric potential field equation 39
4.6	Projection method
4.6 .1	Spatial discretization of the momentum equation
4.6.2	Spatial discretization of the pressure equation
4.6.3	Boundary and initial conditions
4. 7	Discretization of the surfactant transport equation
4.8	Discretization of the surfactant transport equation
4.9	Numerical methodology for droplet deformation computation 50
4.9	Numerical methodology for droplet deformation computation 30
	5 RESULTS FOR IONIC SURFACTANT-COVERED DROPLETS 53
5.1	Convergence rate
5.2	Comparison of the electric potential
5.3	Ionic and non-ionic surfactant-covered droplet deformation 55
5.3.1	Comparison with small deformation theory
5.3.2	More detailed analysis of Mason number and Mobility ratio
5.4	Scalar field contours
5.5	Ionic and non-ionic surfactant concentration
5.6	Pairwise droplet interaction
	6 RESULTS FOR ELECTROHYDRODYNAMICS OF DROPLETS 71
6.1	Validation of the method using Smoothed and Sharp interface models 71
6.2	Influence of surface charge convection on steady-deformation 75
6.3	Transient behavior
6.4	Quincke Regime
6.4.1	Single Quincke droplet rotation
6.4.2	Tilt angle compared to rigid sphere
	7 CONCLUSION
	BIBLIOGRAPHY 89
	APPENDIX 99
	APPENDIX A – FIRST DERIVATIVE USING CENTRAL FINITE DIFFERENCE

APPENDIX	NITE DIFFERENCE
APPENDIX	C – DERIVATION OF SURFACTANT TRANSPORT EQUATION
APPENDIX	D – DROPLET ELONGATION PREDICTION 103
APPENDIX	E – DERIVATION OF SURFACE CHARGE TRANS- PORT EQUATION
APPENDIX	F – DERIVATION OF FRUMKIN-DAVIES ISOTHERM MODEL FOR INTERFACIAL TENSION 107

1 Introduction

1.1 On Ionic Surfactant-Covered Droplets

Multiphase immiscible fluid systems—such as emulsions, foams, and vesicle suspensions—are present in industries ranging from pharmaceuticals and food processing to petroleum and biotechnology (Solans et al., 2005; McClements, 2015; Salager, 2002; Binks, 2004). The functional properties of these dispersed phase systems—mechanical strength, thermal stability, and sensory characteristics—are dictated by the dynamic morphology of their dispersed phase, including droplet size, shape, and interfacial interactions (Bibette; Calderon; Poulin, 1999; Mason et al., 1996). Emulsions are two-phase mixtures of immiscible fluids where one fluid is dispersed in another continuous phase. The presence of surfactants at the droplet interface can change the macroscopic response of the emulsion. Surfactants are typically macromolecules composed of a hydrophilic head and a hydrophobic tail that can adsorb to fluid interfaces, altering local physico-chemical properties such as surface tension and stabilizing droplets against coalescence (Rosen, 2004; Israelachvili, 2011). Insoluble surfactants, which remain confined to the interface and do not dissolve into the bulk phase, play a particularly important role in interfacial dynamics due to their strong localization and ability to induce significant surface tension gradients. Ionic surfactants introduce an additional layer of complexity: the generation of electric fields at droplet interfaces, which can significantly alter interfacial dynamics, droplet deformation, and bulk rheology (Qazi et al., 2020; Tcholakova et al., 2008).

The theoretical foundation of surfactant behavior dates back to early studies on surface tension and interfacial phenomena by Laplace (1749–1827) and Young (1773–1829), which provided a fundamental understanding of capillary effects (Young, 1805; Gennes; Brochard-Wyart; Quéré, 2004). This groundwork was further expanded by Bancroft (1913), who pioneered research on emulsification, elucidating how surfactants stabilize multiphase systems. Subsequent advancements by Langmuir (1925) introduced molecular-level insights, particularly on the orientation and distribution of surfactant molecules at interfaces, while Frumkin (1925) established critical equations of state linking interfacial tension to adsorption kinetics. In parallel, Bouasse (1924) contributed to the study of capillary phenomena and surface interactions, reinforcing the role of surfactants in interfacial stability.

In the mid-20th century, Ward and Tordai (1944) made contributions by developing models to describe surfactant adsorption kinetics at interfaces. Their work introduced the concept of diffusion-controlled and adsorption-limited processes, which remain central to understanding surfactant dynamics. Davies (1951) expanded this framework by investigating charged surfactant films, introducing equations of state that accounted for ionic distributions and surface catalysis, further bridging colloidal chemistry with interfacial phenomena. Davies and Rideal (1963) later formalized electrostatic corrections to the Langmuir isotherm for ionic surfactants, while Dukhin, Miller and Kretzschmar (1983, 1991) introduced the quasi-equilibrium approach using Gouy-Chapman theory to model adsorption kinetics including the effects of the ion's finite size.

Shinoda et al. (1963) emphasized the industrial and biological significance of surfactants, particularly in detergency, the textile industry, and biochemical research. Gao and Rosen (1995) synthesized key concepts in surfactant behavior, with a particular focus on dynamic surface tension and the relationship between surfactant structure and its interfacial properties. They emphasized the role of the critical micelle concentration (CMC) and how the structure of surfactants influences their surface-active behavior.

Dynamic surface tension and adsorption kinetics emerged as critical research areas in the 1980s–1990s. Borwankar and Wasan (1986,1988) investigated equilibrium and dynamics of surfactant adsorption, highlighting the interplay between diffusion and interfacial rearrangement. MacLeod and Radke (1994) later compared quasi-equilibrium and full transient models for ionic surfactants, concluding that discrepancies were negligible within experimental timescales. Stone (1990) derived a time-dependent convective-diffusion equation for surfactant transport along deformable interfaces, providing a theoretical foundation for understanding how spatial variations in surfactant concentration create interfacial tension gradients that drive Marangoni stresses and influence the deformation and stability of fluid interface. Lin, McKeigue and Maldarelli (1990) employed pendant drop digitization to study diffusion-controlled adsorption, revealing induction periods and kinetic-diffusive regimes. Lin, McKeigue and Maldarelli (1994) further explored cohesive energy effects on surfactant exchange processes, while Fainerman et al. (1998, 2002) developed generalized adsorption models for ionic and mixed surfactants.

The 1990s and early 2000s also saw a surge in studies on complex surfactant systems, including proteins, polymers, and polyelectrolytes. Miller et al. (2004) and Fainerman, Lucassen-Reynders and Miller (2003) developed models to describe the adsorption kinetics of proteins and polymers, which exhibit more complex behavior due to molecular reorientation and denaturation. Langevin and Argillier (2016) reviewed the interfacial properties of asphaltenes, drawing parallels between their behavior and that of proteins, further expanding the scope of surfactant research. During this period, Miller, Joos and Fainerman (1994) and Eastoe and Dalton (2000) further differentiated between diffusion-limited and kinetically controlled processes, particularly for ionic and nonionic surfactants. The role of surfactant exchange kinetics at interfaces was quantified by Pan, Green and Maldarelli (1998), integrating theoretical models with experimental validations. Additionally, Li and Pozrikidis (1997) investigated the effect of surfactants on drop deformation and the rheology of dilute emulsions in Stokes flow, providing insights into the complex

interplay between surfactant distribution and interfacial dynamics. Building upon this, Vlahovska and Loewenberg (2005) developed a small-deformation theory for insoluble surfactant-covered drops in linear flows, offering analytical solutions that further elucidate the influence of surfactants on drop behavior. These studies, focused on insoluble surfactants, which remain confined to the interface and significantly alter interfacial tension and flow dynamics. This class of problems highlights the critical role of insoluble surfactants in governing droplet deformation, stability, and rheological properties in emulsions.

Casandra et al. (2016) and Phan (2016) extended these frameworks to partially dissociated ionic surfactants, demonstrating the challenges in distinguishing dissociation effects from equilibrium and dynamic surface tension data. Casandra et al. (2018) further advanced this understanding by theoretically examining the effect of the degree of dissociation (α) on adsorption kinetics, showing that improper assumptions about α can lead to significant deviations in surfactant diffusivity and model parameters, even when equilibrium and dynamic surface tension data appear well-fitted.

The advent of microfluidics has revolutionized the study of surfactant dynamics. Alvarez et al. (2010, 2012) developed microtensiometers to measure dynamic interfacial tension, enabling the study of surfactant adsorption at shorter time scales and smaller length scales. Riechers et al. (2016) utilized microfluidic devices to study surfactant adsorption kinetics in droplets, providing insights into the transition between diffusion-controlled and adsorption-limited regimes. Deng, Schroën and de Ruiter (2022) and Liang et al. (2022) further advanced microfluidic techniques, allowing for precise measurements of dynamic interfacial tension and adsorption kinetics in complex systems.

In parallel, studies such as that by Qazi et al. (2020) have deepened our understanding of ionic surfactants by investigating the dynamic surface tension of CTAB and related species under high salt concentrations, highlighting the crucial role of counterions—ions of opposite charge that associate with the surfactant headgroups—and ionic strength.

Complementing these experimental and theoretical works, numerous numerical methods have been developed to simulate surfactant-laden two-phase flows with high accuracy—each with its own strengths and limitations. Early numerical studies by Li and Pozrikidis (1997) and Vlahovska and Loewenberg (2005) provided critical insights into drop deformation and the rheology of dilute emulsions by coupling boundary-integral formulations with convection—diffusion solvers to account for nonuniform surfactant distributions and the resulting Marangoni stresses. Finite Element Methods (FEM) have been widely used for solving partial differential equations (PDEs) on evolving surfaces. Dziuk and Elliott (2007, 2012, 2013) pioneered the use of FEM for surface PDEs, developing methods that approximate both the surface and the solution on finite element spaces, with rigorous error analysis and optimal convergence rates for elliptic PDEs. Barrett, Garcke and Nürnberg(2015a, 2015b) extended these approaches to two-phase flows with insoluble surfactants, ensuring stability and conservation of surfactant mass.

Front-Tracking Methods have also been employed to handle the intricate dynamics of surfactant-laden interfaces. Muradoglu and Tryggvason (2014) developed a front-tracking method for simulating soluble surfactants in 3D multiphase flows, using an explicit finite volume approach for the surfactant convection-diffusion equation. Jesus et al. (2015) applied implicit finite volume methods developed by Lenz, Nemadjieu and Rumpf (2011) to simulate 3D two-phase flows with insoluble surfactants, demonstrating the conservation of surfactant mass. Sorgentone and Tornberg (2017) combined spherical harmonics expansions with boundary integral methods to study surfactant-laden drop dynamics in 3D, achieving high accuracy in capturing interfacial deformations.

Level-Set Methods have gained popularity for their ability to handle topological changes of the dispersed phase. Xu and Zhao (2003) proposed an Eulerian formulation for solving PDEs on moving interfaces, which was later extended to simulate interfacial flows with insoluble and soluble surfactants (Xu; Yang; Lowengrub, 2012a; Xu; Shi; Lai, 2017). Ruuth and Merriman (2008) introduced the closest point method, which embeds surface PDEs into a narrowband around the interface, allowing for efficient and accurate solutions. Xu et al. (2006) further developed a level-set continuum surface force (CSF) method for two-phase flows with insoluble surfactants, demonstrating its capability to handle a wide range of viscosity and density ratios by incorporating surface tension forces directly into the Navier–Stokes equations. Building upon these methodologies, Pimenta and Oliveira (2021) employed a combination of the level set and closest point methods to study the rheology of dilute emulsions composed of surfactant-covered droplets.

Grid-Based Particle Methods (GBPM) offer an alternative approach for tracking evolving interfaces without the need for re-meshing. Leung and Zhao (2009) introduced GBPM, which represents the interface using meshless Lagrangian markers and computes geometric quantities through local polynomial approximations. Petras and Ruuth (2016) coupled GBPM with the closest point method to solve convection-diffusion equations on moving surfaces, achieving high accuracy even for complex geometries. Chu and Tsai (2018) proposed the implicit boundary integral method (IBIM), which extends surface PDEs into a volumetric domain, ensuring stability and reducing computational costs.

Immersed Interface Methods (IIM) and Ghost Fluid Methods (GFM) have also been applied to surfactant-laden flows. Li and Ito (2006) developed the IIM, which directly enforces jump conditions for velocity and pressure at the interface, providing accurate solutions for Stokes flows with surfactants. Kang, Fedkiw and Liu (2000) introduced the GFM, which captures normal jumps, whereas it smears out tangential jumps in the solution, simplifying the implementation of interfacial conditions.

Volume-of-Fluid (VOF) Methods and Diffuse Interface Methods have been used to simulate surfactant effects in multiphase flows. James and Lowengrub (2004) developed a VOF method that conserves surfactant mass, enabling simulations of interfacial flows with insoluble surfactants [14]. Adami, Hu and Adams (2010) proposed a conservative smoothed particle hydrodynamics (SPH) method for surfactant dynamics, which handles

complex interfacial deformations and surfactant transport.

Despite significant advancements in understanding surfactant adsorption kinetics, and dynamic interfacial phenomena, a gap remains in the study of insoluble ionic surfactant-covered droplets under imposed flow and electrostatic effects induced by surface charge density. Existing literature has yet to integrate the interplay of electromigration flux along droplet surfaces with classical fluid dynamics and surface phenomena. No framework currently addresses how the electric field generated by ionic surfactant molecules themselves—via surface charge accumulation or dipole interactions—modulates droplet behavior, or interfacial stability.

Current models of surfactant transport predominantly focus on diffusion- or adsorption-limited regimes, neglecting contributions from electrokinetic phenomena such as electromigration or electrophoretic redistribution of charged surfactants. Furthermore, the coupling between surfactant-generated electric fields and hydrodynamic stresses at deformable interfaces remains unexplored. This omission limits predictive capabilities in applications where electric fields inherently govern surfactant-laden systems, such as electrowetting, electrospray technologies, or biofluidic interfaces with inherent ionic gradients.

To bridge this gap, our work systematically investigates the role of insoluble ionic surfactants in shaping both electric fields and hydrodynamic responses at droplet interfaces. We propose a unified model that incorporates electromigration flux and electric stress contributions to interfacial momentum balance, offering new insights into the coupled effect of surfactant electrostatics and fluid dynamics.

1.2 On the Electrohydrodynamics of Droplet Flow

Electrohydrodynamics (EHD) is the study of fluid behavior under the influence of electric fields, encompassing phenomena such as electroosmosis, dielectrophoresis, and electrorotation. When applied to droplets, EHD examines how electric fields induce deformations, instabilities, and dynamic behaviors in liquid droplets. EHD has found widespread applications in areas ranging from industrial processing to biomedical technologies. For example, controlled droplet deformation and breakup play a critical role in inkjet printing technologies, where precise drop formation is essential (Basaran, 2002). In mass spectrometry, electrospray ionization techniques exploit EHD to generate highly charged droplets for improved ionization efficiency (Mora, 2000). Moreover, dielectrophoretic manipulation has enabled the development of lab-on-a-chip devices for sensitive biochemical analyses (Pohl, 1978). These diverse applications underscore the practical importance of EHD in designing and optimizing modern fluidic systems.

The theoretical foundation on electrohydrodynamics of droplets dates back to Allan and Mason (1962), who investigated the deformation and breakup of fluid drops under shear flow and electric fields, highlighting the fundamental role of electrical forces in

destabilizing drops. Taylor (1964) expanded Allan and Mason's (1962) work by analyzing the disintegration of water drops, providing one of the earliest quantitative descriptions of electric field-induced drop breakup. In subsequent work, Taylor (1966) introduced the leaky dielectric model, predicting steady deformation and internal circulation within drops subjected to electric fields. The leaky dielectric model was further reviewed by Melcher and Taylor (1969), who provided a comprehensive examination of interfacial shear stresses and their role in EHD phenomena.

Brazier-Smith, Jennings and Latham (1971) explored the interactions between individual drops and drop pairs in strong electric fields, contributing to the understanding of drop coalescence and stability. Similarly, Torza, Cox and Mason (1971) studied the conditions leading to drop deformation and eventual bursting under electric stress. Saville (1971) expanded this scope by investigating charge relaxation effects in liquid jets, shedding light on the role of interfacial charge dynamics.

Further developments in EHD theory and experimentation continued through the late 20th century. Ajayi (1978) provided clarifications on Taylor's electrohydrodynamic model, reinforcing its predictive capabilities by calculating drop deformations to second order in the capillary number. Jones and Kallio (1979) and Jones (1979) studied dielectrophoretic levitation and force calculations in nonuniform fields, broadening the practical applications of EHD principles.

The 1980s and 1990s saw advancements in experimental and computational studies. Arp, Foister and Mason (1980) extended the exploration of EHD effects in complex dispersions. Brooks et al. (1984) examined electrostatic and electrokinetic potentials in polymer-aqueous systems, bridging EHD with colloidal science. Haywood, Renksizbulut and Raithby (1991) investigated transient deformation in electrostatic fields, introducing time-dependent analyses into EHD research. Vizika and Saville (1992) explored both steady and oscillatory fields, extending Taylor's model to dynamic conditions.

Tsukada et al. (1993) provided dual perspectives on internal and external circulation around deformed drops, enriching the understanding of EHD-induced flow patterns. Feng and Scott (1996) advanced computational modeling of leaky dielectric drops, validating previous theoretical predictions. Baygents, Rivette and Stone (1998) examined interactions among drop pairs, offering insights into collective behaviors under electric fields.

The early 21st century continued this trajectory. Feng (1999) introduced finite electric Reynolds number effects, accounting for nonlinearities beyond low-Reynolds-number assumptions. Feng (2002) proposed a two-dimensional electrorotation model for fluid drops, further refining EHD simulation techniques. Tomar et al. (2007) utilized a volume-of-fluid approach to simulate complex two-phase flows, capturing interfacial dynamics that were previously difficult to quantify.

Hua, Lim and Wang (2008) conducted numerical simulations emphasizing the in-

fluence of viscosity on drop deformation in electric fields. Lin, Skjetne and Carlson (2012) introduced phase-field modeling, allowing for more sophisticated simulations of multiphase EHD interactions. Lanauze, Walker and Khair (2013) studied the effects of inertia and charge relaxation, revealing competing mechanisms in EHD deformation. Lanauze, Walker and Khair (2015) examined nonlinear drop deformation, highlighting deviations from classical models.

Building on these theoretical advancements, Das and Saintillan (2016) developed a nonlinear small-deformation theory for transient droplet electrohydrodynamics, addressing previously neglected transient charge relaxation and nonlinear charge convection. Their work extended the leaky dielectric model to second order in the electric capillary number, providing a refined framework for analyzing prolate or oblate steady shapes and interfacial toroidal flows. Subsequently, Das and Saintillan (2017) implemented a three-dimensional boundary element method to simulate viscous drops under strong electric fields, incorporating charge convection to study symmetry-breaking bifurcations leading to Quincke rotation. Their simulations closely matched experimental data of Salipante and Vlahovska (2010) and small-deformation theories, bridging gaps between theory and numerical experimentation.

Dong and Sau (2018) expanded the study of collective behaviors by investigating electrohydrodynamic interactions, deformation, and coalescence of suspended drop pairs at varied angles of incidence. Their simulations revealed how hydrodynamic forces and permittivity ratios govern alignment, coalescence, or divergence of drop pairs, complementing earlier work by Baygents, Rivette and Stone (1998) on drop interactions.

Further advances in Quincke rotation dynamics emerged with Dong and Sau (2023), who analyzed unsteady electrorotation of viscous drops in uniform fields. Their study uncovered transient phenomena such as evolving equatorial charge jets and identified three distinct rotation patterns governed by viscosity ratios and electric field strength. By linking rotation behavior to the competition between charge convection and conduction, they demonstrated how the electric Reynolds number (Re_E) dictates transitions between steady, periodic, or irregular rotation regimes.

Sengupta, Walker and Khair (2017) demonstrated the importance of surface charge convection in electrohydrodynamic breakup. More recently, Peng et al. (2024) revealed that surface charge convection in leaky-dielectric systems can lead to singular behaviors, such as the antisymmetric blowup of surface-charge density near the equator for weakly conducting oblate droplets, and the formation of stagnant, perfectly conducting surface-charge caps at the poles for prolate droplets. Mori and Young (2018) reframed the classical leaky dielectric theory as a weak electrolyte limit of an electrodiffusion model, bridging past and modern theoretical frameworks. Behera, Mandal and Chakraborty (2019) extended drop settling analyses beyond the Stokes regime, while Vlahovska (2019) provided a comprehensive review of EHD advances in drop and vesicle research. Abbasi et al. (2020) investigated the role of EHD forces in emulsion droplets, emphasizing applica-

tions in material science. Sorgentone and Vlahovska (2021) expanded numerical studies to three-dimensional interactions, improving the accuracy of computational models.

The most recent developments have introduced novel concepts such as Quincke rotation-driven propulsion. Dong et al. (2024) demonstrated this mechanism in microfluidic contexts, while Xie et al. (2024) proposed a self-propulsion strategy for Quincke droplets on superhydrophobic walls under low Reynolds number $\text{Re}_{\text{E}} \leq 1$. Their work highlighted the interplay between wall effects and electrohydrodynamic forces, offering new avenues for droplet manipulation in confined geometries. Firouznia, Bryngelson and Saintillan (2023) validated theoretical and numerical models against experimental data, further refining our understanding of EHD phenomena.

Numerical modeling of electrohydrodynamic (EHD) phenomena has seen significant advancements, particularly in the study of droplet deformation and dynamics under electric fields. However, a critical limitation in many numerical works is the reliance on the leaky dielectric model without evolving the charge conservation equation in time. This simplification restricts the ability to capture transient phenomena, such as charge convection and electrorotation, which are essential for understanding the full dynamics of EHD systems. Most studies assume a static charge distribution at the interface, neglecting the temporal evolution of surface charges and their convective transport, which can significantly influence droplet behavior.

Some authors have addressed this limitation by incorporating the evolution of the charge conservation equation into their numerical frameworks. For instance, Das and Saintillan (2017) developed a nonlinear small-deformation theory using the boundary element method, which accounts for surface charge convection and captures transient effects such as Quincke rotation. Similarly, Sengupta, Walker and Khair (2017) employed the boundary integral method to study the role of surface charge convection in the breakup of prolate drops. While these works provide valuable insights into the effects of charge convection and electrorotation, they are limited to the study of single droplets and do not extend to more complex multiphase systems.

Recent work by Dong et al. (2024) represents a step forward by using the Volume of Fluid (VOF) method to evolve the charge conservation equation and investigate self-propulsion of a pair of droplets, a phenomenon resulting from simultaneous Quincke rotation. However, their approach solves for electric charge in the bulk fluid rather than focusing solely on the interface, which may not fully resolve the sharp interfacial dynamics critical to EHD phenomena. In contrast, methods like the level set method and ghost fluid method (GFM) offer advantages in modeling sharp interfaces and handling discontinuities across phases. For example, Paknemat, Pishevar and Pournaderi (2012) used the level set method and GFM to study droplet deformation and breakup under electric fields, but their work did not evolve the charge conservation equation, limiting its ability to capture transient charge dynamics.

The work of Alidoost and Pishevar (2018) addresses this gap by employing the level set method and GFM to model a sharp interface while also evolving the charge conservation equation at the interface. Their study demonstrates how charge migration affects droplet deformation, particularly in oblate and prolate modes. However, their work does not explore the effects of charge convection or Quincke rotation, leaving room for further investigation into these phenomena.

The proposed framework aims to bridge the gap between existing numerical methods by focusing on the nonlinear effects of charge convection and electrorotation, which are often neglected in traditional leaky dielectric models.

1.3 Objectives

1.3.1 For Ionic Surfactant-laden Droplets

This dissertation aims to investigate the influence of electric charge density and interfacial dynamics on the behavior of ionic-surfactant-covered droplets in shear flow. The specific objectives are:

- Develop a theoretical framework to incorporate electric charge effects into surfactant dynamics;
- Introduce an electromigration flux term into the surfactant mass balance equation to model charge-driven transport at the droplet interface;
- Identify and characterize the dimensionless groups governing electric interactions, such as the electric Mason number and Mobility ratio;
- Analyze the impact of electric stresses on droplet deformation and inclination, quantifying the interplay between electrostatic and hydrodynamic forces;
- Explore the effect of electromigration flux on droplet deformation, inclination, and shape;
- Investigate the spatial distribution of surfactant along the droplet interface.

1.3.2 For the Electrohydrodynamics of Droplets Flow

This dissertation aims to develop and validate a numerical framework that integrates multiple computational techniques to investigate the influence of surface charge convection on droplet dynamics, with particular emphasis on the Quincke rotation regime. The specific objectives are:

- Develop a diffusive interface model to accurately solve the surface charge conservation equation on deformable interfaces;
- Integrate level-set, ghost fluid, and closest point methods into a unified framework to model sharp interface problems;
- Explore the effects of surface charge convection on droplet deformation and stability;
- Characterize the onset and dynamics of Quincke rotation of droplets in EHD regime;
- Conduct an initial investigation into the self-propulsion of droplets induced by Quincke rotation.

1.4 Scope of the work

This dissertation is structured as follows: Chapter 2 introduces the governing equations and theoretical framework for systems involving ionic surfactants. The chapter establishes the coupling between surfactant concentration, surface charge density, and electrostatic effects. Chapter 3 formulates the electrohydrodynamic problem, focusing on the interplay between electric fields, charge conservation, and electric stresses. Chapter 4 outlines the numerical methodology employed throughout the study, including: the finite difference method for approximating derivatives, projection method for solving the Navier-Stokes equations, the level-set technique for interface capturing, the closest-point method for surfactant transport, and the ghost fluid method for handling interfacial discontinuities. Additionally, Chapter 4 introduces the diffusive interface model as an alternative to the sharp interface approach, providing a comparative framework for resolving electrohydrodynamic phenomena. Chapter 5 presents and discusses the results for ionic surfactant-covered droplets subjected to shear flow. The chapter explores the effects of surfactant redistribution, electromigration, and charge intensity on droplet deformation, highlighting the roles of the Mason number and mobility ratio. Chapter 6 covers the results of the electrohydrodynamics of clean droplets under applied electric field, focusing on surface charge convection and the onset of Quincke rotation. The chapter compares predictions from sharp and diffuse interface models on droplet's deformation, analyzes the tilt angle during rotation, and validates results against rigid sphere theory and experimental data. Chapter 7 concludes the dissertation by summarizing key findings, highlighting the interplay between ionic surfactants, shear flow, and electrostatic effects in droplet dynamics. Potential directions for future research are proposed, including extensions to numerous multiphase systems and more complex electric field configurations.

2 Formulation for Ionic Surfactant-Covered Droplets

2.1 Problem Statement

A two-dimensional problem is assumed, consisting of a neutrally buoyant droplet covered with ionic insoluble surfactant of concentration denoted by c suspended in another liquid. The droplet initial radius is a. Both fluids are immiscible Newtonian fluids with constant physical properties, and the system is subjected to incompressible flow. The density, dielectric permittivity, and dynamic viscosity of the fluids are denoted as ρ , ϵ and μ , respectively, and the subscripts "i" and "o" are used to differentiate between inside and outside the droplet as illustrated in Fig. 3. No-slip boundary condition is applied at the stationaries upper and lower walls. For the electric potential, ψ , homogeneous Neumann boundary condition $\frac{\partial \psi}{\partial y} = 0$ is applied at the lower wall and upper walls. The domain is considered to be periodic along the x-direction.

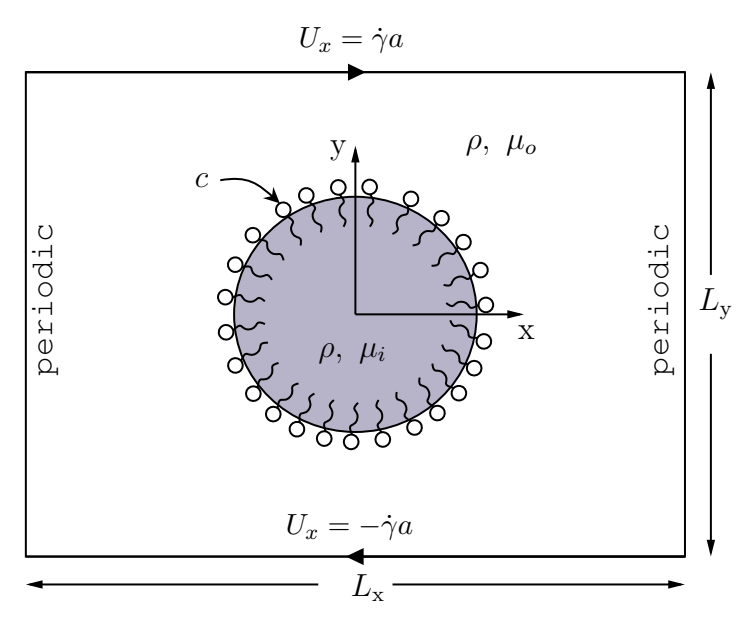


Figure 1 – Schematic diagram of the problem of a surfactant-covered droplet suspended in another fluid. Note that the illustration is not to scale.

2.2 Governing Equations

2.2.1 Hydrodynamics equations

The hydrodynamics is governed by the mass conservation and linear momentum equations as follows:

$$\nabla \cdot \mathbf{u} = 0, \tag{2.1}$$

and

$$\rho \frac{D\mathbf{u}}{Dt} = \nabla \cdot \boldsymbol{\sigma}_{\mathrm{H}} + \rho \mathbf{g}, \tag{2.2}$$

where ρ is the density, **u** is the velocity field, **g** is the gravitational acceleration field, and $\frac{D}{Dt}$ is the material derivative. The stress tensor of Newtonian fluid is given by

$$\boldsymbol{\sigma}_{\mathrm{H}} = -p\mathbf{I} + \mu(\nabla \mathbf{u} + \nabla \mathbf{u}^{\mathsf{T}}), \tag{2.3}$$

where p is the pressure field and μ is the dynamic viscosity coefficient.

The normal stress jump is given by the Young-Laplace law:

$$[\![\boldsymbol{\sigma}_{\mathrm{H}} \cdot \hat{\mathbf{n}}]\!] \cdot \hat{\mathbf{n}} = \gamma \nabla \cdot \hat{\mathbf{n}}, \tag{2.4}$$

where $[\![\,]\!]$ represents the outer-inner jump across the interface, γ is the surface tension coefficient, and $\hat{\mathbf{n}}$ is the outward pointing unit vector. The term $\nabla \cdot \hat{\mathbf{n}}$ computes the local mean curvature of the surface. If the surface tension coefficient varies along the interface (as a consequence of non-uniform surfactant concentration, for instance), then there is also a jump in shear stress given by

$$[\![\boldsymbol{\sigma}_{\mathrm{H}} \cdot \hat{\mathbf{n}}]\!] \cdot \hat{\mathbf{t}} = \nabla_s \gamma, \tag{2.5}$$

where $\hat{\mathbf{t}}$ is the tangential unit vector, and $\nabla_s = (\mathbf{I} - \hat{\mathbf{n}}\hat{\mathbf{n}}) \cdot \nabla$ is the surface gradient operator.

The velocity field must satisfy the continuity condition, ensuring that

$$[\![\mathbf{u}]\!] = \mathbf{0}. \tag{2.6}$$

Let $F(\mathbf{x}, t)$ be a shape function that implicitly defines the interface as $F(\mathbf{x}, t) = 0$. The kinematic boundary condition states that the interface moves with the flow, expressed as:

$$\frac{DF}{Dt} = 0. (2.7)$$

Expanding the material derivative:

$$\frac{\partial F}{\partial t} + \mathbf{u} \cdot \nabla F = 0. \tag{2.8}$$

The unit normal vector $\hat{\mathbf{n}}$ to the interface is expressed in terms of F as:

$$\hat{\mathbf{n}} = \frac{\nabla F}{|\nabla F|},\tag{2.9}$$

where $|\nabla F|$ is the magnitude of ∇F . Substituting $\nabla F = \hat{\mathbf{n}} |\nabla F|$ into Eq. (2.8), we obtain:

$$\frac{\partial F}{\partial t} + \mathbf{u} \cdot \hat{\mathbf{n}} |\nabla F| = 0. \tag{2.10}$$

Dividing through by $|\nabla F|$ (assuming $|\nabla F| \neq 0$), the kinematic condition can be rewritten as:

$$\frac{1}{|\nabla F|} \frac{\partial F}{\partial t} + \mathbf{u} \cdot \hat{\mathbf{n}} = 0. \tag{2.11}$$

If the interface does not change with time (i.e., it is in a steady state), then $\frac{\partial F}{\partial t} = 0$, and the kinematic condition simplifies to:

$$\mathbf{u} \cdot \hat{\mathbf{n}} = 0, \tag{2.12}$$

indicating that the velocity field has no component normal to the interface.

A natural approach to solving interfacial flow problems involves directly solving Eqs. (2.1) and (2.2) for both fluid phases, enforcing the coupling through the jump conditions given in Eqs. (2.4), (2.5), and (2.6). However, this direct formulation presents significant numerical challenges due to the discontinuities at the interface.

An alternative approach is to incorporate interfacial effects, such as surface tension and electrostatic stresses, as body forces in the momentum equation. By adopting this formulation, Eq. (2.2) is rewritten as

$$\rho \frac{D\mathbf{u}}{Dt} = -\nabla \bar{p} + \nabla \cdot [\mu(\mathbf{x})(\nabla \mathbf{u} + \nabla \mathbf{u}^{\mathsf{T}})] + \mathbf{F}_{\gamma} + \mathbf{F}_{\mathsf{E}}, \tag{2.13}$$

where \mathbf{F}_{γ} and $\mathbf{F}_{\rm E}$ represent body force terms per unit volume that account for interfacial tension and electrostatic effects, respectively. The body force associated with the gravitational field is expressed as the gradient of a scalar potential ($\mathbf{g} = -\nabla \Phi_g$) and is incorporated into the modified pressure, \bar{p} . For simplicity, the *overbar* notation will be omitted in subsequent sections.

2.2.2 Interfacial force

In the presence of an interface, there exists a pressure discontinuity that counteracts the influence of surface tension. This effect can be computed by balancing forces on a finite surface element dS, as visualized in Fig. 2:

$$\int_{S} \Delta \mathbf{f} dS = \oint_{C} \gamma \hat{\mathbf{b}} d\Gamma, \tag{2.14}$$

in which the left-side term is associated to the pressure jump, the right-side accounts for the surface tension (energy per unit area). The unit binormal vector, $\hat{\mathbf{b}}$, is perpendicular to tangential $\hat{\mathbf{t}}$ and normal $\hat{\mathbf{n}}$ unit vectors, obeying the relation $\hat{\mathbf{b}} = \hat{\mathbf{t}} \times \hat{\mathbf{n}}$, and $d\Gamma$ is the differential arc length along C. Using a variation of Stokes theorem on the right-side of Eq. (2.14), it can be rewritten as (Aris, 1989):

$$\int_{S} \Delta \mathbf{f} dS = \int_{S} [\nabla \cdot (\gamma \hat{\mathbf{n}}) \hat{\mathbf{n}} - \nabla (\gamma \hat{\mathbf{n}}) \cdot \hat{\mathbf{n}}] dS.$$
 (2.15)

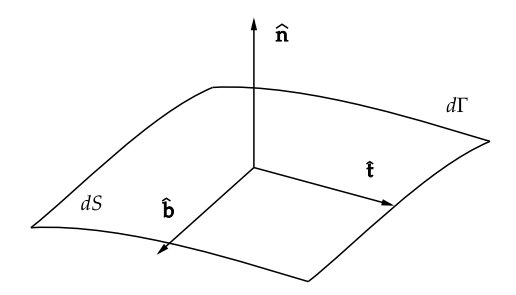


Figure 2 – Surface element used to derive equations at surface. $\hat{\mathbf{b}}$ is the unit binormal vector, $\hat{\mathbf{t}}$ is the unit tangential vector and $\hat{\mathbf{n}}$ is the unit normal vector. $d\Gamma$ represents the contour and dS is the finite surface element

Using a Dirac delta distribution to locate these contributions only around the interface, this leads to

$$\mathbf{F}_{\gamma} = (\nabla_s \gamma - \gamma \kappa \hat{\mathbf{n}}) \delta(\|\mathbf{x} - \mathbf{x}_{\Gamma}\|), \tag{2.16}$$

where γ is the surface tension coefficient, $\kappa = \nabla \cdot \hat{\mathbf{n}}$ is the local mean curvature, δ is the Dirac delta function, \mathbf{x}_{Γ} is the position of the droplet interface, ∇_s is the surface gradient operator, and \mathbf{I} is the unity tensor.

This approach that uses the Dirac delta function to localize the surface tension force at the interface, is a key feature of the Continuous Surface Force (CSF) model. The CSF model, originally proposed by Brackbill, Kothe and Zemach (1992), allows surface tension forces to be expressed as a volume force in the Navier-Stokes equations, making it easier to implement numerically. In this model, the Dirac delta function is approximated numerically using a smoothed function that spreads the force over a small region around the interface. This method is widely used in numerical simulations of multiphase flows, such as those involving the Volume of Fluid (VOF) or Level Set methods.

2.2.3 Electrostatics equations

The presence of ionic molecules on the interface increases the electric charge on the droplet surface, creating an electric field. The relation between the free electric charge and the electric field is governed by Gauss's Law:

$$\nabla \cdot (\epsilon \mathbf{E}) = q_v, \tag{2.17}$$

where ϵ , **E**, and q_v denote the electric permittivity, the electric field, and the free volumetric charge density, respectively.

In the absence of a magnetic field, the Maxwell-Faraday equation yields an irrotational electric field ($\nabla \times \mathbf{E} = 0$) and it can be written in terms of the electric potential (ψ) as $\mathbf{E} = -\nabla \psi$ (Masliyah; Bhattacharjee, 2006). Thus, Eq. (2.17) becomes

$$\nabla \cdot (\epsilon \nabla \psi) = -q_v. \tag{2.18}$$

The electric force in Eq. (2.13) can be written as follows

$$\mathbf{F}_{\mathrm{E}} = \nabla \cdot \mathbf{M}_{\mathrm{E}},\tag{2.19}$$

where \mathbf{M}_{E} is the electric Maxwell stress tensor, given by

$$\mathbf{M}_{\mathrm{E}} = \epsilon \left[\mathbf{E} \mathbf{E} - \frac{1}{2} (\mathbf{E} \cdot \mathbf{E}) \mathbf{I} \right]. \tag{2.20}$$

Operating the divergence in Eq. (2.19), yields

$$\mathbf{F}_{\mathrm{E}} = q_v \mathbf{E} - \frac{1}{2} \mathbf{E} \cdot \mathbf{E} \nabla \epsilon, \qquad (2.21)$$

where the first and the second terms on the right-side are called Coulomb force and dielectric force, respectively. In the absence of free electric charge, the electric force only arises from permittivity gradients, a phenomenon tipically found in perfect dielectric mediums.

2.2.4 Ionic surfactant model

This section focuses in presenting the considerations made to unite the electrostatic theory with the interfacial problem.

The presence of ionic surfactant along the droplet interface changes the surface tension that can be modeled by the Langmuir isotherm equation of state (Langmuir, 1932),

$$\gamma(c) = \gamma_0 + RTc_{\infty} \left[\ln \left(1 - \frac{c}{c_{\infty}} \right) - \frac{K}{2} \left(\frac{c}{c_{\infty}} \right)^2 \right], \tag{2.22}$$

where γ_0 is the surface tension of a clean interface (no surfactant), R is the universal gas constant, T is the absolute temperature, c_{∞} is the maximum packing concentration of surfactant, K is a model parameter that takes into account the molecular interaction among the surfactant molecules, z_1 is the ionic surfactant valence, and F = 96485 C/mol is the Faraday's constant (that represents the total electric charge carried by one mole of electrons).

Since all the free charge is concentrated at the droplet surface, q_v and q_s are related by $q_v = q_s \delta(\|\mathbf{x} - \mathbf{x}_{\Gamma}\|)$, where the Dirac delta has per length units. Hence, the Gauss's Law for the diffusive interface model reduces to

$$\nabla \cdot (\epsilon \nabla \psi) = -q_s \delta(\|\mathbf{x} - \mathbf{x}_{\Gamma}\|). \tag{2.23}$$

The surface charge density due to the presence of ionic surfactant is (Datwani; Stebe, 1999):

$$q_s = z_1 F c, (2.24)$$

where $z_1 Fc$ is the increase in surface charge due to ionic surfactant concentration.

Using the relation in Eq. (2.24) in Eq. (2.23) and assuming a constant dielectric permittivity, the Poisson equation for the electric potential is recast as:

$$\nabla^2 \psi = -\frac{z_1 F c}{\epsilon} \delta(\|\mathbf{x} - \mathbf{x}_{\Gamma}\|). \tag{2.25}$$

The electric force given by Eq. (2.21) becomes

$$\mathbf{F}_{\mathrm{E}} = z_1 \mathrm{F} c \,\delta(\|\mathbf{x} - \mathbf{x}_{\Gamma}\|) \mathbf{E}. \tag{2.26}$$

The polarization force is not considered in Eq. (2.26) due to the assumption of constant dielectric permittivity. This approach assumes that electric effects arise solely from charges carried by the ionic surfactant, without accounting for significant contributions from permittivity gradients.

2.2.5 Surfactant transport

For a surfactant-covered droplet, an additional equation is required to account for the concentration of an insoluble surfactant on the droplet surface. It can be obtained by considering a mass balance through a finite surface element dS, which lies on a curved surface. From the mass conservation law, an evolution equation for the surfactant concentration c can be written as follows

$$\frac{D}{Dt} \int_{S} c \, dS = -\oint_{C} \hat{\mathbf{b}} \cdot \mathbf{j}_{s} \, d\Gamma, \tag{2.27}$$

where \mathbf{j}_s is the tangential flux vector, determined by Nernst-Planck equation, which generalizes Fick's law of diffusion to account for electrostatic forces acting on diffusing particles (Masliyah; Bhattacharjee, 2006). Since c is only defined along the surface, Nernst-Planck equation can be written as

$$\mathbf{j}_s = -D_s \nabla_s c + \frac{D_s z_1 e}{k_B T} c \, \mathbf{E}_s, \tag{2.28}$$

where D_s is the surface diffusion coefficient of the surfactant, z_1 is the valence of the ionic surfactant species, e is the elementary charge, $k_B = 1.380649 \times 10^{-23}$ J/K is the Boltzmann constant, and T is the absolute temperature. The surfactant transport equation accounting the Nernst-Planck flux is given by (see complete derivation in Appendix C):

$$\frac{\partial c}{\partial t} + \nabla_s \cdot (c\mathbf{u}) = \nabla_s \cdot \left(D_s \nabla_s c - \frac{D_s z e}{k_B T} c \mathbf{E}_s \right). \tag{2.29}$$

The Einstein relation between the diffusion coefficient D_s and the ion mobility \mathcal{M} can be written as:

$$D_s = \frac{k_B T}{z_1 e} \mathcal{M},\tag{2.30}$$

where k_B is the Boltzmann constant, T is the absolute temperature, z_1 is the charge number of the ion, and e is the elementary charge. This relation is a fundamental result in

statistical mechanics and transport theory, connecting the diffusion coefficient D_s and the mobility \mathcal{M} of particles in a fluid (Einstein, 1905). It reflects the balance between random thermal motion (diffusion) and directed motion due to an external force (mobility), both driven by thermal energy k_BT .

Using the Einstein relation, D_s in Eq. (2.29) can be replaced, leading to

$$\frac{\partial c}{\partial t} + \nabla_s \cdot (c\mathbf{u}) = \nabla_s \cdot (D_s \nabla_s c - \mathcal{M} c \mathbf{E}_s). \tag{2.31}$$

An important aspect of Eq. (2.31) is the ion mobility \mathcal{M} in the electromigration term. This quantity represents the ion's ability to move with a drift velocity U_d under the influence of an applied electric field E_0 , and can be defined as $\mathcal{M} = \frac{U_d}{E_0}$. The ion mobility expresses how efficiently an ion responds to the electric field. The electromigration term can also be interpreted as an advective flux driven by an effective velocity field $\mathbf{u}^e = \mathcal{M}\mathbf{E}_s$, allowing Eq. (2.29) to be rewritten in the form:

$$\frac{\partial c}{\partial t} + \nabla_s \cdot (c\mathbf{u} + c\mathbf{u}^e) = \nabla_s \cdot (D_s \nabla_s c). \tag{2.32}$$

2.3 Nondimensionalization

The governing equations were normalized using the droplet radius a as the characteristic length, $1/\dot{\gamma}$ as the characteristic time, $\dot{\gamma}a$ as the characteristic velocity, μ_o as the characteristic viscosity, $\mu_o\dot{\gamma}$ as the characteristic pressure, γ_0 as the free surfactant characteristic surface tension, c_0 as the characteristic surfactant coverage, and $z_1 Fac_0/\epsilon$ as the characteristic electric potential. The resulting dimensionless variables are:

$$t^* = \dot{\gamma}t$$
, $\mathbf{x}^* = \mathbf{x}/a$, $\mathbf{u}^* = \mathbf{u}/(\dot{\gamma}a)$, $p^* = p/(\mu_o\dot{\gamma})$, $\kappa^* = a\kappa$, $\lambda = \mu/\mu_o$, $\nabla^* = a\nabla$, $\delta^* = a\delta$, $\psi^* = \epsilon\psi/(z_1 Fac_0)$, $\mathbf{E}^* = \epsilon \mathbf{E}/(z_1 Fc_0)$, $\gamma^* = \gamma/\gamma_0$, and $c^* = c/c_0$. (2.33)

Equations (2.1), (2.13), (2.18) and (2.29) in dimensionless form are:

$$\nabla^* \cdot \mathbf{u}^* = 0, \tag{2.34}$$

$$\operatorname{Re} \frac{D\mathbf{u}^{*}}{Dt^{*}} = -\nabla^{*}p^{*} + \nabla^{*} \cdot [\lambda(\mathbf{x})(\nabla^{*}\mathbf{u}^{*} + \nabla^{*}\mathbf{u}^{*\top})] + \frac{1}{\operatorname{Ca}}(\nabla_{s}^{*}\gamma^{*} - \kappa^{*}\gamma^{*}\mathbf{n})\delta(\|\mathbf{x}^{*} - \mathbf{x}_{\Gamma}^{*}\|) + \frac{1}{\operatorname{Mn}}c^{*}\mathbf{E}^{*}\delta(\|\mathbf{x}^{*} - \mathbf{x}_{\Gamma}^{*}\|),$$
(2.35)

$$\gamma^*(c^*) = 1 + E\left[\ln\left(1 - Xc^*\right) - \frac{K}{2}X^2c^{*2}\right],\tag{2.36}$$

$$\nabla^{*2}\psi^* = -c^*\delta(\|\mathbf{x}^* - \mathbf{x}_{\Gamma}^*\|), \tag{2.37}$$

$$\frac{\partial c^*}{\partial t^*} + \nabla_s^* \cdot (c^* \mathbf{u}^*) = \frac{1}{\text{Pe}} \nabla_s^{*2} c^* - \mathcal{R}_{\mathcal{M}} \nabla_s^* \cdot (c^* \mathbf{E}_s^*), \qquad (2.38)$$

In Eq. (2.35) the dimensionless groups are:

Re =
$$\frac{\rho \dot{\gamma} a^2}{\mu_o}$$
, Ca = $\frac{\mu_o \dot{\gamma} a}{\gamma_0}$, and Mn = $\frac{\epsilon \mu_o \dot{\gamma}}{z_1^2 F^2 c_0^2}$, (2.39)

where the Reynolds number (Re) measures the relative importance of inertia and viscous forces; the capillary number (Ca) measures the relative importance of viscous and capillary forces, and the Mason number relates viscous and electric forces due to the presence of ionic surfactant.

In Eq. (2.36), the dimensionless groups are:

$$E = \frac{\text{RT}c_{\infty}}{\gamma_0} \quad \text{and} \quad X = \frac{c_0}{c_{\infty}}, \tag{2.40}$$

in which the surfactant elasticity (E) represents the sensitivity of surface tension to changes in surfactant concentration, and the surfactant coverage factor (X) quantifies the fraction of the surface area covered by surfactant molecules.

In Eq. (2.38), two dimensionless groups emerge as:

$$Pe = \frac{\dot{\gamma}a^2}{D_s}$$
, and $R_{\mathcal{M}} = \frac{\mathcal{M}}{\mathcal{M}_f} = \frac{z_1^2 F^2 D_s c_0}{\dot{\gamma} a RT \epsilon}$. (2.41)

The Péclet number (Pe) represents the relative importance of advection to diffusion for the transport of surfactant on the droplet surface. The mobility ratio (R_M) compares the ion's mobility in response to the overall electric field created by the ion's own charge with its mobility due to the external fluid flow, indicating the relative influence of electric forces versus hydrodynamic forces on ion transport.

Note that a flow-driven mobility, denoted as $\mathcal{M}_f = \frac{\dot{\gamma}a\epsilon}{z_1Fc_0}$, is defined similarly to the electric ion mobility \mathcal{M} . The key difference is that \mathcal{M}_f uses the characteristic flow velocity $\dot{\gamma}a$ instead of the drift velocity $U_d = \frac{z_1^2F^2D_sc_0}{RT\epsilon}$, providing a measure of the ion's mobility in relation to the external flow.

2.4 Dimensional Analysis

This section provides some realistic values for the physical parameters relevant to the problem, offering a sense of their magnitude. These values are not intended to restrict the scope of the study but rather serve as a guide to the typical order of magnitude for the parameters in question. Table 1 summarizes these values for key parameters such as droplet radius, fluid properties, surfactant properties, and environmental conditions, which are commonly encountered in such problems, vegetable oil systems, for example.

The combination of these parameters leads to the dimensionless groups presented in Table 2. The Reynolds number, that is quite small (Re = 0.008), indicates a creeping flow regime, where inertial forces are negligible compared to viscous forces, typical for

Table 1 – Typical values of physical parameters in the problem.

Parameter	Symbol	Typical Value
Droplet radius	a	$10\mu\mathrm{m}$
Density of oil	ho	$800 \mathrm{kg/m}^3$
Viscosity of oil	μ_o	$0.1\mathrm{Pa\cdot s}$
Shear rate	$\dot{\gamma}$	$10^4 \mathrm{s}^{-1}$
Surface tension (W/O)	γ_0	$0.03\mathrm{N/m}$
Dielectric permittivity of oil	ϵ	$3 \cdot 8.85 \times 10^{-12} \mathrm{F/m}$
Surfactant coverage	X	0.1
Surfactant concentration	c_{∞}	$1 \times 10^{-8} \mathrm{mol/m}^2$
Temperature (Room temperature)	T	298 K
Ionic surfactant valence	z_1	+1
Diffusion coefficient	D_s	$10^{-8} \mathrm{m}^2/\mathrm{s}$
Gas constant	R	8.314 J/(mol K)
Faraday constant	F	$96485\mathrm{C/mol}$
Ion mobility (Na ⁺)	\mathcal{M}	$5 \times 10^{-8} \mathrm{m^2/V \cdot s}$

microfluidic and small-scale systems as the one study in this work. The Capillary number, with a value of $Ca = 3.33 \times 10^{-1}$, suggests that the droplet is relatively deformable, meaning that viscous forces are sufficiently large to cause noticeable droplet deformation while surface tension still plays a significant role in maintaining droplet shape.

Table 2 – Typical dimensionless groups.

Parameter	Symbol	Typical Value
Reynolds number	Re	0.008
Capillary number	Ca	0.33
Mason number	Mn	2.85
Elasticity parameter	E	8.26×10^{-4}
Surfactant coverage ratio	X	0.1
Peclet number	Pe	100
Mobility ratio	$R_{\mathcal{M}}$	1.82

The Mason number (Mn = 2.85) is moderate, indicating that the viscous effects dominate over the electric effects. This means that the ionic surfactant concentration is not very high, so electric charges do not create a strong electric field. The elasticity parameter ($E = 8.26 \times 10^{-4}$) is small, indicating that the surface tension is not highly sensitive to variations in surfactant concentration. As a result, even if there is a non-uniform distribution of surfactant on the interface, the resulting surface tension gradients would be small. Consequently, Marangoni currents, which are driven by surface tension gradients, would not play a significant role in the observed phenomena.

The surfactant coverage ratio (X = 0.1) indicates a low level of surfactant at the interface. This value suggests that the interface is far from the saturation condition (maximum packing factor), meaning there is ample space for additional surfactant molecules to be added. The coverage ratio is controllable, as it depends primarily on the amount

of surfactant introduced during droplet preparation. The Péclet number (Pe = 100) suggests that convective transport of surfactant along the droplet interface is much more significant than diffusive transport. Consequently, the surfactant molecules face difficulty in spreading and homogenizing on the droplet surface due to the flow advection. The Mobility ratio ($R_{\mathcal{M}} = 1.82$) indicates that electromigration of ions is more pronounced than ion convection driven by the flow.

3 Formulation for Electrohydrodynamics of Droplets

3.1 Problem Statement

We consider a two-dimensional problem, consisting of a neutrally buoyant droplet with initial radius a suspended in another liquid medium subjected to a uniform electric field, \mathbf{E}_0 . Both fluids are immiscible Newtonian fluids with constant physical properties, and the system is subjected to incompressible flow. The density, electric conductivity, dielectric permittivity, and dynamic viscosity of the fluids are denoted as ρ , σ , ϵ , and μ , respectively, and the subscripts "i" and "o" are used to differentiate between inside and outside the droplet, as illustrated in Fig. 3. No-slip boundary condition is applied at the stationaries upper and lower walls. For the electric potential, Neumann boundary condition $\frac{\partial \psi}{\partial y} = -\mathbf{E}_0$ is applied at the lower and upper walls. The domain is considered to be periodic along the x-direction.

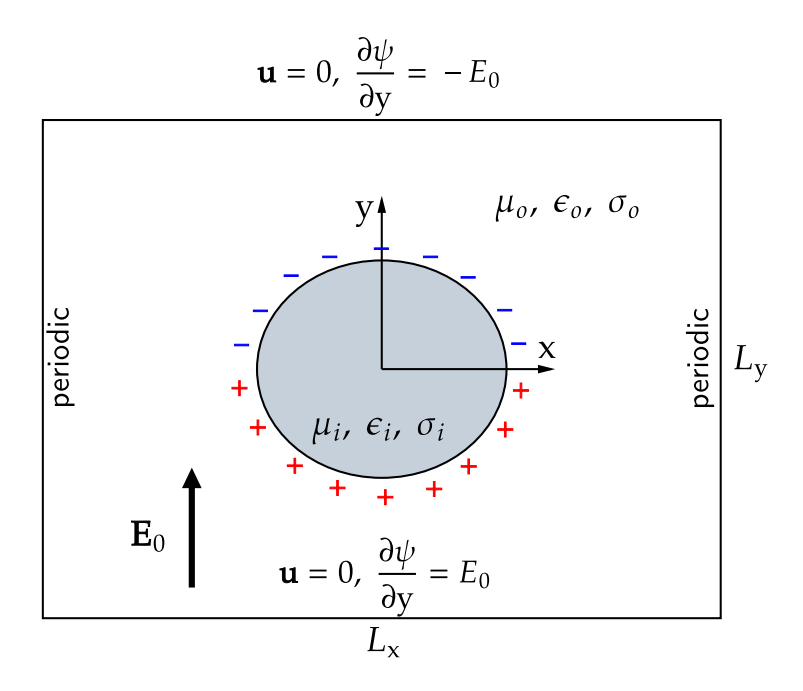


Figure 3 – Schematic diagram of the problem of a droplet suspended in another fluid and subjected to an applied uniform electric field with accumulation of surface charge at the interface; the outer fluid is more conducting than the inner one.

3.2 Governing Equations

3.2.1 Hydrodynamics equations

The Electrohydrodynamic (EHD) problem is governed by the same mass conservation and linear momentum equations as presented in Chapter 2. However, since no tensioactive molecules are present at the interface, there is no tangential stress component due to interfacial tension. The electric stress is accounted for through the full Maxwell stress tensor, since gradients of dielectric permittivity are allowed. The governing equations reduce to:

$$\nabla \cdot \mathbf{u} = 0, \tag{3.1}$$

and

$$\rho \frac{D\mathbf{u}}{Dt} = -\nabla p + \nabla \cdot [\mu(\mathbf{x})(\nabla \mathbf{u} + \nabla \mathbf{u}^{\mathsf{T}})] - \gamma \kappa \delta(\|\mathbf{x} - \mathbf{x}_{\Gamma}\|)\hat{\mathbf{n}} + \mathbf{F}_{E}.$$
(3.2)

The electric force term in Eq. (3.2) will be further discussed in the following section.

3.2.2 Electrostatic equations

In the case of a droplet subjected to an applied electric field, Gauss's Law couples the volumetric charge density with the electric field in the bulk fields,

$$\nabla \cdot (\epsilon \nabla \psi) = -q_v. \tag{3.3}$$

Another important equation that needs to be considered is the charge conservation law,

$$\frac{\partial q_v}{\partial t} + \nabla \cdot \mathbf{J} = 0, \tag{3.4}$$

where $\frac{\partial q_v}{\partial t}$ represents charge relaxation, **J** is the current density vector given by

$$\mathbf{J} = \sigma \mathbf{E} + q_v \mathbf{u},\tag{3.5}$$

where σ is the electric conductivity. The first term at the right-side is the Ohmic charge conduction and the second term corresponds to the electrohydrodynamic flow-induced charge convection (Dong; Sau, 2023). Taking the divergence of Eq. (3.5) and substituing in Eq. (3.4) yields

$$\frac{\partial q_v}{\partial t} + \nabla \cdot (q_v \mathbf{u}) = -\nabla \cdot (\sigma \mathbf{E}). \tag{3.6}$$

3.2.3 Leaky Dielectric Model

In the leaky dielectric model, first introduced by Melcher and Taylor (1969), charges accumulate at the interface almost instantaneously since electrical relaxation time

scale in the bulk fluid is much smaller than the characteristic time of fluid motion. Hence, Eq. (3.6) reduces to

$$\nabla \cdot (\sigma \nabla \psi) = 0, \tag{3.7}$$

where the coupling boundary condition at the interface is given by the continuity of the electric current as follows:

$$[\![\sigma\nabla\psi]\!]_{\Gamma}\cdot\hat{\mathbf{n}} = 0, \tag{3.8}$$

where $[\![\,]\!]$ represents the jump (outer minus inner) across the interface, and $\hat{\mathbf{n}}$ is the outward pointing unit vector.

In order to explore phenomena like transient deformation, surface charge convection, and electrorotation, one can focus on charge conservation specifically along the interface by integrating Eq. (3.4) across the interface, leading to the following surface charge transport equation (Saville, 1997):

$$\frac{\partial q_s}{\partial t} + \nabla_s \cdot (q_s \mathbf{u}) = -[\![\sigma \mathbf{E}]\!] \cdot \hat{\mathbf{n}}, \tag{3.9}$$

where q_s is the surface charge density.

EHD motion arises from the interaction between the electric field and the effective electric charge at the interface. The coupling between hydrodynamics and electrostatics occurs through the stress jump condition at the interface, where the discontinuity in the Maxwell stress gives rise to both normal and tangential force components, governing the interfacial dynamics. These force balances are expressed as follows:

$$[\![\mathbf{M}_{\mathbf{E}} \cdot \hat{\mathbf{n}}]\!] \cdot \hat{\mathbf{n}} = \frac{1}{2} [\![\epsilon (\mathbf{E} \cdot \hat{\mathbf{n}})^2 - \epsilon (\mathbf{E} \cdot \hat{\mathbf{t}})^2]\!], \tag{3.10}$$

and

$$[\![\mathbf{M}_{\mathbf{E}} \cdot \hat{\mathbf{n}}]\!] \cdot \hat{\mathbf{t}} = q_s \mathbf{E} \cdot \hat{\mathbf{t}}. \tag{3.11}$$

Since most leaky dielectric systems have piecewise constant permittivity and conductivity, the electric force is only nonzero in the vicinity of the interface. Therefore, Eq. (2.21) is not appropriate for computing the electric force due to the discontinuity in the electric field and permittivity. To circumvent discontinuity aspects in the formulation, one can consider an interfacial electric force that arises from the jump of the Maxwell stress tensor in the normal direction as:

$$\mathbf{F}_{\mathrm{E}} = [\![\mathbf{M}_{\mathrm{E}} \cdot \hat{\mathbf{n}}]\!] \delta(\|\mathbf{x} - \mathbf{x}_{\Gamma}\|) = \delta(\|\mathbf{x} - \mathbf{x}_{\Gamma}\|) (\mathbf{M}_{\mathrm{E,o}} - \mathbf{M}_{\mathrm{E,i}}) \cdot \hat{\mathbf{n}}, \tag{3.12}$$

where $\mathbf{M}_{E,o}$ and $\mathbf{M}_{E,i}$ represent the Maxwell stress tensor computed as \mathbf{x} approaches \mathbf{x}_{Γ} , from outside and inside the droplet, respectively, and $\delta(\|\mathbf{x} - \mathbf{x}_{\Gamma}\|)$ is the Dirac delta distribution.

As there is no free charge in the bulk in leaky dielectric model, Eq. (3.3) solely becomes

$$\nabla \cdot (\epsilon \nabla \psi) = 0, \tag{3.13}$$

and the surface charge distribution appears in the form of a jump in displacement field condition across the interface expressed by

$$[\![\epsilon \nabla \psi]\!]_{\Gamma} \cdot \hat{\mathbf{n}} = -q_s. \tag{3.14}$$

According to Eq. (3.14), the derivatives of the electric potential are discontinuous. However, the electric potential itself remains continuous across the interface, and enforced by $[\![\psi]\!]_{\Gamma} = 0$.

In this model, two important parameters are defined to quantify the contrast in electric properties between the droplet and its surrounding medium:

$$S = \frac{\epsilon_i}{\epsilon_o}$$
 and $R = \frac{\sigma_i}{\sigma_o}$, (3.15)

where S and R denote the ratios of dielectric permittivity and electric conductivity, respectively.

3.2.4 Nondimensionalization

The governing equations were normalized using the droplet radius a as the characteristic length, μ_o as the characteristic viscosity, E_0 as the characteristic electric field strength, ϵ_o as the characteristic dielectric permittivity, σ_o as the characteristic electric conductivity, $U_{\rm EHD} = \epsilon_o a E_0/\mu_o$ as the characteristic velocity, and $\epsilon_o E_0^2$ as the characteristic pressure. The resulting dimensionless variables are:

$$t^* = \epsilon_o E_0^2 t / \mu_o, \quad \mathbf{x}^* = \mathbf{x}/a, \quad \mathbf{u}^* = \mathbf{u}/U_{\text{EHD}}, \quad p^* = p/(\epsilon_0 E_0^2), \quad \kappa^* = a\kappa, \quad \lambda = \mu/\mu_o,$$

$$\nabla^* = a\nabla, \quad \delta^* = a\delta, \quad \mathbf{E}^* = \mathbf{E}/E_0, \quad \epsilon^* = \epsilon/\epsilon_o, \quad \sigma^* = \sigma/\sigma_o \quad \text{and} \quad q_s^* = q_s/(\epsilon_o E_0)$$
(3.16)

Equations (3.1), (3.2), (3.13) and (3.9) in dimensionless form are:

$$\nabla^* \cdot \mathbf{u}^* = 0, \tag{3.17}$$

$$\operatorname{Re} \frac{D\mathbf{u}^*}{Dt^*} = -\nabla^* p^* + \nabla^* \cdot [\lambda(\mathbf{x})(\nabla^* \mathbf{u}^* + \nabla^* \mathbf{u}^{*\top})] - \frac{1}{\operatorname{Ca}_{\mathrm{E}}} \kappa^* \delta^*(\phi) \mathbf{n} + (\mathbf{M}_{\mathrm{E,o}}^* - \mathbf{M}_{\mathrm{E,i}}^*) \cdot \hat{\mathbf{n}}, \quad (3.18)$$

$$\nabla^* \cdot (\epsilon^* \nabla^* \psi^*) = 0, \quad [\![\epsilon^* \nabla^* \psi^*]\!]_{\Gamma} \cdot \hat{\mathbf{n}} = -q_s^* \cdot$$
(3.19)

$$\frac{\partial q_s^*}{\partial t^*} + \nabla_s^* \cdot (q_s^* \mathbf{u}^*) = \frac{1}{\text{Re}_{\mathbf{E}}} (\mathbf{R} \mathbf{E}_{s,i}^* - \mathbf{E}_{s,o}^*) \cdot \hat{\mathbf{n}}. \tag{3.20}$$

In Eqs. (3.18) and (3.20), the dimensionless groups are:

$$Re = \frac{\rho U_{EHD} a}{\mu_o}, \quad Ca_E = \frac{\epsilon_o a E_0^2}{\gamma} \quad and \quad Re_E = \frac{\epsilon_o U_{EHD}}{\sigma_o a},$$
 (3.21)

where the Reynolds number (Re) measures the relative importance of inertia and viscous forces, and the electric capillary number (Ca_E) relates electric and capillary forces. The electric Reynolds number (Re_E) represents the ratio of charge relaxation $\tau_{e,o} = \epsilon_o/\sigma_o$ to flow $\tau_f = a/U_{\rm EHD}$ times scale (Lanauze; Walker; Khair, 2015).

4 Numerical Methodology

The numerical methodology employed in this work integrates various computational techniques to accurately model both problems: ionic surfactant-covered droplets and electrohydrodynamics of droplets. This chapter starts with a presentation of the finite difference method to approximate spatial derivatives and definition of the computational meshgrid. The level-set method is presented to implicitly capture the evolving droplet interface, with a careful discussion on numerical stability and error minimization. Time integration schemes are discussed, along with the closest point method, which enables the computation of spatial variations and divergences of variables along the interface. Two approaches are presented to model the interface: a sharp-interface approach using the ghost fluid method and a diffuse-interface representation that leverages the level-set framework. The projection method is introduced to solve the governing hydrodynamic equations, with a brief discussion on the numerical treatment of individual force components. Finally, we describe the implementation of surfactant transport and charge conservation equations.

4.1 Finite Difference method

The finite difference method is a numerical technique employed to approximate derivatives by expressing them as differences between finite values and it is largely used to solve differential equations numerically. Various approaches exist for deriving finite difference approximations, including Taylor's series expansion and the derivation of Lagrange interpolating polynomials. However, this section focuses on obtaining derivatives approximations in a more systematic manner using finite difference operators.

4.1.1 Finite difference operators

A finite difference operator is a function $\mathscr{F}: \mathbb{R}^{\mathbb{Z}} \to \mathbb{R}^{\mathbb{Z}}$ that maps a sequence $\{z_i\}_{-\infty}^{\infty} \in \mathbb{R}^{\mathbb{Z}}$ into another sequence $\{z_i^*\}_{-\infty}^{\infty} = \mathscr{F}(\{z_i\}_{-\infty}^{\infty}) \in \mathbb{R}^{\mathbb{Z}}$. The most important operators are defined below:

- a) Shift operator: $\xi z_i = z_{i+1}$;
- b) Forward difference operator: $\Delta_+ z_i = z_{i+1} z_i$;
- c) Backward difference operator: $\Delta_{-}z_{i} = z_{i} z_{i-1}$;
- d) Central difference operator: $\Delta_0 z_i = z_{i+1/2} z_{i-1/2}$;

e) Mean operator:
$$\delta_0 z_i = \frac{z_{i+1/2} + z_{i-1/2}}{2}$$
.

An essential property of these operators is linearity, enabling compositions between them and facilitating algebraic operations such as addition, multiplication, and exponentiation. This feature allows for the rewriting of operators in terms of the *Shift* operator as follows:

$$\Delta_{+} = \xi - \mathcal{I},
\Delta_{-} = \mathcal{I} - \xi^{-1},
\Delta_{0} = \xi^{1/2} - \xi^{-1/2},
\delta_{0} = \frac{\xi^{1/2} + \xi^{-1/2}}{2}.$$
(4.1)

Here, \mathcal{I} represents the identity operator, which preserves the sequence unchanged.

4.1.2 Differential operator

Consider a sequence of values z_i of a function $f : \mathbb{R} \to \mathbb{R}$, defined only at equidistant points x_i separated by Δx , as depicted in Fig. 4, such that

$$\{z_i\}_{-\infty}^{\infty} = \{f(x_i)\}_{-\infty}^{\infty}.$$
 (4.2)

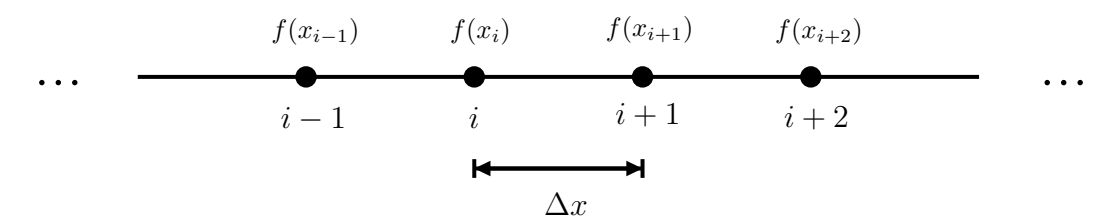


Figure 4 – Schematic representation of a equidistant separated points sequence.

Hence, a differential operator \mathcal{D} can be defined as

$$\mathcal{D}z_i = f'(x_i),\tag{4.3}$$

where higher order derivatives are defined as

$$\mathcal{D}^n z_i = f^{(n)}(x_i). \tag{4.4}$$

The differential operator can also be rewritten in terms of the *shift* operator (Pal, 2007):

$$\mathcal{D} = \frac{1}{\Delta x} \ln \xi. \tag{4.5}$$

For example, to obtain a forward finite difference for the first derivative of $f(x_i)$, one uses the forward operator expressed in Eq. (4.1) and writes Eq. (4.5) as

$$\mathcal{D} = \frac{1}{\Delta x} \ln \left(\mathcal{I} + \Delta_+ \right). \tag{4.6}$$

Using a Taylor's series expansion of the natural logarithm with $\mathcal{I} + \Delta x$ as argument:

$$\mathcal{D} = \frac{1}{\Delta x} \sum_{n=1}^{\infty} (-1)^{n+1} \frac{\Delta_{+}}{n} = \frac{1}{\Delta x} \left[\Delta_{+} - \frac{\Delta_{+}^{2}}{2} + \frac{\Delta_{+}^{3}}{3} - \mathcal{O}(\Delta_{+}^{4}) \right]. \tag{4.7}$$

In Numerical Analysis, it can be proved that every finite difference operators have order Δx , then $\mathcal{O}(\Delta_+^4) \sim \Delta x^4$ (Gupta, 2005). Applying the operator in Eq. (4.7) to z_i , and considering first order approximation $\mathcal{O}(\Delta x)$, yields

$$f'(x_i) = \mathcal{D}z_i = \frac{\Delta_+ z_i}{\Delta x} + \frac{\mathcal{O}(\Delta_+^2)}{\Delta x} = \frac{z_{i+1} - z_i}{\Delta x} + \mathcal{O}(\Delta x). \tag{4.8}$$

Note that Eq. (4.8) is the classic forward finite difference approximation for the first derivative of a discrete function $f(x_i)$.

The backward and central finite difference approximations for the first derivative can be obtained by employing the same formalism using the appropriated finite difference operators, respectively, as (See in Appendix A for detailed derivation).

$$f'(x_i) = \frac{z_i - z_{i-1}}{\Delta x} + \mathcal{O}(\Delta x), \tag{4.9}$$

and

$$f'(x_i) = \frac{z_{i+1} - z_{i-1}}{2\Delta x} + \mathcal{O}(\Delta x^2). \tag{4.10}$$

The forward and backward finite differences are only first order approximations, while the central finite difference has second order accuracy. For the second derivative, a central finite difference (derivation in Appendix B) is given by

$$f''(x_i) = \frac{z_{i+1} - 2z_i + z_{i-1}}{\Delta x^2} + \mathcal{O}(\Delta x^2), \tag{4.11}$$

that is second order accuracy.

4.1.3 Staggered grid

All the governing equations were discretized for two-dimensional uniform meshgrid, consisting in three overlaped staggered grids, as illustrated in Fig. 5. The vector fields x and y components are evaluated at the right (squares) and upper (triangles) faces of the cells, respectively. The scalar quantities and scalar field are evaluated at the center (circles) of the cells. The position of the cells in the x and y directions are determined, respectively, by i and j. The grid is composed of N_x cells in the x-direction and N_y cells in the y-direction. Therefore, there are $N_x \times N_y$ points for scalar fields (central points), $(N_x + 1) \times N_y$ points for vector components in the x-direction, and $N_x \times (N_y + 1)$ points for vector components in the y-direction.

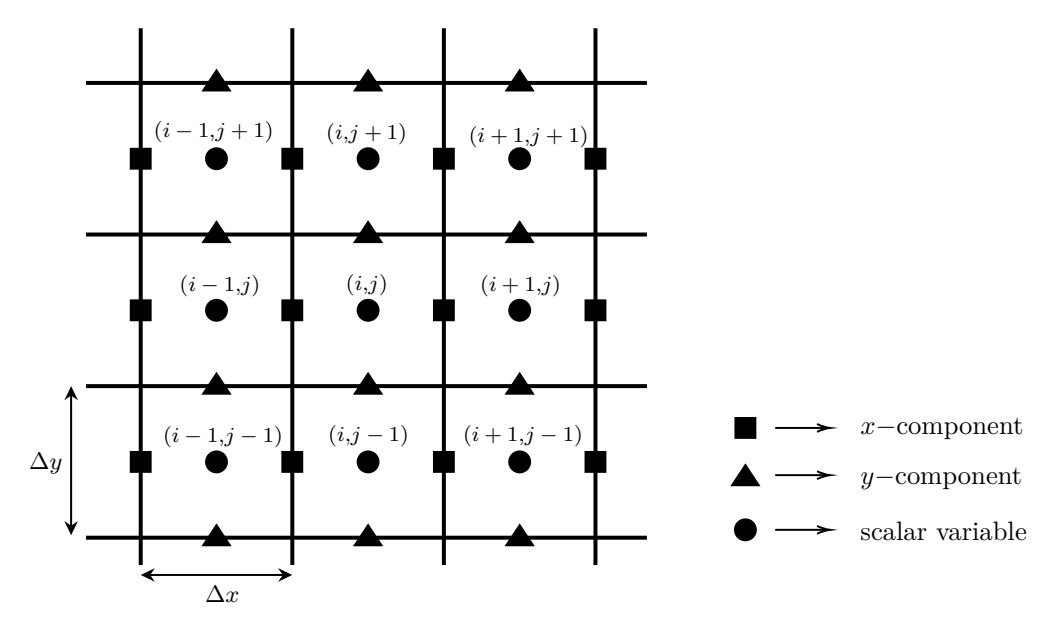


Figure 5 – Staggered grid proposed by Kim and Moin (1985).

4.2 Level Set method

The Level Set method is used to capture and evolve the interface in time. A signed function $\phi = \phi(\mathbf{x}, t)$ is defined to store the distance between each position \mathbf{x} in the domain and its closest point to the interface \mathbf{x}_{Γ} , such that:

$$\begin{cases}
\phi(\mathbf{x}, t) > 0, & \mathbf{x} \in \Omega^+, \\
\phi(\mathbf{x}, t) = 0, & \mathbf{x} \in \Gamma, \\
\phi(\mathbf{x}, t) < 0, & \mathbf{x} \in \Omega^-,
\end{cases}$$
(4.12)

as illustrated in Fig. 6.

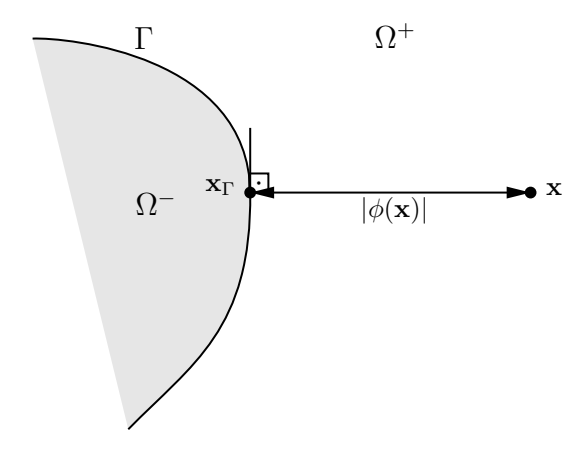


Figure 6 – Representation of the level set function.

The interface is defined by the equation $\phi(\mathbf{x},t) = 0$, while the level set is assumed to represent a conservative material property, satisfying $\frac{D\phi}{Dt} = 0$. As a result, the interface is transported by the flow described by the following advection equation:

$$\frac{\partial \phi}{\partial t} + \mathbf{u} \cdot \nabla \phi = 0. \tag{4.13}$$

The level set function can also be used to smooth properties and prevent abrupt transitions across the interface, effectively defining a diffusive interface. This approach involves considering a narrow layer of thickness 2ε surrounding the interface, within which properties can smoothly transition across the interface as follows

$$\chi_{\varepsilon}(\phi) = \chi_i + (\chi_o - \chi_i) H_{\varepsilon}(\phi), \tag{4.14}$$

where χ is an arbitrary material property such as electric conductivity, dielectric permittivity or dynamic viscosity, and H_{ε} is a smoothed Heaviside function given by

$$H_{\varepsilon}(\phi) = \begin{cases} 0, & \text{if } \phi < -\varepsilon, \\ \frac{1}{2} \left[1 + \frac{\phi}{\varepsilon} + \frac{1}{\pi} \sin\left(\frac{\pi\phi}{\varepsilon}\right) \right], & \text{if } -\varepsilon \le \phi \le \varepsilon, \\ 1, & \text{if } \phi > \varepsilon. \end{cases}$$
(4.15)

The Dirac delta distribution can be obtained by its definition as the directional derivative of the Heaviside function:

$$\delta(\|\mathbf{x} - \mathbf{x}_{\Gamma}\|) = \nabla H(\phi) \cdot \mathbf{n} = \nabla H(\phi) \cdot \frac{\nabla \phi}{|\nabla \phi|} = \frac{\partial H}{\partial \phi} \nabla \phi \cdot \frac{\nabla \phi}{|\nabla \phi|} = \frac{\partial H}{\partial \phi} |\nabla \phi| = \delta(\phi) |\nabla \phi|. \quad (4.16)$$

Here, the outward unit normal vector to the droplet interface can be computed as

$$\hat{\mathbf{n}} = \frac{\nabla \phi}{|\nabla \phi|},\tag{4.17}$$

and the smoothed Dirac delta function is

$$\delta_{\varepsilon}(\phi) = \frac{\partial H_{\varepsilon}(\phi)}{\partial \phi} = \begin{cases} 0, & \text{if } \phi < -\varepsilon, \\ \frac{1}{2\varepsilon} \left[1 + \cos\left(\frac{\pi\phi}{\varepsilon}\right) \right], & \text{if } -\varepsilon \le \phi \le \varepsilon, \\ 0, & \text{if } \phi > \varepsilon. \end{cases}$$
(4.18)

4.2.1 Re-initialization of the level set function

The solution of Eq. (4.13) describes the time evolution of the surface $\Gamma(t)$, representing the propagation of the fluid interface. Although the zero level set of the function ϕ still denotes the surface, this evolution does not ensure that ϕ remains the signed distance function of the interface across the entire domain. Sussman, Smereka and Osher (1994) proposed a technique to reinitialize the level set function, ensuring that it remains a signed distance function of $\Gamma(t)$. This involves reinitializing the level set function ϕ to become a distance function, such that $|\nabla \phi| \approx 1$, by solving the following Hamilton–Jacobi equation until reaching a steady state:

$$\frac{\partial \phi}{\partial \tau} + S(\phi)(|\nabla \phi| - 1) = 0, \tag{4.19}$$

where τ is the pseudo-time and $S(\phi)$ is the sign function of ϕ .

When solving Eq. (4.19), the zero level set needs to be redefined each time. Although this equation alone does not alter the position of the interface, numerical computations introduce accumulated errors each time the interface is re-initialized. To address this issue, Sussman and Fatemi (1999) introduced a constraint to enhance the accuracy of the solution of Eq. (4.19). Given that the interface should remain stationary, the volume should also remain constant. Therefore, Eq. (4.19) is modified as follows:

$$\frac{\partial \phi}{\partial \tau} = \phi_{\tau} = S(\phi)(1 - |\nabla \phi|) + \lambda_m \delta_{\varepsilon}(\phi) |\nabla \phi|, \tag{4.20}$$

where λ_m is a function of τ obtained by imposing

$$\frac{\partial}{\partial \tau} \int_{\Omega} H(\phi) d\Omega' = \int_{\Omega} \delta(\phi) \frac{\partial \phi}{\partial \tau} d\Omega'
= \int_{\Omega} \left[\delta_{\varepsilon}(\phi) S(\phi) (1 - |\nabla \phi|) + \lambda_m \delta_{\varepsilon}^2(\phi) |\nabla \phi| \right] d\Omega' = 0.$$
(4.21)

Hence,

$$\lambda_m = -\frac{\int_{\Omega} \delta_{\varepsilon}(\phi) S(\phi) (1 - |\nabla \phi|) d\Omega'}{\int_{\Omega} \delta_{\varepsilon}^2(\phi) |\nabla \phi| d\Omega'}.$$
 (4.22)

4.2.2 Local Level Set

The level set function is updated using the local level set method (Peng et al., 1999), which involves delimiting a region within the domain where the equations will be solved. Utilizing this approach significantly reduces the computational efforts associated with solving the advection and re-initialization equations of the level set function, while also mitigating numerical issues near the boundaries. Firstly, tubes are created embedding the interface such that

$$T_i = \{\mathbf{x} : |\phi(\mathbf{x})| < \varepsilon_i\} \quad \text{for} \quad i = 1, 2 \text{ and } 3.$$
 (4.23)

A cut-off function $c(\phi)$ is defined as

$$c(\phi) = \begin{cases} 1, & \text{if } |\phi| \le \varepsilon_2, \\ (|\phi| - \varepsilon_3)^2 (2|\phi| + \varepsilon_3 - 3\varepsilon_2) / (\varepsilon_3 - \varepsilon_2)^3, & \text{if } \varepsilon_2 < |\phi| \le \varepsilon_3, \\ 0, & \text{if } |\phi| > \varepsilon_3, \end{cases}$$
(4.24)

to limit computations to the region within the tubes, where $(\varepsilon_1, \varepsilon_2, \varepsilon_3) = (3, 6, 9) \max(\Delta x, \Delta y)$. Hence, the advection equation for the level set function becomes

$$\frac{\partial \phi}{\partial t} + c(\phi)\mathbf{u} \cdot \nabla \phi = 0. \tag{4.25}$$

4.2.3 Time integration

The evolution of the level set function over time is achieved using a third-order Total Variation Diminishing (TVD) Runge-Kutta (RK) method, following the approach outlined by Shu and Osher (1988). This method ensures that the overall order of the solution remains unaffected and offers excellent stability by minimizing error accumulation across iterations. The RK method involves three sequential steps:

$$\begin{cases}
\tilde{\phi}_{i,j}^{n+1} &= \phi_{ij}^{n} - \Delta t \, c(\phi_{ij}^{n}) \, \mathbf{u}_{ij}^{n} \cdot \nabla \phi_{ij}^{n}, \\
\tilde{\phi}_{i,j}^{n+1/2} &= \frac{3}{4} \phi_{ij}^{n} + \frac{1}{4} \tilde{\phi}_{i,j}^{n+1} - \frac{1}{4} \Delta t \, c(\tilde{\phi}_{i,j}^{n+1}) \, \mathbf{u}_{ij}^{n+1} \cdot \nabla \tilde{\phi}_{i,j}^{n+1}, \\
\phi_{i,j}^{n+1} &= \frac{1}{3} \phi_{ij}^{n} + \frac{2}{3} \tilde{\phi}_{i,j}^{n+1/2} - \frac{2}{3} \Delta t \, c(\tilde{\phi}_{i,j}^{n+1/2}) \, \mathbf{u}_{ij}^{n+1/2} \cdot \nabla \tilde{\phi}_{i,j}^{n+1/2}.
\end{cases} \tag{4.26}$$

Here, the superscript n+1 denotes the current time step, while n refers to the previous time step, and n+1/2 represents the mean time between n and n+1. To ensure accurate approximation of spatial derivatives, the convective term $\mathbf{u}_{ij} \cdot \nabla \phi_{ij}$ is computed using a fifth-order Weighted Essentially Non-Oscillatory (WENO) method, combined with Godunov and upwind schemes (Osher; Fedkiw, 2004).

The re-initialization of the level set function follows similar steps to the advection numerical scheme. The time parameter t is replaced by τ , and the initial level set function $\phi_{ij}^{(0)} = \phi_{ij}^{n+1}$ is computed according to Eq. (4.26). Therefore, the re-initialization follows the three steps below:

$$\begin{cases}
\tilde{\phi}_{i,j}^{(1)} = \phi_{ij}^{(0)} - \Delta \tau \, S_{\varepsilon}(\phi_{i,j}^{(0)})(1 - |\nabla \phi_{i,j}^{(0)}|), \\
\tilde{\phi}_{i,j}^{(2)} = \frac{3}{4}\phi_{ij}^{(0)} + \frac{1}{4}\tilde{\phi}_{i,j}^{(1)} - \frac{1}{4}\Delta \tau \, S_{\varepsilon}(\phi_{i,j}^{(1)})(1 - |\nabla \phi_{i,j}^{(1)}|), \\
\phi_{i,j}^{(3)} = \frac{1}{3}\phi_{ij}^{(2)} + \frac{2}{3}\tilde{\phi}_{i,j}^{(2)} - \frac{2}{3}\Delta \tau \, S_{\varepsilon}(\phi_{i,j}^{(2)})(1 - |\nabla \phi_{i,j}^{(2)}|).
\end{cases} (4.27)$$

The complete re-initialization of the level set function concludes with:

$$\phi_{i,j}^{n+1} = \phi_{i,j}^{(3)} + \Delta \tau \lambda_m \delta_{\varepsilon}(\phi_{i,j}^{(0)}). \tag{4.28}$$

In this process, a time step of $\tau = \frac{1}{2}\Delta x$ was chosen, with a total of three reinitialization steps. This implies that the total re-initialization time is $3\Delta \tau$, which is sufficient to reach the steady-state, i.e., when $|\nabla \phi| \approx 1$.

4.3 Closest Point method

The closest point method falls under the category of embedding methods, where a lower-dimensional object is extended to a higher-dimensional space for computational purposes. In the context of this work, the droplet surface is embedded within its surrounding space, simplifying the solution of surface partial differential equations (SPDEs). By treating the surface as part of the surrounding space, standard PDE solution techniques can be applied. This approach allows for the direct application of familiar finite difference methods for discretization and numerical solution (Ruuth; Merriman, 2008).

Consider a function $f(\mathbf{x}_{\Gamma})$ only defined on the surface, where \mathbf{x}_{Γ} represents the Euclidean positions on the surface. An extension operator E is defined such that:

$$E[f(\mathbf{x}_{\Gamma})] = f^*(\mathbf{x}), \tag{4.29}$$

where $f^*(\mathbf{x})$ is the extended function of $f(\mathbf{x}_{\Gamma})$ defined across the entire domain. To effectively utilize the embedding method, the extended function yields gradients along tangential directions only, while remaining constant in normal directions to the surface. This requirement ensures that $E[f(\mathbf{x}_{\Gamma})]$ remains constant along the normal direction to the surface, and it can be achieved through the closest point representation.

For any point \mathbf{x} within the domain Ω , the representation $\mathbf{cp}(\mathbf{x})$ denotes the closest point to \mathbf{x} on the surface as visualized in Fig. 7. It can be observed that the closest point to \mathbf{x}_1 on the interface, labeled as $\mathbf{cp}(\mathbf{x}_1)$, lines up with the position in the normal direction of \mathbf{x}_1 where $\phi = 0$. Also, the distance between \mathbf{x}_1 and $\mathbf{cp}(\mathbf{x}_1)$ is simply the shortest distance between \mathbf{x}_1 and the interface, which is basically the value of the level set function $\phi(\mathbf{x}_1)$.

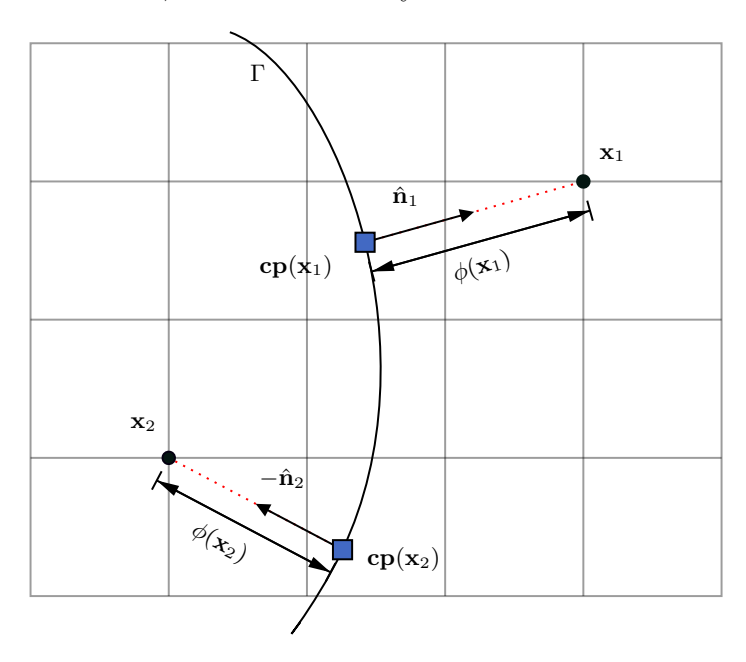


Figure 7 – Geometric representation of the closest point method. The black dots represent points in the grid, while the blue squares indicate their corresponding closest points on the surface.

Therefore, for any function defined on the surface at \mathbf{x}_{Γ} , its constant extension to \mathbf{x} is simply denoted by

$$E[f(\mathbf{x}_{\Gamma})](\mathbf{x}) = f(\mathbf{cp}(\mathbf{x})). \tag{4.30}$$

This approach enables the replacement of surface gradients with standard gradients, facilitating the computation of solutions within the tubes defined by Eq. (4.23) surrounding the surface. For instance,

$$\nabla_s f(\mathbf{x}_{i,j}) = \nabla f(\mathbf{cp}(\mathbf{x}_{i,j})) \tag{4.31}$$

and, for vector or tensor functions, surface divergence becomes

as

$$\nabla_s \cdot \mathbf{F}(\mathbf{x}_{i,j}) = \nabla \cdot \mathbf{F}(\mathbf{cp}(\mathbf{x}_{i,j})). \tag{4.32}$$

The closest point for each grid point \mathbf{x} is simply computed by geometric analysis

$$\mathbf{cp}(\mathbf{x}_{i,j}) = \mathbf{x}_{i,j} - \phi(\mathbf{x}_{i,j})\hat{\mathbf{n}},\tag{4.33}$$

which can be decomposed in x and y components for a cartesian grid:

$$x(\mathbf{cp}(\mathbf{x}_{i,j})) = x_{i,j} - \phi(\mathbf{x}_{i,j})n_x, \tag{4.34}$$

and

$$y(\mathbf{cp}(\mathbf{x}_{i,j})) = y_{i,j} - \phi(\mathbf{x}_{i,j})n_y. \tag{4.35}$$

Since all variable fields are stored at the faces or centers of each cell, they rarely coincide with surface points directly. Therefore, an interpolation step is necessary to obtain the variable values at the required surface points. The choice of interpolation order becomes crucial to minimize interpolation errors, ensuring that the solution is not dominated by these errors as stated by Ruuth and Merriman (2008). In this work, Lagrange two-dimensional interpolation of various orders was utilized. Following the interpolation of variable values on the surface, they were extended to the embedding point grids within the tube region surrounding the interface using the closest point method.

For simplicity, the closest point nomenclature for any grid point $\mathbf{cp}(\mathbf{x}_{i,j})$ will be referred to as $\mathbf{cp}_{i,j}$ in future sections.

4.4 Interface models

In this work, we combine two different models for interface representation, which reflects in how capillary, viscous and electric effects are computed. The diffusive interface model incorporates a finite interfacial region where all quantities are continuous and smoothed, while the Sharp interface model involves abrupt quantity jumps across the interface. Both models are depicted in Fig. 8. The Sharp interface model is specifically employed to compute the electric field using a boundary jump condition, connecting the inner and outer interface domains. Subsequently, we propose a diffusive interface formulation for the electric potential and surface charge density, aiming for a simpler approach to address electrohydrodynamics problems.

4.4.1 Sharp interface model (Ghost Fluid method)

The Ghost Fluid method is a numerical approach used to capture jump conditions in the presence of a sharp interface. In this work, the method developed by Liu, Fedkiw and Kang (2000) was implemented to capture the surface charge jump condition expressed in Eq. (3.14) for solving the electric potential using Eq. (3.13). Employing the standard second order discretization for the variable coefficient Poisson equation in Eq. (3.13), it

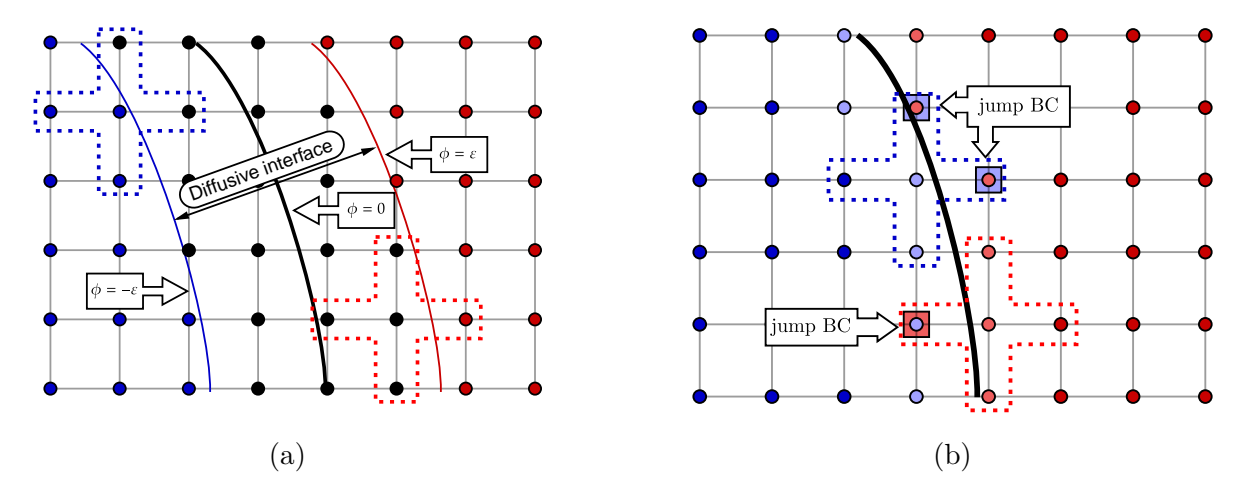


Figure 8 – Schematic representation of interface models used: (a) Diffusive interface: blue dots represent inner region grid points, red dots represent outer region grid points, and black dots represent diffusive interface grid points (2ε thickness). (b) Sharp interface: similar colors to diffusive interface, with light blue and light red dots representing grid points with at least one neighboring grid point on the opposite side of the interface. The blue and red squares represent ghost grid points.

gives

$$\frac{1}{\Delta x} \left[\epsilon_{i+\frac{1}{2},j} \left(\frac{\psi_{i+1,j} - \psi_{i,j}}{\Delta x} \right) - \epsilon_{i-\frac{1}{2},j} \left(\frac{\psi_{i,j} - \psi_{i-1,j}}{\Delta x} \right) \right]
+ \frac{1}{\Delta y} \left[\epsilon_{i,j+\frac{1}{2}} \left(\frac{\psi_{i,j+1} - \psi_{i,j}}{\Delta y} \right) - \epsilon_{i,j-\frac{1}{2}} \left(\frac{\psi_{i,j} - \psi_{i,j-1}}{\Delta y} \right) \right] = 0.$$
(4.36)

A geometric interpretation of the discretization scheme described by Eq. (4.36) is visualized through the five-point stencil discretization depicted by the blue and red dashed lines in Fig. 8, where $\psi_{i,j}$ computation relies on the values of the electric potential at the closest four neighboring grid points. Grid points are categorized as regular or irregular (interface) points. Regular points, indicated by blue and red dots in Fig. 8b, imply that the standard five-point stencil discretization does not intersect the interface, allowing direct application. On the other hand, at irregular points, the stencil cuts through the interface, so it involves grid points both inside and outside the interface, as depicted by the light blue and light red dots in Fig. 8b. Given that the electric potential derivatives are not continuous or smoothed at the interface, the numerical derivative approximation such as $(\psi_{i+1,j} - \psi_{i,j})/\Delta x$ for a irregular grid point is not well-defined and requires special attention.

To provide a reasonable approximation of the derivative near the interface, consider that the interface lies between the nodes (i, j) and (i + 1, j). A subcell resolution θ , as visualized in Fig. 9, can be obtained using the level set function as

$$\theta = \frac{|\phi_{i+1,j}|}{|\phi_{i,j}| + |\phi_{i+1,j}|}.$$
(4.37)

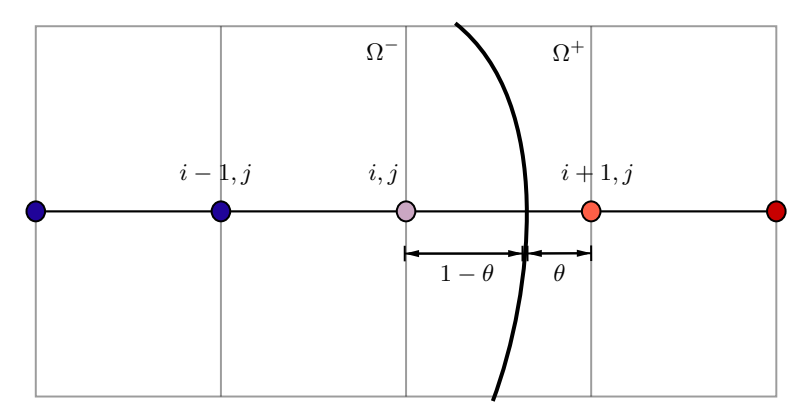


Figure 9 – Subcell resolution.

The use of the subcell resolution allows to calculate a more accurate derivative since the interface location is precisely given by the level set function. The jump condition expressed by Eq. (3.14) can be decompose into two components:

$$\llbracket \epsilon \psi_x \rrbracket = \llbracket \epsilon \psi_n \rrbracket n_x = -q_{\Gamma} n_x, \tag{4.38}$$

and

$$\llbracket \epsilon \psi_u \rrbracket = \llbracket \epsilon \psi_n \rrbracket n_u = -q_{\scriptscriptstyle \Gamma} n_u, \tag{4.39}$$

in which ψ_x , ψ_y and ψ_n denotes the derivative of the electric field in x, y and normal directions, respectively. Although Eqs. (4.38) and (4.39) are not always true, they still correctly capture the jump in the normal direction (Liu; Fedkiw; Kang, 2000). Discretizing Eq. (4.38) according to Fig. 9, it gives

$$\epsilon^{+} \left(\frac{\psi_{i+1,j} - \psi_{I}}{\theta \Delta x} \right) - \epsilon^{-} \left(\frac{\psi_{I} - \psi_{i,j}}{(1 - \theta) \Delta x} \right) = -q_{\Gamma} n_{x}, \tag{4.40}$$

where ψ_I is electric potential at the interface, while ϵ^+ and ϵ^- are the dielectric permittivity in the regions Ω^+ and Ω^- , respectively. Performing algebraic manipulations, Eq. (4.40) leads to two derivatives:

$$\frac{\partial \psi}{\partial x}\Big|_{\Omega^{+}} \approx \frac{\psi_{i+1,j} - \psi_{I}}{\theta \Delta x} = \frac{\hat{\epsilon}}{\epsilon^{+}} \left(\frac{\psi_{i+1,j} - \psi_{i,j}}{\Delta x} \right) - \frac{\hat{\epsilon}q_{\Gamma}n_{x}(1-\theta)}{\epsilon^{+}\epsilon^{-}}, \tag{4.41}$$

and

$$\frac{\partial \psi}{\partial x}\Big|_{\Omega^{-}} \approx \frac{\psi_{I} - \psi_{i,j}}{(1 - \theta)\Delta x} = \frac{\hat{\epsilon}}{\epsilon^{-}} \left(\frac{\psi_{i+1,j} - \psi_{i,j}}{\Delta x} \right) + \frac{\hat{\epsilon}q_{\Gamma}n_{x}\theta}{\epsilon^{+}\epsilon^{-}}, \tag{4.42}$$

where

$$\hat{\epsilon} = \frac{\epsilon^+ \epsilon^-}{\epsilon^+ (1 - \theta) + \epsilon^- \theta}.$$
 (4.43)

Note that Eqs. (4.41) and (4.42) are well-defined derivatives that account for the jump across the interface. Therefore, the derivative in Ω^- can be used to replace the not well-defined derivative $\left(\frac{\psi_{i+1,j}-\psi_{i,j}}{\Delta x}\right)$ in Eq. (4.36) for irregular points giving that:

$$\frac{1}{\Delta x} \left[\hat{\epsilon} \left(\frac{\psi_{i+1,j} - \psi_{i,j}}{\Delta x} \right) + \frac{\hat{\epsilon} q_{\Gamma} n_x \theta}{\epsilon^+} - \epsilon_{i-\frac{1}{2},j} \left(\frac{\psi_{i,j} - \psi_{i-1,j}}{\Delta x} \right) \right]
+ \frac{1}{\Delta y} \left[\epsilon_{i,j+\frac{1}{2}} \left(\frac{\psi_{i,j+1} - \psi_{i,j}}{\Delta y} \right) - \epsilon_{i,j-\frac{1}{2}} \left(\frac{\psi_{i,j} - \psi_{i,j-1}}{\Delta y} \right) \right] = 0.$$
(4.44)

In Eq. (4.44), the second term in the first bracket doesn't depend on the solution, so it can be considered a source term. Then

$$\frac{1}{\Delta x} \left[\hat{\epsilon} \left(\frac{\psi_{i+1,j} - \psi_{i,j}}{\Delta x} \right) - \epsilon_{i-\frac{1}{2},j} \left(\frac{\psi_{i,j} - \psi_{i-1,j}}{\Delta x} \right) \right]
+ \frac{1}{\Delta y} \left[\epsilon_{i,j+\frac{1}{2}} \left(\frac{\psi_{i,j+1} - \psi_{i,j}}{\Delta y} \right) - \epsilon_{i,j-\frac{1}{2}} \left(\frac{\psi_{i,j} - \psi_{i,j-1}}{\Delta y} \right) \right] = -\frac{\hat{\epsilon} q_{\Gamma} n_x \theta}{\epsilon^{+} \Delta x}.$$
(4.45)

Since this source term arises from the jump condition between nodes (i, j) and (i + 1, j), it can be labeled as a source term originating from the right arm of the stencil given by

$$F_R = -\frac{\hat{\epsilon}q_\Gamma n_x \theta}{\epsilon^+ \Delta x}.\tag{4.46}$$

The derivative correction also leads to a replacement in the dielectric permittivity $\epsilon_{i+\frac{1}{2},j}$, in Eq. (4.45), by the effective dielectric permittivity $\hat{\epsilon}$, as defined by Eq. (4.43).

It's important to note that q_{Γ} is available only at the interface, but it can be interpolated using grid point values of $q_{s_{i,j}}$ as

$$q_{\Gamma} = \frac{q_{s_{i,j}} n_{x_{i,j}} |\phi_{i+1,j}| + q_{s_{i+1,j}} n_{x_{i+1,j}} |\phi_{i,j}|}{|\phi_{i+1,j}| + |\phi_{i,j}|}.$$
(4.47)

Equation (4.46) arises from the right-arm of the five-point stencil when $\phi_{i,j} \leq 0$ and $\phi_{i+1,j} > 0$. If $\phi_{i,j} > 0$ and $\phi_{i+1,j} \leq 0$, it would be

$$F_R = \frac{\hat{\epsilon}q_{\Gamma}n_x\theta}{\epsilon^- \Lambda x}.$$
 (4.48)

It could also be $F_R = 0$ if both $\phi_{i,j} \le 0$ and $\phi_{i+1,j} \le 0$ or if both $\phi_{i,j} > 0$ and $\phi_{i+1,j} > 0$.

The same analysis applies to the left, top and bottom arms of the five-points stencil discretization, which provide derivative corrections for all directions. Substituting all the new derivatives in Eq. (4.36) yields to the most general discretization for variable Poisson equation:

$$\frac{1}{\Delta x} \left[\epsilon_{i+\frac{1}{2},j} \left(\frac{\psi_{i+1,j} - \psi_{i,j}}{\Delta x} \right) - \epsilon_{i-\frac{1}{2},j} \left(\frac{\psi_{i,j} - \psi_{i-1,j}}{\Delta x} \right) \right]
+ \frac{1}{\Delta y} \left[\epsilon_{i,j+\frac{1}{2}} \left(\frac{\psi_{i,j+1} - \psi_{i,j}}{\Delta y} \right) - \epsilon_{i,j-\frac{1}{2}} \left(\frac{\psi_{i,j} - \psi_{i,j-1}}{\Delta y} \right) \right] = F_L + F_R + F_B + F_T.$$
(4.49)

Here, F_L , F_R , F_B , and F_T are source terms containing the necessary jump conditions to correct the derivatives. For instance, in Fig 8b, the blue dashed line representing the five-point stencil discretization has two nodes lying on the opposite side of the interface. Consequently, corrections are applied only to the right F_R and top F_T source terms, while the red dashed line stencil shows a need for only the left F_L source term. For those nodes that dont't require correction, the source term remains zero.

A practical algorithm can be implemented to efficiently compute these additional source terms:

- Left-arm of the stencil:
 - 1. If both $\phi_{i,j} \leq 0$ and $\phi_{i-1,j} \leq 0$ or if both $\phi_{i,j} > 0$ and $\phi_{i-1,j} > 0$, then $F_L = 0$. Otherwise, define

$$\theta = \frac{|\phi_{i-1,j}|}{|\phi_{i,j}| + |\phi_{i-1,j}|},\tag{4.50}$$

$$\hat{\epsilon} = \frac{\epsilon_{i-1,j}\epsilon_{i,j} (|\phi_{i-1,j}| + |\phi_{i,j}|)}{\epsilon_{i,j}|\phi_{i-1,j}| + \epsilon_{i-1,j}|\phi_{i,j}|},$$
(4.51)

and

$$q_{\Gamma} = \frac{q_{s_{i,j}} n_{x_{i,j}} |\phi_{i-1,j}| + q_{s_{i-1,j}} n_{x_{i-1,j}} |\phi_{i,j}|}{|\phi_{i,j}| + |\phi_{i-1,j}|}.$$
(4.52)

2. If $\phi_{i,j} \leq 0$ and $\phi_{i-1,j} > 0$, then

$$F_L = \frac{\hat{\epsilon}q_{\Gamma}n_x\theta}{\epsilon^+ \Delta x};\tag{4.53}$$

otherwise, if $\phi_{i,j} > 0$ and $\phi_{i-1,j} \leq 0$, then

$$F_L = -\frac{\hat{\epsilon}q_{\Gamma}n_x\theta}{\epsilon^- \Delta x}.$$
 (4.54)

- Top-arm of the stencil:
 - 1. If both $\phi_{i,j} \leq 0$ and $\phi_{i,j+1} \leq 0$ or if both $\phi_{i,j} > 0$ and $\phi_{i,j+1} > 0$, then $F_T = 0$. Otherwise, define

$$\theta = \frac{|\phi_{i,j+1}|}{|\phi_{i,j}| + |\phi_{i,j+1}|},\tag{4.55}$$

$$\hat{\epsilon} = \frac{\epsilon_{i,j+1}\epsilon_{i,j}\left(|\phi_{i,j+1}| + |\phi_{i,j}|\right)}{\epsilon_{i,j}|\phi_{i,j+1}| + \epsilon_{i,j+1}|\phi_{i,j}|},\tag{4.56}$$

and

$$q_{\Gamma} = \frac{q_{s_{i,j}} n_{y_{i,j}} |\phi_{i,j+1}| + q_{s_{i,j+1}} n_{y_{i,j+1}} |\phi_{i,j}|}{|\phi_{i,j}| + |\phi_{i,j+1}|}.$$
(4.57)

2. If $\phi_{i,j} \leq 0$ and $\phi_{i,j+1} > 0$, then

$$F_T = -\frac{\hat{\epsilon}q_{\Gamma}n_y\theta}{\epsilon^+\Delta u};\tag{4.58}$$

otherwise, if $\phi_{i,j} > 0$ and $\phi_{i,j+1} \leq 0$, then

$$F_T = \frac{\hat{\epsilon}q_{\Gamma}n_y\theta}{\epsilon^-\Delta u}.\tag{4.59}$$

- Bottom-arm of the stencil:
 - 1. If both $\phi_{i,j} \leq 0$ and $\phi_{i,j-1} \leq 0$ or if both $\phi_{i,j} > 0$ and $\phi_{i,j-1} > 0$, then $F_B = 0$. Otherwise, define

$$\theta = \frac{|\phi_{i,j-1}|}{|\phi_{i,j}| + |\phi_{i,j-1}|},\tag{4.60}$$

$$\hat{\epsilon} = \frac{\epsilon_{i,j-1}\epsilon_{i,j} \left(|\phi_{i,j-1}| + |\phi_{i,j}| \right)}{\epsilon_{i,j} |\phi_{i,j-1}| + \epsilon_{i,j-1} |\phi_{i,j}|},\tag{4.61}$$

and

$$q_{\Gamma} = \frac{q_{s_{i,j}} n_{y_{i,j}} |\phi_{i,j-1}| + q_{s_{i,j-1}} n_{y_{i,j-1}} |\phi_{i,j}|}{|\phi_{i,j}| + |\phi_{i,j-1}|}.$$
(4.62)

2. If $\phi_{i,j} \leq 0$ and $\phi_{i,j-1} > 0$, then

$$F_B = \frac{\hat{\epsilon}q_{\Gamma}n_y\theta}{\epsilon^+\Delta y};\tag{4.63}$$

otherwise, if $\phi_{i,j} > 0$ and $\phi_{i,j-1} \leq 0$, then

$$F_B = -\frac{\hat{\epsilon}q_{\Gamma}n_y\theta}{\epsilon^-\Delta u}.$$
 (4.64)

The electric field near the interface can also be computed using Eqs. (4.41) and (4.42). In this scenario, where the interface lies between (i,j) and (i+1,j), the derivative provided by these approximations can be stored at the midpoint $(i+\frac{1}{2},j)$. This midpoint corresponds to the node (i,j) for the x-component of the electric field due to the staggered grid arrangement between scalar and vector component quantities. For the y-component, a similar analysis can be conducted.

4.4.2 Smoothed interface model (Continuum surface force)

In contrast to the sharp interface, with the diffusive interface approach the capillary force, which causes a jump in the pressure across the interface, can be continuous and smoothly computed in Eq. (2.35) within the narrow interface. Additionally, the viscous term in Eq. (2.35) also introduces a jump condition due to the discontinuous viscosity coefficient. While various formulations have been proposed to take in account the effects of viscosity, such as the one by Kang, Fedkiw and Liu (2000), implementing them present significant challenges. To address these complexities, the diffusive interface model offers an appealing framework that simplifies implementation by considering a continuum surface force. This same approach can be extended to the electric force $\mathbf{F}_{\rm E}$ in Eq. (2.35) and the ohmic conduction in Eq. (3.20).

In this formulation, the volumetric charge density can be distributed within the diffusive interface using the Dirac delta distribution. Consequently, it can be expressed in terms of the surface charge density as:

$$q_v = q_s \delta(\|\mathbf{x} - \mathbf{x}_{\Gamma}\|) = q_s \delta(\phi) |\nabla \phi|. \tag{4.65}$$

This allows us to rewrite Eq. (2.17) as:

$$\nabla \cdot (\epsilon \nabla \psi) = -q_s \delta(\phi) |\nabla \phi|. \tag{4.66}$$

Here, the electric field $\mathbf{E} = -\nabla \psi$ is continuous across the interface. Then, Eq. (4.66) can be discretized using ordinary Finite Difference schemes.

From Eq. (3.6), the ohmic conduction term on the right-side can be manipulated using the Level Set properties in order to obtain a modified surface charge transport equation (See Appendix E for detailed derivation):

$$\frac{\partial q_s^*}{\partial t^*} + \nabla_s^* \cdot (q_s^* \mathbf{u}^*) = \frac{1}{\text{Re}_E} \left\{ \frac{\sigma_s^*}{\epsilon_s^*} \left[(1 - S) \mathbf{E}_s^* \cdot \hat{\mathbf{n}} - q_s^* \right] + (R - 1) \mathbf{E}_s^* \cdot \hat{\mathbf{n}} \right\}, \tag{4.67}$$

where σ_s^* , ϵ_s^* and \mathbf{E}_s^* are the electric conductivity, dielectric permittivity, and electric field in dimensionless form computed at the droplet surface, i.e., at $\phi = 0$.

An advantage of using Eq. (4.67) over Eq. (3.20) is its lack of discontinuities in any variable or property, which simplifies direct implementation. However, a disadvantage arises from the finite thickness of the interface (ε), where $\varepsilon \sim \mathcal{O}(\Delta x)$, resulting in only a few grid points available to compute local properties within the diffusive interface. This limitation can lead to inaccuracies, particularly when the ratio between inner and outer properties is too large or small, resulting in steep gradients that may be miscalculated.

4.5 Spatial discretization of the electric potential field equation

The complete discretization and rearrangement of Eq. (4.49) leads to a linear system of equations given by

$$a_{\psi_{i,j}}\psi_{i-1,j} + b_{\psi_{i,j}}\psi_{i,j-1} + c_{\psi_{i,j}}\psi_{i,j} + d_{\psi_{i,j}}\psi_{i+1,j} + e_{\psi_{i,j}}\psi_{i,j+1} = f_{\psi_{i,j}},$$
(4.68)

in which the coefficients are

$$a_{\psi_{i,j}} = \frac{\epsilon_{i-\frac{1}{2},j}}{\Delta x^2}, \ b_{\psi_{i,j}} = \frac{\epsilon_{i,j-\frac{1}{2}}}{\Delta y^2}, \ d_{\psi_{i,j}} = \frac{\epsilon_{i+\frac{1}{2},j}}{\Delta x^2}, \ e_{\psi_{i,j}} = \frac{\epsilon_{i,j+\frac{1}{2}}}{\Delta y^2},$$
 (4.69)

$$c_{\psi_{i,j}} = -\frac{\epsilon_{i-\frac{1}{2},j} + \epsilon_{i+\frac{1}{2},j}}{\Delta x^2} - \frac{\epsilon_{i,j-\frac{1}{2}} + \epsilon_{i,j+\frac{1}{2}}}{\Delta y^2} \quad \text{and} \quad f_{\psi_{i,j}} = F_{L_{i,j}} + F_{R_{i,j}} + F_{B_{i,j}} + F_{T_{i,j}}.$$

As in the sharp interface model the dielectric permittivity ϵ is piecewise constant, it can only assume values 1 or S depending on which side of the interface the nodes $(i-\frac{1}{2},j),\ (i+\frac{1}{2},j),\ (i,j-\frac{1}{2})$ and $(i,j+\frac{1}{2})$ lie on. For the smoothed interface model, the dielectric permittivity is a continuous function of the level set function, i.e, $\epsilon = \epsilon_{\varepsilon}(\phi)$, then, for the same intermediary nodes, it can be computed by taking an harmonic average of neighboring points to avoid instabilities. In addition, the right-side inhomogeneity in Eq. (4.68) takes into account the presence of diffusive charge density as seen in Eq. (4.66) and becomes

$$f_{\psi_{i,j}} = -q_{s_{i,j}}\delta(\phi_{i,j})|\nabla\phi_{i,j}|. \tag{4.70}$$

The boundary conditions for the electric potential problem are heterogeneous Neumann conditions, defined by the prescribed normal derivative at each boundary as visualized in Fig. 3. At the top and bottom boundaries, $\frac{\partial \psi}{\partial y}\Big| = -E_{0y}$ which can be simply discretized using finite difference scheme, leading to:

$$\frac{\psi_{1:N_x,N_y+1} - \psi_{1:N_x,N_y}}{\Delta y} = -\mathbf{E}_{0y} \tag{4.71}$$

and

$$\frac{\psi_{1:N_x,1} - \psi_{1:N_x,0}}{\Delta y} = -\mathbf{E}_{0y},\tag{4.72}$$

where $(1:N_x,N_y+1)$ and $(1:N_x,0)$ are ghost points placed outside the domain as shown in Fig. 10.

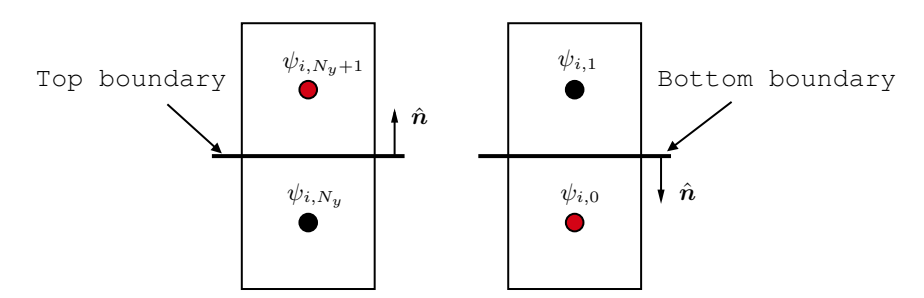


Figure 10 – Top and bottom boundaries representation. The red dots represent points outside the domain (ghost points), while the black dots represent points inside the domain.

Applying Eqs. (4.71) and (4.72) in Eq. (4.68), the coefficients of the linear system change accordingly with

$$\begin{cases}
c_{\psi_{1:N_x,N_y}} = c_{\psi_{1:N_x,N_y}} + e_{\psi_{1:N_x,N_y}}, \\
\psi_{1:N_x,N_y+1} = -\Delta y \mathcal{E}_{0y}
\end{cases}$$
(4.73)

and

$$\begin{cases}
c_{\psi_{1:N_x,1}} = c_{\psi_{1:N_x,1}} + b_{\psi_{1:N_x,1}}, \\
\psi_{1:N_x,0} = \Delta y \mathcal{E}_{0y}.
\end{cases}$$
(4.74)

For the right and left boundaries, the same process can be employed applying the electric field component E_{0x} .

4.6 Projection method

A significant challenge in solving transient incompressible flow problems arises from the strong interdependency between pressure and velocity fields, coupled with the absence of a direct equation for pressure. In contrast, compressible flows involve variations in thermodynamic properties such as temperature and density, demanding the solution of the energy equation to fully close the problem, while a pressure-velocity coupling is enforced by the continuity equation in incompressible flows. To address this difficulty, one alternative is to employ projection methods, which enable the decoupling of pressure and velocity calculations in distinct steps.

In this presented projection method, the computation of velocity and pressure fields occurs in two distinct stages. Initially, a trial velocity field is computed, not considering the influence of pressure and the incompressibility condition, resulting in an intermediate velocity field, \mathbf{u}^* . In the second stage, the trial velocity field is projected in the space

of the vector fields with zero divergences to calculate the trial pressure. From there, the correction of the pressure and velocity fields is made satisfying the incompressibility condition, obtaining p and \mathbf{u} .

A semi-explicit strategy is employed to address the variable ratio of viscosity, which works well for diffusion-dominated equations (Badalassi; Ceniceros; Banerjee, 2003). It consists in adding $\frac{\bar{\lambda}}{2\text{Re}}\nabla^2\mathbf{u}^*$ and subtracting $\frac{\bar{\lambda}}{2\text{Re}}\nabla^2\tilde{\mathbf{u}}^{n+1}$ in the right-side of Eq. (2.35), where \mathbf{u}^* is treated implicitly and $\tilde{\mathbf{u}}^{n+1}$ explicitly by extrapolation. Also, $\bar{\lambda}$ is constant in space given by $\bar{\lambda} = \max\{1, \lambda_{\varepsilon}(\phi)\}$. This approach results in a stable scheme under the standard CFL condition (Xu; Yang; Lowengrub, 2012a).

Using the strategy described above with a semi-explicit Crank-Nicolson scheme for time discretization, Eq. (2.35) can be split into two equations following:

$$\frac{\mathbf{u}^* - \mathbf{u}^n}{\Delta t} = -\left[(\mathbf{u} \cdot \nabla) \mathbf{u} \right]^{n + \frac{1}{2}} + \frac{1}{\text{Re}} \nabla \cdot \left[\lambda_{\epsilon}(\phi) (\nabla \mathbf{u} + \nabla \mathbf{u}^{\top}) \right]^{n + \frac{1}{2}} + \frac{\bar{\lambda}}{2\text{Re}} \nabla^2 \mathbf{u}^* - \frac{\bar{\lambda}}{2\text{Re}} \nabla^2 \tilde{\mathbf{u}}^{n+1} - \frac{1}{\text{CaRe}} \left[\kappa \nabla \phi \delta_{\epsilon}(\phi) \right]^{n + \frac{1}{2}} + \frac{1}{\text{Re}} \left[(\mathbf{M}_{E,o} - \mathbf{M}_{E,i}) \cdot \hat{\mathbf{n}} \right]^{n + \frac{1}{2}},$$
(4.75)

and

$$\frac{\mathbf{u}^{n+1} - \mathbf{u}^*}{\Delta t} = -\nabla \chi^{n+1},\tag{4.76}$$

in which Δt is the time step, χ is the auxiliary pressure field. The right-side terms available at $n + \frac{1}{2}$ in Eq. (4.75) are extrapolated using Adams-Bashforth formula given by

$$\mathfrak{f}^{n+\frac{1}{2}} = \frac{3}{2}\mathfrak{f}^n - \frac{1}{2}\mathfrak{f}^{n-1}. (4.77)$$

For example, the convective term becomes $[(\mathbf{u} \cdot \nabla)\mathbf{u}]^{n+\frac{1}{2}} = \frac{3}{2}[(\mathbf{u} \cdot \nabla)\mathbf{u}]^n - \frac{1}{2}[(\mathbf{u} \cdot \nabla)\mathbf{u}]^{n-1}$. The explicit diffusive term in Eq. (4.75) is also extrapolated simply by

$$\frac{\bar{\lambda}}{2\text{Re}} \nabla^2 \tilde{\mathbf{u}}^{n+1} = \frac{\bar{\lambda}}{2\text{Re}} [2\nabla^2 \tilde{\mathbf{u}}^n - \nabla^2 \tilde{\mathbf{u}}^{n-1}]. \tag{4.78}$$

In order to obtain an equation for the auxiliary pressure, one can proceed taking the divergence of Eq. (4.76), and enforcing incompressibilty condition for \mathbf{u}^{n+1} , resulting in the Poisson equation:

$$\nabla^2 \chi^{n+1} = \frac{\nabla \cdot \mathbf{u}^*}{\Delta t}.$$
 (4.79)

After solving Eq. (4.75) to obtain \mathbf{u}^* and Eq. (4.79) to obtain χ , the velocity at the next step \mathbf{u}^{n+1} can be obtained using Eq. (4.76). The final step involves summing Eqs. (4.75) and (4.76) to derive an explicit update equation for pressure:

$$p^{n+1} = \chi^{n+1} - \frac{\nabla \cdot \mathbf{u}^*}{\text{Re}}.$$
 (4.80)

4.6.1 Spatial discretization of the momentum equation

The governing equations are spatially discretized using finite difference method as described in section 4.1. Hence, the first Eq. (4.75) of the projection method becomes

$$\mathbf{u}_{i,j}^* - \frac{\bar{\lambda}\Delta t}{2\mathrm{Re}}\nabla^2\mathbf{u}_{i,j}^* = \mathbf{u}_{i,j}^n + \Delta t\left(\mathbf{\mathcal{G}}(\mathbf{u}^n, \mathbf{u}^{n-1})_{i,j} + \frac{1}{\mathrm{CaRe}}\mathbf{F}_{s_{i,j}}^{n+\frac{1}{2}} + \frac{1}{\mathrm{Re}}\mathbf{F}_{\mathrm{E}_{i,j}}^{n+\frac{1}{2}}\right),\tag{4.81}$$

in which

$$\mathcal{G}(\mathbf{u}^{n}, \mathbf{u}^{n-1})_{i,j} = -\left[(\mathbf{u} \cdot \nabla)\mathbf{u}\right]^{n+\frac{1}{2}} + \frac{1}{\mathrm{Re}}\nabla \cdot \left[\lambda_{\epsilon}(\phi)(\nabla \mathbf{u} + \nabla \mathbf{u}^{\mathsf{T}})\right]^{n+\frac{1}{2}} - \frac{\bar{\lambda}}{2\mathrm{Re}}\nabla^{2}\tilde{\mathbf{u}}^{n+1}, (4.82)$$

$$\mathbf{F}_{s_{i,j}}^{n+\frac{1}{2}} = \kappa_{i,j}^{n+\frac{1}{2}} \nabla \phi_{i,j}^{n+\frac{1}{2}} \delta_{\varepsilon}(\phi_{i,j}^{n+\frac{1}{2}})$$
(4.83)

and

$$\mathbf{F}_{\mathrm{E}_{i,j}}^{n+\frac{1}{2}} = \mathbf{M}_{\mathrm{E},\mathrm{o}_{\mathrm{i},\mathrm{j}}}^{n+\frac{1}{2}} \cdot \hat{\mathbf{n}}_{i,j}^{n+\frac{1}{2}} - \mathbf{M}_{\mathrm{E},\mathrm{i}_{\mathrm{i},\mathrm{j}}}^{n+\frac{1}{2}} \cdot \hat{\mathbf{n}}_{i,j}^{n+\frac{1}{2}}.$$
 (4.84)

The complete discretization of Eq. (4.81) in the x-direction leads to a linear system for the trial velocity, which takes the form of:

$$a_{u_{i,j}}u_{i-1,j}^* + b_{u_{i,j}}u_{i,j-1}^* + c_{u_{i,j}}u_{i,j}^* + d_{u_{i,j}}u_{i+1,j}^* + e_{u_{i,j}}u_{i,j+1}^* = f_{u_{i,j}}, \tag{4.85}$$

where the coefficients are given as

$$a_{u_{i,j}} = d_{u_{i,j}} = -\frac{\bar{\lambda}\Delta t}{2\operatorname{Re}\Delta x^{2}}, \quad b_{u_{i,j}} = e_{u_{i,j}} = -\frac{\bar{\lambda}\Delta t}{2\operatorname{Re}\Delta y^{2}},$$

$$c_{u_{i,j}} = 1 + \frac{\bar{\lambda}\Delta t}{2\operatorname{Re}\Delta x^{2}} + \frac{\bar{\lambda}\Delta t}{2\operatorname{Re}\Delta y^{2}} \quad \text{and}$$

$$f_{u_{i,j}} = u_{i,j}^{n} + \Delta t \left(\mathcal{G}(u_{i,j}^{n}, u_{i,j}^{n-1}) + \frac{1}{\operatorname{CaRe}} F_{s_{x}i,j}^{n+\frac{1}{2}} + \frac{\operatorname{Ca}_{E}}{\operatorname{CaRe}} F_{E_{x}i,j}^{n+\frac{1}{2}} \right).$$

$$(4.86)$$

The inhomogeneous term \mathcal{G} is discretized as

$$\begin{split} \mathcal{G}\left(u_{i,j}^{n},u_{i,j}^{n-1}\right) &= -\frac{3}{2}\left[u_{i,j}^{n}\left(\frac{\partial u^{n}}{\partial x}\right) + \frac{(v_{i+1,j}^{n} + v_{i,j}^{n} + v_{i+1,j-1}^{n} + v_{i,j-1}^{n})}{4}\left(\frac{\partial u^{n}}{\partial y}\right)\right] \\ &+ \frac{1}{2}\left[u_{i,j}^{n-1}\left(\frac{\partial u^{n-1}}{\partial x}\right) + \frac{(v_{i,j}^{n-1} + v_{i+1,j}^{n-1} + v_{i+1,j-1}^{n-1} + v_{i,j-1}^{n-1})}{4}\left(\frac{\partial u^{n-1}}{\partial y}\right)\right] \\ &+ \frac{3}{2\mathrm{Re}}\left[\frac{2\lambda_{\epsilon}(\phi_{i+1/2,j}^{n})(u_{i+1,j}^{n} - u_{i,j}^{n}) - 2\lambda_{\epsilon}(\phi_{i-1/2,j}^{n})(u_{i,j}^{n} - u_{i-1,j}^{n})}{\Delta x^{2}}\right] \\ &+ \frac{3}{2\mathrm{Re}}\left[\frac{\lambda_{\epsilon}(\phi_{i,j+1/2}^{n})(u_{i,j+1}^{n} - u_{i,j}^{n}) - \lambda_{\epsilon}(\phi_{i,j-1/2}^{n})(u_{i,j}^{n} - u_{i,j-1}^{n})}{\Delta y^{2}}\right] \\ &+ \frac{3}{2\mathrm{Re}}\left[\frac{\lambda_{\epsilon}(\phi_{i,j+1/2}^{n-1})(v_{i,j+1}^{n} - v_{i,j}^{n}) - \lambda_{\epsilon}(\phi_{i,j-1/2}^{n-1})(v_{i,j}^{n} - v_{i,j-1}^{n})}{\Delta y^{2}}\right] \\ &- \frac{1}{2\mathrm{Re}}\left[\frac{2\lambda_{\epsilon}(\phi_{i+1/2,j}^{n-1})(u_{i,j+1}^{n-1} - u_{i,j}^{n-1}) - 2\lambda_{\epsilon}(\phi_{i-1/2,j}^{n-1})(u_{i,j}^{n-1} - u_{i-1,j}^{n-1})}{\Delta x^{2}}\right] \\ &- \frac{1}{2\mathrm{Re}}\left[\frac{\lambda_{\epsilon}(\phi_{i,j+1/2}^{n-1})(u_{i,j+1}^{n-1} - u_{i,j}^{n-1}) - \lambda_{\epsilon}(\phi_{i,j-1/2}^{n-1})(u_{i,j}^{n-1} - u_{i,j-1}^{n-1})}{\Delta y \Delta x}\right] \\ &- \frac{1}{2\mathrm{Re}}\left[\frac{\lambda_{\epsilon}(\phi_{i,j+1/2}^{n-1})(v_{i,j+1}^{n-1} - v_{i,j}^{n-1}) - \lambda_{\epsilon}(\phi_{i,j-1/2}^{n-1})(v_{i,j}^{n-1} - v_{i,j-1}^{n-1})}{\Delta y \Delta x}\right] \\ &- \frac{1}{2\mathrm{Re}}\left[\frac{\lambda_{\epsilon}(\phi_{i,j+1/2}^{n-1})(v_{i,j+1}^{n-1} - v_{i,j}^{n-1}) - \lambda_{\epsilon}(\phi_{i,j-1/2}^{n-1})(v_{i,j}^{n-1} - v_{i,j-1}^{n-1})}{\Delta y \Delta x}\right] \\ &+ \frac{\lambda}{2\mathrm{Re}}\left(\frac{u_{i+1,j}^{n} + u_{i,j}^{n} - 2u_{i,j}^{n}}{\Delta x^{2}} + \frac{u_{i,j+1}^{n} + u_{i,j-1}^{n} - 2u_{i,j}^{n-1}}{\Delta y^{2}}\right), \end{split}$$

where the convective term requires upwinding techniques to avoid non-physical oscillations and numerical instabilities. The derivatives $\frac{\partial u}{\partial x}$ and $\frac{\partial u}{\partial y}$ are computed by a second order ENO, which inherently includes upwinding features through the adaptive stencil selection in its construction (Osher; Fedkiw, 2004).

The capillary force per unit volume in Eq. (4.86) is computed as

$$\mathbf{F}_{s_x i, j}^{n + \frac{1}{2}} = -\left(\frac{\kappa_{i+1, j}^{n + \frac{1}{2}} + \kappa_{i, j}^{n + \frac{1}{2}}}{2}\right) \left(\frac{\phi_{i+1, j}^{n + \frac{1}{2}} - \phi_{i, j}^{n + \frac{1}{2}}}{\Delta x}\right) \delta_{\varepsilon} \left(\frac{\phi_{i+1, j}^{n + \frac{1}{2}} + \phi_{i, j}^{n + \frac{1}{2}}}{2}\right), \tag{4.88}$$

where the local mean curvature is

$$\kappa_{i,j} = \frac{n_{x_{i+1,j}} - n_{x_{i-1,j}}}{2\Delta x} + \frac{n_{y_{i,j+1}} - n_{y_{i,j-1}}}{2\Delta y},\tag{4.89}$$

in which

$$n_{x_{i,j}} = \frac{\phi_{i+1,j} - \phi_{i-1,j}}{2\Delta x |\nabla \phi_{i,j}|}$$
(4.90)

and

$$n_{y_{i,j}} = \frac{\phi_{i,j+1} - \phi_{i,j-1}}{2\Delta y |\nabla \phi_{i,j}|},\tag{4.91}$$

with

$$|\nabla \phi_{i,j}| = \sqrt{\left(\frac{\phi_{i+1,j} - \phi_{i-1,j}}{2\Delta x}\right)^2 + \left(\frac{\phi_{i,j+1} - \phi_{i,j-1}}{2\Delta y}\right)^2}.$$
 (4.92)

Meanwhile, x-component of the electric force in Eq. (4.84) is

$$\mathbf{F}_{\mathbf{E}_{x}i,j}^{n+\frac{1}{2}} = \left(\mathbf{M}_{\mathbf{E},\mathbf{o}_{i,j}}^{n+\frac{1}{2}} \cdot \hat{\mathbf{n}}_{i,j}^{n+\frac{1}{2}}\right)_{x} - \left(\mathbf{M}_{\mathbf{E},\mathbf{i}_{i,j}}^{n+\frac{1}{2}} \cdot \hat{\mathbf{n}}_{i,j}^{n+\frac{1}{2}}\right)_{x},\tag{4.93}$$

in which

$$\left(\mathbf{M}_{\mathrm{E,o_{i,j}}}^{n+\frac{1}{2}} \cdot \hat{\mathbf{n}}_{i,j}^{n+\frac{1}{2}}\right)_{x} = \epsilon_{i,j} \left[\mathbf{E}_{\mathrm{n,o}}(\mathbf{c}\mathbf{p}_{i,j}) \mathbf{E}_{x}(\mathbf{c}\mathbf{p}_{i,j}) - \frac{1}{2} |\mathbf{E}_{\mathrm{o}}(\mathbf{c}\mathbf{p}_{i,j})|^{2} n_{x_{i,j}} \right]$$
(4.94)

is the outer Maxwell stress tensor projected onto the normal direction of the surface. For the inner component, it is completely equivalent.

The normal derivative of the electric potential at the closest point approaching from outside the interface gives the opposite normal electric field $E_{n,o}(\mathbf{cp}_{i,j})$, and it can be calculated by the one-side extrapolation formula (Xu, 2012)

$$E_{n,o}(\mathbf{cp}_{i,j}) = -\frac{-5\psi(\mathbf{cp}_{1_{i,j}}) + 8\psi(\mathbf{cp}_{2_{i,j}}) - 3\psi(\mathbf{cp}_{3_{i,j}})}{2\delta_{\psi}\Delta x} + \mathcal{O}(\delta_{\psi}^{2}\Delta x^{2}), \tag{4.95}$$

in which $\mathbf{cp}_{1_{i,j}}$, $\mathbf{cp}_{2_{i,j}}$ and $\mathbf{cp}_{3_{i,j}}$ are the closest points related to three auxiliary level set curves outside of the interface as shown in Fig. 11. Also, the same procedure can be applied using points inside the interface to compute the normal derivative approaching from inside. The parameter δ_{ψ} is an arbitrary positive number used to calibrate the distance between the auxiliary bands in order to avoid instabilities.

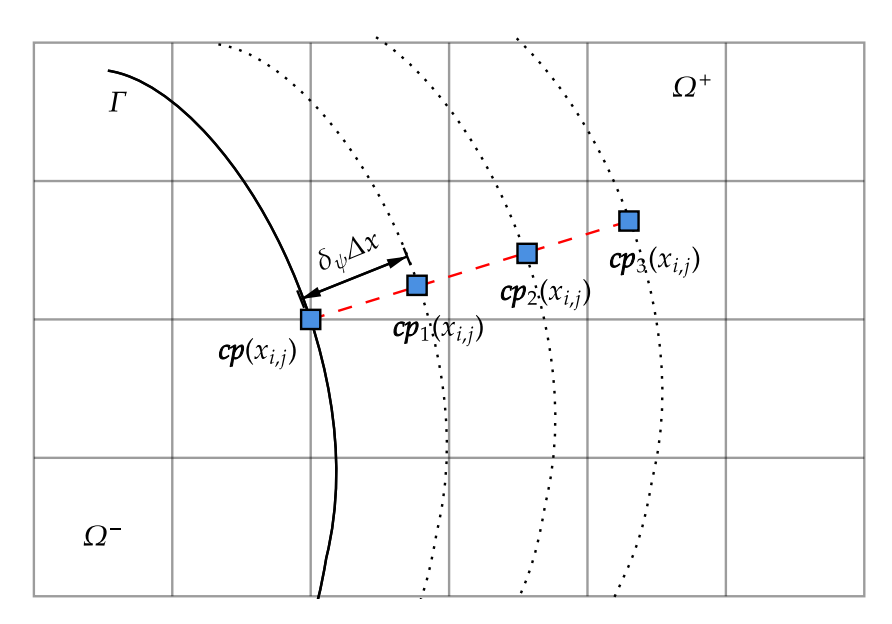


Figure 11 – Normal derivative computed by one-side extrapolation using values of ψ calculated at $\mathbf{cp}_1(x_{i,j})$, $\mathbf{cp}_2(x_{i,j})$ and $\mathbf{cp}_3(x_{i,j})$.

The outer electric field at the closest point to the interface in Eq. (4.94) is calculated as

$$|\mathbf{E}_{o}(\mathbf{c}\mathbf{p}_{i,j})|^{2} = \mathbf{E}_{n,o}(\mathbf{c}\mathbf{p}_{i,j})^{2} + \mathbf{E}_{t}(\mathbf{c}\mathbf{p}_{i,j})^{2}, \tag{4.96}$$

where $E_t(\mathbf{cp}_{i,j})$ is the tangential electric field intensity at the interface. This tangential component does not need to be differentiated between outside and inside because it is continuous across the interface and it can be calculated by taking the surface gradient of the electric potential, i.e, $E_t(\mathbf{x}_{\Gamma}) = -\nabla_s \psi(\mathbf{x}_{\Gamma}) \cdot \hat{\mathbf{t}}$. Hence, using the closest point property to calculate surface gradient as shown in Eq. (4.31), and decomposing the tangential electric field into x and y components to match the adopted Cartesian meshgrid, the latter becomes

$$E_{t}(\mathbf{c}\mathbf{p}_{i,j})\hat{\mathbf{t}} = -\frac{\psi(\mathbf{c}\mathbf{p}_{i+1,j}) - \psi(\mathbf{c}\mathbf{p}_{i-1,j})}{2\Delta x}\hat{\mathbf{i}} + \frac{\psi(\mathbf{c}\mathbf{p}_{i,j+1}) - \psi(\mathbf{c}\mathbf{p}_{i,j-1})}{2\Delta y}\hat{\mathbf{j}}.$$
 (4.97)

Finally, the velocity field is updated using Eq. (4.76), which leads to the discrete equation:

$$u_{i,j}^{n+1} = u_{i,j}^* - \Delta t \left(\frac{\chi_{i+1,j}^{n+1} - \chi_{i,j}^{n+1}}{\Delta x} \right)$$
 (4.98)

4.6.2 Spatial discretization of the pressure equation

The complete discretization of Eq. (4.79) leads to a linear system for the auxiliary pressure, which takes the form of:

$$a_{\chi_{i,j}}\chi_{i-1,j} + b_{\chi_{i,j}}\chi_{i,j-1} + c_{\chi_{i,j}}\chi_{i,j} + d_{\chi_{i,j}}\chi_{i+1,j} + e_{\chi_{i,j}}\chi_{i,j+1} = f_{\chi_{i,j}},$$
(4.99)

where the coefficients are given as

$$a_{\chi_{i,j}} = d_{\chi_{i,j}} = \frac{1}{\Delta x^2}, \quad b_{\chi_{i,j}} = e_{\chi_{i,j}} = \frac{1}{\Delta y^2},$$

$$c_{\chi_{i,j}} = -\frac{2}{\Delta x^2} - \frac{2}{\Delta y^2} \quad \text{and} \quad f_{\chi_{i,j}} = \frac{1}{\Delta t} \left(\frac{u_{i,j}^* - u_{i-1,j}^*}{\Delta x} + \frac{v_{i,j}^* - u_{i,j-1}^*}{\Delta y} \right). \tag{4.100}$$

Discretizing Eq. (4.80) leads to the resulting update equation for the pressure field:

$$p_{i,j}^{n+\frac{1}{2}} = \chi_{i,j}^{n+1} - \frac{1}{2\text{Re}} \left(\frac{u_{i,j}^* - u_{i-1,j}^*}{\Delta x} + \frac{v_{i,j}^* - v_{i,j-1}^*}{\Delta y} \right). \tag{4.101}$$

4.6.3 Boundary and initial conditions

In the case of simple shear flow, periodic boundary conditions are applied to the velocity and pressure fields at the lateral boundaries. At the top and bottom walls of the domain, no-slip conditions are enforced, while the velocity field ${\bf u}$ is subject to non-homogeneous Dirichlet boundary conditions. For the pressure field, homogeneous Neumann boundary conditions are utilized.

Equations (4.85) and (4.99) indicate that for cells located on the domain boundaries (i = 1 or $i = N_x$, j = 1 or $j = N_y$), at least one neighboring cell will fall outside the computational domain $[N_x \times N_y]$. Therefore, ghost nodes—points outside the domain—are introduced, as depicted by the red symbols in Fig. 12. These ghost nodes are essential for applying boundary conditions, a topic that will be elaborated upon in subsequent sections.

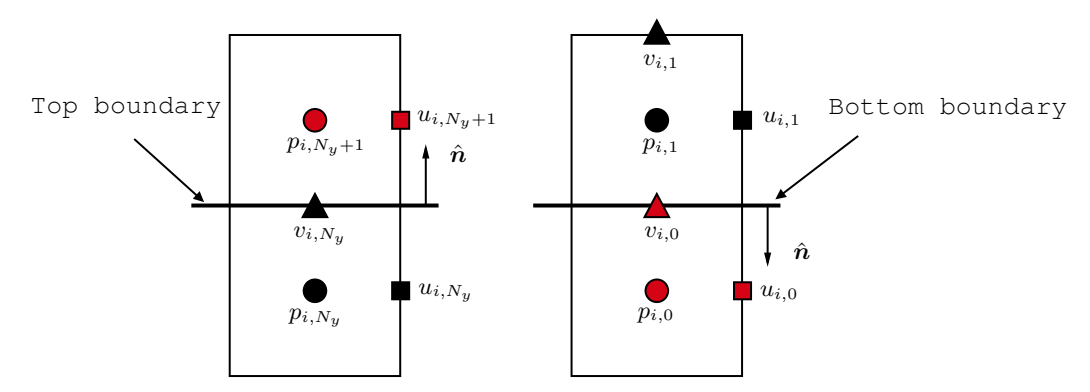


Figure 12 – Top and bottom boundaries representation. The red symbols represent points outside the domain (ghost points), while the black symbols represent points inside the domain.

For the auxiliary and actual and pressure fields, the boundary conditions on the lower and upper walls are defined as $\nabla \chi \cdot \hat{\mathbf{n}} = 0$ and $\nabla p \cdot \hat{\mathbf{n}} = 0$, respectively. The discretization for the auxiliary pressure condition for the lower and upper walls can be expressed in finite differences as:

$$\frac{\chi_{1:N_x,1} - \chi_{1:N_x,0}}{\Delta y} = 0, (4.102)$$

and

$$\frac{\chi_{1:N_x,N_y+1} - \chi_{1:N_x,N_y}}{\Delta y} = 0. (4.103)$$

For the real pressure field p, it is completely equivalent. Those leads to the following ghost point conditions:

$$\begin{cases} \chi_{1:N_x,0} = \chi_{1:N_x,1}, & \text{lower;} \\ p_{1:N_x,0} = p_{1:N_x,1}, & \text{lower;} \\ \chi_{1:N_x,N_y+1} = \chi_{1:N_x,N_y}, & \text{upper;} \\ p_{1:N_x,N_y+1} = p_{1:N_x,N_y}, & \text{upper.} \end{cases}$$

$$(4.104)$$

For the velocity field component u, ghost nodes on the lower and upper boundaries are determined based on the corresponding wall velocities. Figure 12 shows that the lower wall lies between nodes $(1:N_x,0)$ and $(1:N_x,1)$, separated by a distance of $\Delta y/2$. A similar situation exists on the upper wall, between nodes $(1:N_x,n_y)$ and $(1:N_x,n_y+1)$. Consequently, the following conditions apply on the lower and upper walls:

$$U_{\text{south}} = \frac{u_{1:N_x,0} + u_{1:N_x,N_y-1}}{2} \tag{4.105}$$

and

$$U_{\text{north}} = \frac{u_{i,N_y} + u_{i,N_y+1}}{2}.$$
 (4.106)

Thus, the ghost nodes for u and v can be expressed as:

$$\begin{cases} u_{1:N_x,0} = 2U_{\text{south}} - u_{1:N_x,1}, & \text{lower;} \\ u_{1:N_x,N_y+1} = 2U_{\text{north}} - u_{1:N_x,N_y}, & \text{upper;} \\ v_{1:N_x,0} = 0, & \text{lower;} \\ v_{1:N_x,N_y+1} = 0, & \text{upper.} \end{cases}$$

$$(4.107)$$

For the trial velocity field \mathbf{u}^* , it is necessary to relate the boundary conditions of \mathbf{u} and \mathbf{u}^* using Eq. (4.76). This ensures that, on the normal direction relative to the walls:

$$\mathbf{u}^{n+1} \cdot \hat{\mathbf{n}} = \mathbf{u}^* \cdot \hat{\mathbf{n}} - \Delta t (\nabla \chi \cdot \hat{\mathbf{n}})^{n+1}. \tag{4.108}$$

However, on the walls, we have $\nabla \chi \cdot \hat{\mathbf{n}} = 0$. Consequently, the equation simplifies to $\mathbf{u}^{n+1} \cdot \hat{\mathbf{n}} = \mathbf{u}^* \cdot \hat{\mathbf{n}}$, indicating that the boundary conditions for \mathbf{u} can be directly applied to \mathbf{u}^* when the velocity component, u or v, aligns with the normal direction to the wall.

Tangential to the wall, the condition is:

$$\mathbf{u}^{n+1} \cdot \hat{\mathbf{t}} = \mathbf{u}^* \cdot \hat{\mathbf{t}} - \Delta t (\nabla \chi \cdot \hat{\mathbf{t}})^{n+1}. \tag{4.109}$$

Hence, based on Eqs. (4.105) and (4.106), the ghost nodes for \mathbf{u}^* , when the velocity component is tangential to the wall, are defined as:

$$\begin{cases} u_{1:N_x,0}^* = 2U_{\text{south}}^* - u_{1:N_x,1}^*, & \text{lower;} \\ u_{1:N_x,N_y+1}^* = 2U_{\text{north}}^* - u_{1:N_x,N_y}^*, & \text{upper;} \end{cases}$$
(4.110)

where U_{south}^* and U_{north}^* are simply reduced to $U_{\text{s,n}}^*$ and given by:

$$U_{s,n}^* = U_{s,n} + \Delta t \left(\frac{\chi_{i,j+1}^{n+1} - \chi_{i,j}^{n+1}}{\Delta x} \right)$$
 (4.111)

and

$$\chi_{i,j}^{n+1} = 2\chi_{i,j}^n - \chi_{i,j}^{n-1}. (4.112)$$

The boundary conditions on the upper and lower walls modify the coefficients in the governing equations of fluid motion, Eqs. (4.85) and (4.99). Specifically, for the upper wall $(1:N_x,N_y)$:

$$\begin{cases}
c_{u_{i,j}} = c_{u_{i,j}} - e_{u_{i,j}} \\
u_{i,j+1}^* = 2U_{\text{north}}^*, \\
c_{\chi_{i,j}} = c_{\chi_{i,j}} + e_{\chi_{i,j}}, \\
e_{\chi_{i,j}} = 0,
\end{cases}$$
(4.113)

and for the lower wall $(1:N_x,1)$:

$$\begin{cases}
c_{u_{i,j}} = c_{u_{i,j}} - b_{u_{i,j}}, \\
u_{i,j-1}^* = 2U_{\text{south}}^*, \\
c_{\chi_{i,j}} = c_{\chi_{i,j}} + b_{\chi_{i,j}}, \\
b_{\chi_{i,j}} = 0.
\end{cases}$$
(4.114)

On the left and right sides of the domain, periodic boundary conditions are applied. This implies that the flow properties at any given boundary must match those at the opposite boundary, ensuring that even the derivatives are consistent across both boundaries. In the discretization approach adopted here, this consistency is achieved by setting the ghost nodes to have the same values as the internal nodes located adjacent to the opposing boundary, as illustrated in Figure 13.

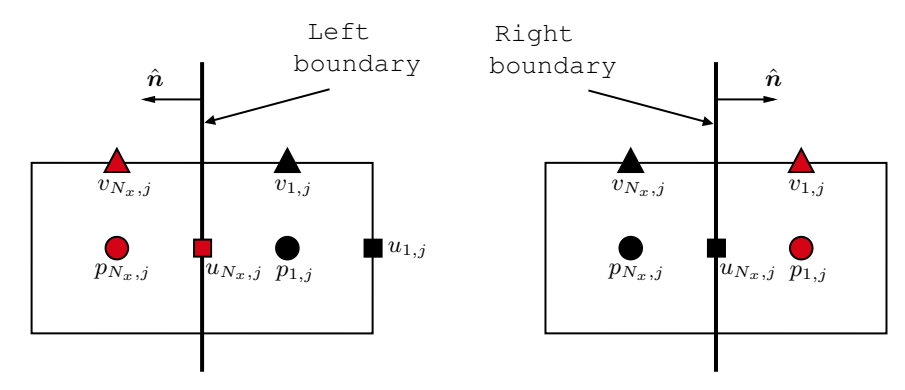


Figure 13 – Representation of left and right periodic boundaries. Ghost points (red symbols) on the left match the domain points (black symbols) on the right, and vice versa, to ensure periodic behavior.

Thus, the ghost nodes for the domain sides can be expressed as:

$$\begin{cases} u_{0,1:N_y}^* = u_{N_x,1:N_y}^*, & \text{left;} \\ u_{N_x+1,1:N_y}^* = u_{1,1:N_y}^*, & \text{right;} \\ v_{0,1:N_y}^* = v_{N_x,1:N_y}^*, & \text{left;} \\ v_{N_x+1,1:N_y}^* = v_{1,1:N_y}^*, & \text{right;} \\ \chi_{0,1:N_y} = \chi_{N_x,1:N_y}, & \text{left;} \\ \chi_{N_x+1,1:N_y} = \chi_{1,1:N_y}, & \text{right.} \end{cases}$$

$$(4.115)$$

The conditions specified in Eq. (4.115) for u^* , v^* , and χ are equally applicable to u, v, and p respectively.

4.7 Discretization of the surfactant transport equation

The surfactant concentration, Eq. (2.38) is evolved by a semi-implicit Crank-Nicholson scheme, similar to that developed by Xu and Zhao (2003), as follows:

$$\frac{c^{n+1} - c^n}{\Delta t} = \left[-\nabla_s \cdot (c\mathbf{u}_s) - c(\nabla_s \cdot \mathbf{n})(\mathbf{u} \cdot \mathbf{n}) \right]^{n+\frac{1}{2}} - \mathcal{R}_{\mathcal{M}} \nabla_s \cdot (c\mathbf{E}_s)^{1+\frac{1}{2}} + \frac{1}{2\mathcal{P}_e} \left(\nabla_s^2 c^{n+1} + \nabla_s^2 c^n \right),$$
(4.116)

The terms evaluated at $n + \frac{1}{2}$ are extrapolated using Adam's Bashforth formula, as described in Eq. (4.77). The diffusive term, although also evaluated at $n + \frac{1}{2}$, is computed as the average between its values at n + 1 and n. The implicit nature of the equation arises from the presence of the diffusive term at n + 1. A distinctive feature of this discretization is that Eq. (4.116) is modified using the closest point method, as proposed by Ruuth and Merriman (2008), where the superficial gradients and divergences are calculated as:

$$\nabla_{s} \cdot (c\mathbf{u}_{s}) = \nabla \cdot \left[c \left(\mathbf{c} \mathbf{p}_{i,j} \right) \mathbf{u}_{s} \left(\mathbf{c} \mathbf{p}_{i,j} \right) \right], \tag{4.117}$$

$$c(\nabla_s \cdot \mathbf{n})(\mathbf{u} \cdot \mathbf{n}) = c\left(\mathbf{c}\mathbf{p}_{i,j}\right) \left[\nabla \cdot \mathbf{n}\left(\mathbf{c}\mathbf{p}_{i,j}\right)\right] \left[\mathbf{u}\left(\mathbf{c}\mathbf{p}_{i,j}\right) \cdot \mathbf{n}\left(\mathbf{c}\mathbf{p}_{i,j}\right)\right],\tag{4.118}$$

$$\nabla_s \cdot (c\mathbf{E}_s) = \nabla \cdot [c(\mathbf{c}\mathbf{p}_{i,j})\mathbf{E}_s(\mathbf{c}\mathbf{p}_{i,j})], \tag{4.119}$$

and

$$\nabla_s^2 c = \nabla^2 c \left(\mathbf{c} \mathbf{p}_{i,j} \right). \tag{4.120}$$

Discretizing the Eq. (4.116) by finite differences and using the closest point method, gives a linear system for the surfactant transport equation:

$$a_{ci,j}c\left(\mathbf{cp}_{i-1,j}^{n+1}\right) + b_{ci,j}c\left(\mathbf{cp}_{i,j-1}^{n+1}\right) + c_{ci,j}c\left(\mathbf{cp}_{i,j}^{n+1}\right) + d_{ci,j}c\left(\mathbf{cp}_{i+1,j}^{n+1}\right) + e_{ci,j}c\left(\mathbf{cp}_{i,j+1}^{n+1}\right) = f_{ci,j},$$

$$(4.121)$$

where the coefficients $a_{ci,j}$, $b_{ci,j}$, $c_{ci,j}$ and $d_{ci,j}$ are, respectively,

$$a_{ci,j} = d_{ci,j} = -\frac{\Delta t}{2 \operatorname{Pe} \Delta x^2},\tag{4.122}$$

$$b_{ci,j} = e_{ci,j} = -\frac{\Delta t}{2 \text{Pe} \Delta y^2},\tag{4.123}$$

$$c_{ci,j} = 1 + \frac{\Delta t}{\text{Pe}\Delta x^2} + \frac{\Delta t}{\text{Pe}\Delta y^2} \tag{4.124}$$

and

$$f_{ci,j} = \frac{3\Delta t}{2} \left\{ -\nabla \cdot \left[c \left(\mathbf{c} \mathbf{p}_{i,j}^{n} \right) \mathbf{u}_{s} \left(\mathbf{c} \mathbf{p}_{i,j}^{n} \right) \right] - c \left(\mathbf{c} \mathbf{p}_{i,j}^{n} \right) \left[\nabla \cdot \mathbf{n} \left(\mathbf{c} \mathbf{p}_{i,j}^{n} \right) \right] \left[\mathbf{u} \left(\mathbf{c} \mathbf{p}_{i,j}^{n} \right) \cdot \mathbf{n} \left(\mathbf{c} \mathbf{p}_{i,j}^{n} \right) \right] - R_{\mathcal{M}} \nabla \cdot \left[c \left(\mathbf{c} \mathbf{p}_{i,j}^{n} \right) \mathbf{E}_{s} \left(\mathbf{c} \mathbf{p}_{i,j}^{n} \right) \right] \right\}$$

$$- \frac{\Delta t}{2} \left\{ -\nabla \cdot \left[c \left(\mathbf{c} \mathbf{p}_{i,j}^{n-1} \right) \mathbf{u}_{s} \left(\mathbf{c} \mathbf{p}_{i,j}^{n-1} \right) \right] - c \left(\mathbf{c} \mathbf{p}_{i,j}^{n-1} \right) \left[\nabla \cdot \mathbf{n} \left(\mathbf{c} \mathbf{p}_{i,j}^{n-1} \right) \right] \left[\mathbf{u} \left(\mathbf{c} \mathbf{p}_{i,j}^{n-1} \right) \cdot \mathbf{n} \left(\mathbf{c} \mathbf{p}_{i,j}^{n-1} \right) \right] - R_{\mathcal{M}} \nabla \cdot \left[c \left(\mathbf{c} \mathbf{p}_{i,j}^{n-1} \right) \mathbf{E}_{s} \left(\mathbf{c} \mathbf{p}_{i,j}^{n-1} \right) \right] \right\}$$

$$+ \frac{\Delta t}{2 \operatorname{Pe}} \nabla^{2} c \left(\mathbf{c} \mathbf{p}_{i,j}^{n} \right) + c_{i}^{n}.$$

$$(4.125)$$

Equation (4.121) is solved by the biconjugate gradient stabilized method. The divergences discretized, regardless of the time step, are given by

$$\nabla \cdot \left[c \left(\mathbf{c} \mathbf{p}_{i,j} \right) \mathbf{u}_{s} \left(\mathbf{c} \mathbf{p}_{i,j} \right) \right] = \frac{c \left(\mathbf{c} \mathbf{p}_{i+1,j} \right) u_{s} \left(\mathbf{c} \mathbf{p}_{i+1,j} \right) - c \left(\mathbf{c} \mathbf{p}_{i-1,j} \right) u_{s} \left(\mathbf{c} \mathbf{p}_{i-1,j} \right)}{2\Delta x} + \frac{c \left(\mathbf{c} \mathbf{p}_{i,j+1} \right) v_{s} \left(\mathbf{c} \mathbf{p}_{i,j+1} \right) - c \left(\mathbf{c} \mathbf{p}_{i,j-1} \right) v_{s} \left(\mathbf{c} \mathbf{p}_{i,j-1} \right)}{2\Delta y}, \tag{4.126}$$

$$\nabla \cdot \left[c \left(\mathbf{c} \mathbf{p}_{i,j} \right) \mathbf{E}_{s} \left(\mathbf{c} \mathbf{p}_{i,j} \right) \right] = \frac{c \left(\mathbf{c} \mathbf{p}_{i+1,j} \right) E_{s,x} \left(\mathbf{c} \mathbf{p}_{i+1,j} \right) - c \left(\mathbf{c} \mathbf{p}_{i-1,j} \right) E_{s,x} \left(\mathbf{c} \mathbf{p}_{i-1,j} \right)}{2\Delta x} + \frac{c \left(\mathbf{c} \mathbf{p}_{i,j+1} \right) E_{s,y} \left(\mathbf{c} \mathbf{p}_{i,j+1} \right) - c \left(\mathbf{c} \mathbf{p}_{i,j-1} \right) E_{s,y} \left(\mathbf{c} \mathbf{p}_{i,j-1} \right)}{2\Delta y}, \tag{4.127}$$

$$c\left(\mathbf{c}\mathbf{p}_{i,j}\right)\left[\nabla \cdot \mathbf{n}\left(\mathbf{c}\mathbf{p}_{i,j}\right)\right]\left[\mathbf{u}\left(\mathbf{c}\mathbf{p}_{i,j}\right) \cdot \mathbf{n}\left(\mathbf{c}\mathbf{p}_{i,j}\right)\right] = c\left(\mathbf{c}\mathbf{p}_{i,j}\right)\kappa\left(\mathbf{c}\mathbf{p}_{i,j}\right)\left[u\left(\mathbf{c}\mathbf{p}_{i,j}\right)n_{x}\left(\mathbf{c}\mathbf{p}_{i,j}\right) + v\left(\mathbf{c}\mathbf{p}_{i,j}\right)n_{y}\left(\mathbf{c}\mathbf{p}_{i,j}\right)\right],$$
(4.128)

and

$$\nabla^{2} c\left(\mathbf{c}\mathbf{p}_{i,j}\right) = \left(\frac{c\left(\mathbf{c}\mathbf{p}_{i-1,j}\right) + c\left(\mathbf{c}\mathbf{p}_{i+1,j}\right) - 2c\left(\mathbf{c}\mathbf{p}_{i,j}\right)}{\Delta x^{2}}\right) + \left(\frac{c\left(\mathbf{c}\mathbf{p}_{i,j-1}\right) + c\left(\mathbf{c}\mathbf{p}_{i,j+1}\right) - 2c\left(\mathbf{c}\mathbf{p}_{i,j}\right)}{\Delta y^{2}}\right).$$

$$(4.129)$$

4.8 Discretization of charge conservation equation

For the electrohydrodynamics problem, a second-order Runge-Kutta method is used to discretize Eq. (3.20) in time, yielding the intermediate values

$$k_1 = \Delta t \left[-\nabla_s \cdot (q_s^n \mathbf{u}^n) + \frac{1}{\text{Re}_{\mathbf{E}}} (\mathbf{R} \mathbf{E}_{s,i}^n - \mathbf{E}_{s,o}^n) \cdot \hat{\mathbf{n}} \right], \tag{4.130}$$

and

$$k_{2} = \Delta t \left\{ -\nabla_{s} \cdot \left[\left(q_{s}^{n} + \frac{k_{1}}{2} \right) \mathbf{u}^{n+\frac{1}{2}} \right] + \frac{1}{\text{Re}_{E}} \left(\mathbf{R} \mathbf{E}_{s,i}^{n+\frac{1}{2}} - \mathbf{E}_{s,o}^{n+\frac{1}{2}} \right) \cdot \hat{\mathbf{n}} \right\}.$$
(4.131)

Then, the updated surface charge density is computed by

$$q_s^{n+1} = q_s^n + k_2. (4.132)$$

The terms evaluated at $n + \frac{1}{2}$ are extrapolated using Adam's Bashforth formula described in Eq. (4.77).

4.9 Numerical methodology for droplet deformation computation

The deformation of a droplet is quantified using the Taylor (1934) deformation parameter, defined as:

$$D = \frac{L - B}{L + B},\tag{4.133}$$

where L represents the droplet's maximum dimension (length) and B its minimum dimension (height). A spherical droplet, where L=B, exhibits a Taylor deformation of zero. As the length significantly exceeds the height $(L\gg B)$, the deformation parameter approaches unity.

To determine the droplet's dimensions and orientation, a computational approach is employed. The droplet's surface points, denoted as \mathbf{x}_{Γ} , are computed in a sequential, counter-clockwise manner. This process enables the determination of both the droplet's size and its surface length.

Initially, the droplet's center, \mathbf{x}_c , is calculated by

$$\mathbf{x}_c = \frac{1}{A} \sum_{i=1}^{N} \mathbf{x}_i \Delta A_i, \tag{4.134}$$

where \mathbf{x}_i is the position vector of each discretized surface element, ΔA_i is the corresponding area element, and $A = \sum_{i=1}^{N} \Delta A_i$ is the total droplet area. Subsequently, the droplet's contour is discretized into n_{θ} points, $\mathbf{x}_{\Gamma} = (x_{\theta_i}, y_{\theta_i})$, each originating from the droplet's center. The position vector of each point forms an angle θ_i , for $i = 1, \ldots, n_{\theta}$, with the reference vector $\mathbf{x}_{\Gamma_{n_{\theta}}} = (0, L_x)$. These points are evenly spaced angularly, such that:

$$\theta_{i+1} = \theta_i + \Delta\theta$$
, where $\Delta\theta = 2\pi/n_{\theta}$. (4.135)

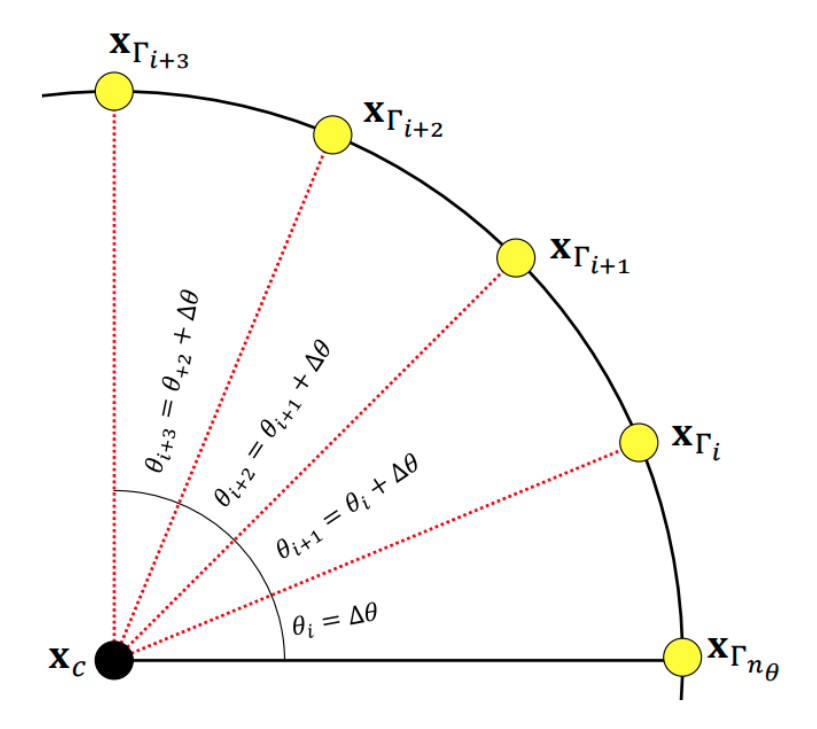


Figure 14 – Geometrical representation of the droplet measure. Each yellow dot on the surface corresponds to an angle θ_i (Pimenta, 2023).

As illustrated in Figure 14, for each angle θ_i , the corresponding surface point \mathbf{x}_{Γ_i} is determined by solving:

$$\begin{cases}
\phi(\mathbf{x}_{\Gamma_i}) = 0, \\
(\mathbf{x}_{\Gamma_i} - \mathbf{x}_c) \times \mathbf{x}_{\theta_i} = 0,
\end{cases}$$
(4.136)

where $\phi(\mathbf{x}_{\Gamma_i})$ represents a function that defines the droplet's surface, and \mathbf{x}_{θ_i} is a reference vector. The solution of this system ensures that the point \mathbf{x}_{Γ_i} lies on the droplet's surface and that the vector connecting the droplet's center \mathbf{x}_c to \mathbf{x}_{Γ_i} is aligned with the direction defined by θ_i .

The angular distribution follows:

$$\theta_i = \Delta \theta, \quad \theta_{i+1} = \theta_i + \Delta \theta, \quad \theta_{i+2} = \theta_{i+1} + \Delta \theta, \quad \theta_{i+3} = \theta_{i+2} + \Delta \theta,$$
 (4.137)

with angular increment $\Delta\theta = 2\pi/n_{\theta}$.

The system of equations (4.136) is solved using the Newton-Raphson method through:

$$\begin{cases} f_1 = \phi(x_{\Gamma_i}, y_{\Gamma_i}) = 0, \\ f_2 = x_{\Gamma_i} y_{\theta_i} - y_{\Gamma_i} x_{\theta_i} - x_c y_{\theta_i} + y_c x_{\theta_i} = 0, \end{cases}$$
(4.138)

where $x_{\theta_i} = \cos \theta_i$ and $y_{\theta_i} = \sin \theta_i$.

The discrete surface points are obtained through these steps:

- 1. Set tolerance tol = 10^{-10} , initialize i = 0, and $\theta_0 = 0$;
- 2. Update angle $\theta_{i+1} = \theta_i + \Delta \theta$. Initialize k = 0 with initial guess $x_{\Gamma_i}^k = x_{\Gamma_{i0}}$ and $y_{\Gamma_i}^k = y_{\Gamma_{i0}}$;

3. Formulate Newton-Raphson system:

$$\begin{pmatrix} \frac{\partial f_1}{\partial x} & \frac{\partial f_1}{\partial y} \\ \frac{\partial f_2}{\partial x} & \frac{\partial f_2}{\partial y} \end{pmatrix} \begin{pmatrix} \delta x_{\Gamma_i} \\ \delta y_{\Gamma_i} \end{pmatrix} = \begin{pmatrix} -f_1 \\ -f_2 \end{pmatrix}, \tag{4.139}$$

specifically:

$$\begin{pmatrix} \frac{\partial \phi}{\partial x}(x_{\Gamma_i}^k, y_{\Gamma_i}^k) & \frac{\partial \phi}{\partial y}(x_{\Gamma_i}^k, y_{\Gamma_i}^k) \\ y_{\theta_i} & -x_{\theta_i} \end{pmatrix} \begin{pmatrix} \delta x_{\Gamma_i}^k \\ \delta y_{\Gamma_i}^k \end{pmatrix} = \begin{pmatrix} -f_1^k \\ -f_2^k \end{pmatrix}; \tag{4.140}$$

- 4. Solve via Cramer's rule for $\delta x_{\Gamma_i}^k$ and $\delta y_{\Gamma_i}^k$;
- 5. Update coordinates:

$$\begin{cases} x_{\Gamma_{i}}^{k+1} = x_{\Gamma_{i}}^{k} + \delta x_{\Gamma_{i}}^{k}, \\ y_{\Gamma_{i}}^{k+1} = y_{\Gamma_{i}}^{k} + \delta y_{\Gamma_{i}}^{k}; \end{cases}$$
(4.141)

- 6. If $|f_1^{k+1}| + |f_2^{k+1}| < \text{tol}$, proceed; else increment k and repeat;
- 7. If $i \neq n_{\theta}$, increment i and repeat from step 2;
- 8. Finalize computation.

The arc-length is computed by summing distances between consecutive \mathbf{x}_{Γ_i} points from Eq. (4.136). The largest and smallest droplet dimensions correspond to the maximum and minimum distances between \mathbf{x}_{Γ_i} and the droplet center \mathbf{x}_c .

5 Results for Ionic Surfactant-Covered Droplets

The results section begins with a convergence analysis of the numerical methods employed using Richardson extrapolation and shows consistent results compared to Xu, Yang and Lowengrub (2012b). Then, a primary verification of the electric formulation for the electric potential is performed by comparing it with the analytical solution for the electric potential of a simple circular droplet. Next, the deformation and shape of ionic and non-ionic surfactant-laden droplets are analyzed and compared with the theoretical predictions of Li and Pozrikidis (1997) and numerical results of Xu, Yang and Lowengrub (2012b). Finally, a more detailed investigation is conducted on the two key parameters introduced in the electric formulation—the Mason number and the mobility ratio—highlighting their roles in Taylor deformation and surfactant distribution.

5.1 Convergence rate

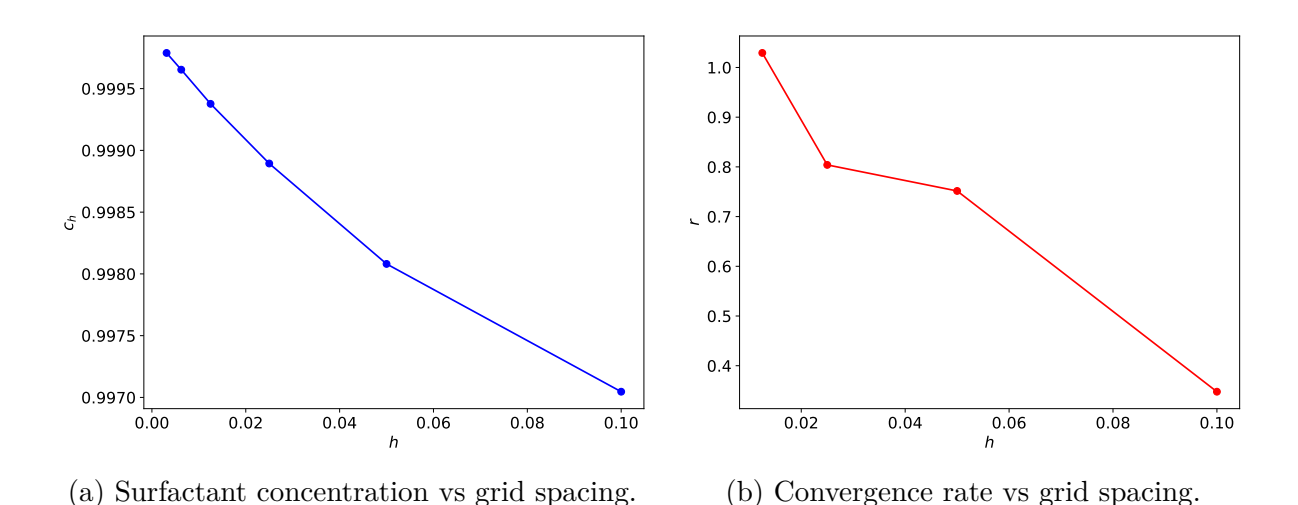


Figure 15 – Convergence analysis for simulations with Re = 0.01, Ca = 0.1, λ = 1, Pe = 10, X = 0.6, and E = 0.2. Surfactant concentration c_h obtained at t = 0.5.

The convergence behavior of the numerical method is analyzed in Fig. 15. The surfactant concentration c_h at x=1 and y=0 as a function of the grid spacing $h=\Delta x=\Delta y$ is visualized in Fig. 15a. The simulations were performed using space grids of $h=0.1,\ 0.05,\ 0.025,\ 0.0125,\ 0.00625,\ and\ 0.003125,\ with a time step of <math>\Delta t=h/8$ for all cases until t=0.5. The nearly linear relationship observed in this plot suggests that the method exhibits first-order convergence with respect to h, i.e., the error decreases

proportionally to h. This is consistent with the expected behavior for methods employing first-order discretization schemes.

The second figure shows the convergence rate r computed using Richardson extrapolation, plotted against h. The convergence rate r is calculated as:

$$r = \log_2\left(\frac{c_h - c_{h/2}}{c_{h/2} - c_{h/4}}\right) + \mathcal{O}(h),\tag{5.1}$$

where c_h , $c_{h/2}$, and $c_{h/4}$ represent the surfactant concentrations computed on grids with spacings h, h/2, and h/4, respectively. As the mesh is refined $(h \to 0)$, the value of r approaches approximately 1.0, which aligns with the ideal value for a first-order method. This result indicates that the numerical method achieves the expected theoretical convergence rate. However, small deviations from the ideal value can still occur due to the coupling of multiple numerical methods, such as the projection method for splitting the Navier-Stokes equations and the closest point method, which involves extensive interpolations around the interface. The interaction between these methods, along with the inherent approximations in their implementation, can introduce minor numerical errors that slightly affect the convergence rate.

The convergence rate of $r \approx 1.0$ demonstrates that the numerical method is robust and provides reliable results, even in the presence of complex coupled physics. This behavior is consistent with findings in the literature, such as those of Xu, Yang and Lowengrub (2012a), who reported similar convergence rates for surfactant transport using advanced numerical techniques. Furthermore, the results align with conventional continuum surface force methods, such as the Immersed Boundary method (see, e.g., Li and Ito (2006)), which also exhibit first-order convergence in practice.

5.2 Comparison of the electric potential

To verify the validation of the electric formulation, the analytical solution of $\nabla^2 \psi = 0$ with the boundary condition $\nabla \psi \cdot \hat{\mathbf{n}} \big|_{\Gamma} = -q_s/\epsilon$ is used as a reference for a circular droplet. At the initial instant of the simulation, while the droplet remains circular, the electric potential is obtained along a line in the y-direction for different domain sizes. As expected, as the domain increases, the numerical solution converges to the analytical solution, which represents a limiting case for an infinite domain, as shown in Fig. 16.

It can be observed that for the $[20 \times 20]$ domain (blue line in Fig. 16), the electric potential matches the analytical solution up to $r \approx 2a$. Beyond this point, the presence of the homogeneous Neumann boundary condition at the top and bottom walls (y = 10 and y = -10) causes significant interference in the electric potential. For larger domains, the perturbation due to the walls is significantly reduced. The electric potential could be obtained from any radial direction with consistent results for larger domains. However,

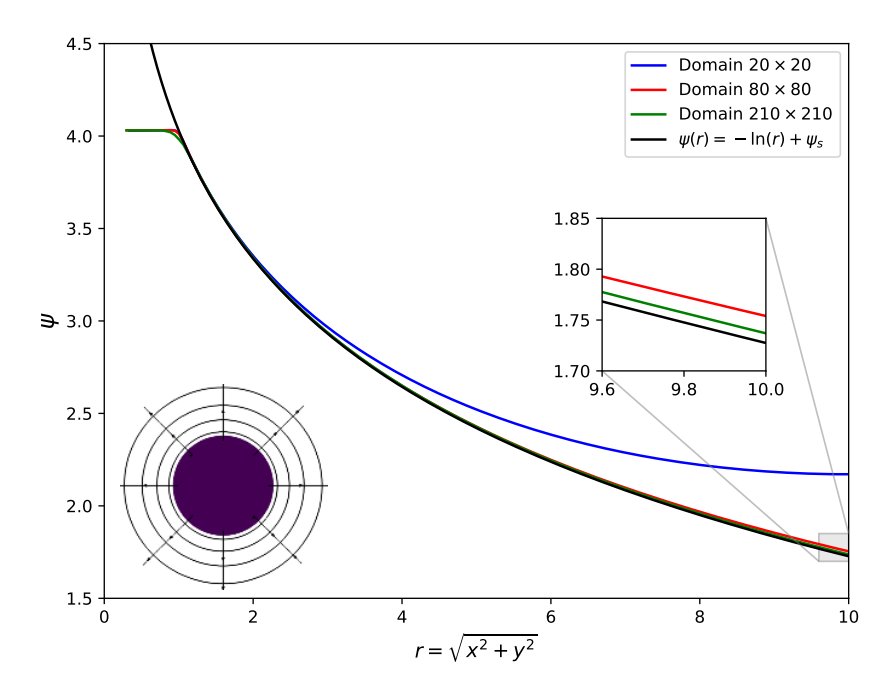


Figure 16 – Comparison between the numerical electric potential field in y-direction with the analytical 1D solution for a circular geometry. The inset depicts a circular droplet with concentric electric potential contours and radial electric field vectors.

for smaller domains, the periodic boundary conditions in the x-direction introduce some interference.

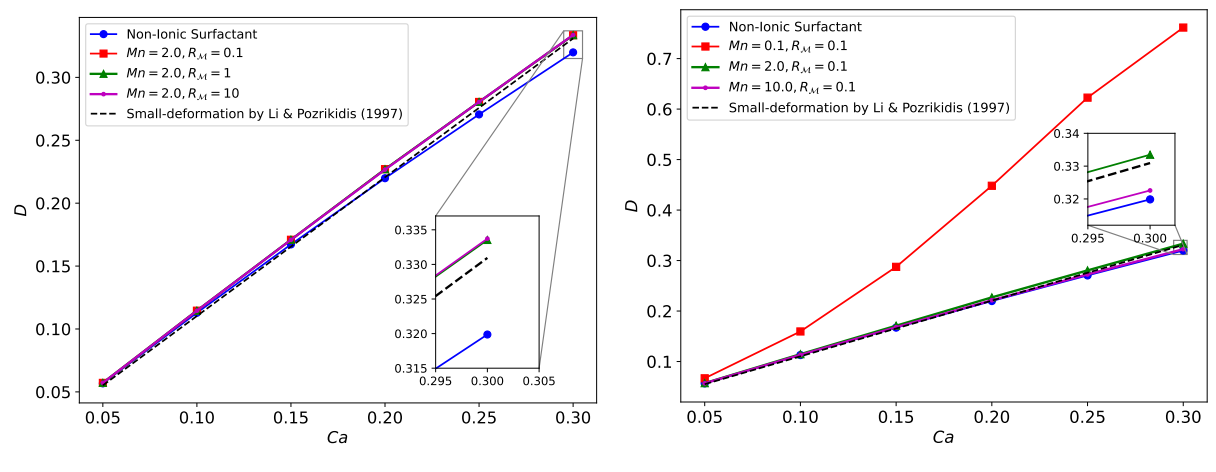
Future simulations in this work use smaller domains, such as 10×10 . In these cases, the electric potential decay will not follow a logarithmic behavior. The purpose of this comparison with larger domains was to verify whether concentrating the electric charge at the interface using a Dirac delta function, as expressed in Eq. (2.23), is equivalent to the classical problem with a fixed Neumann boundary condition at the surface in a circular geometry.

5.3 Ionic and non-ionic surfactant-covered droplet deformation

5.3.1 Comparison with small deformation theory

The electric problem introduces two new parameters, the Mason number and the Mobility ratio, which influence the droplet's deformation. A small deformation theory by Li and Pozrikidis (1997), given by Eq. (5.2) for non-ionic surfactant-covered droplets subjected to shear flow is used as a reference for the simulated cases in Fig. 17, considering Re = 0.01, λ = 1, E = 0.1, and X = 0.6. For all simulations in this section, a square domain of [10 × 10] was used, discretized by a regular 400 × 400 cell mesh.

$$D = \frac{5}{8} \frac{35 + 4\epsilon}{20 + 2\epsilon} \text{Ca}, \quad \epsilon = \frac{EX\alpha}{1 - EX}.$$
 (5.2)



- (a) For Ionic Surfactant, Mn is fixed.
- (b) For Ionic Surfactant, $R_{\mathcal{M}}$ is fixed.

Figure 17 – Taylor deformation as a function of the Capillary Number for Re = 0.01, $E=0.1,\,X=0.6,\,{\rm and}\,\,\alpha=\frac{{\rm Pe}}{{\rm Ca}}=10.$

In Fig. 17a, the present work agrees well with the analytical prediction up to $Ca \approx 0.15$, but deviations appear for larger Capillary numbers, as expected, since the theory is valid only for small deformations. However, for ionic surfactant-covered droplets, the numerical results match well across the entire range of analysis when the Mason number is fixed at 2.0 and the Mobility ratio takes values of 0.1, 1.0, and 10.

It is observed that the Mobility ratio does not significantly influence the Taylor deformation, as the magnitude of the deformation remains similar across small and large values of $R_{\mathcal{M}}$. On the other hand, when the Mobility ratio is fixed and the Mason number is varied, the Taylor deformation shows greater sensitivity for smaller Mason numbers. This behavior is evident in the red line (Mn = 0.1) in Fig. 17b, which begins to deviate significantly from the Non-Ionic case at $Ca \approx 0.1$.

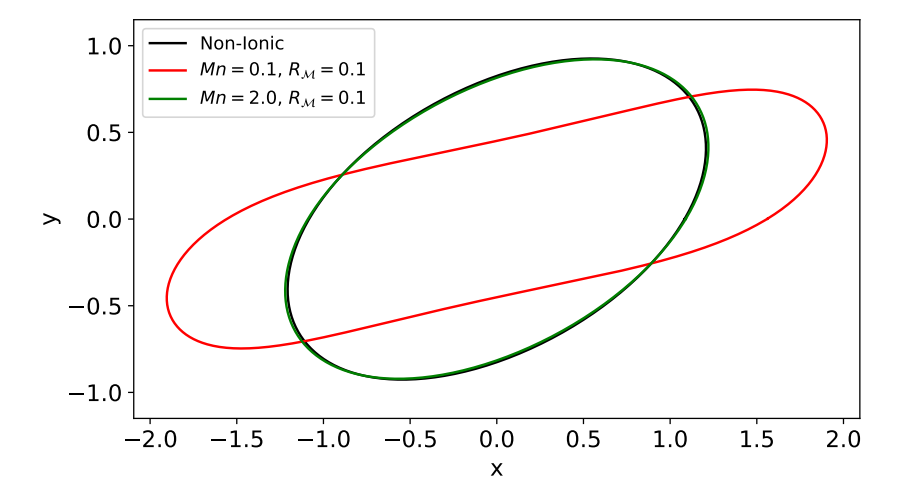


Figure 18 – Droplet shape comparison for Re=0.01, E=0.1, X=0.6, Pe=2.5, Ca=0.25.

The droplet shapes for three points extracted from Fig. 17b at Ca = 0.25 are shown in Fig. 18. For Mn $\sim \mathcal{O}(1)$, the deviation in droplet shape from the Non-Ionic droplet shape is very small, and for Mn $\gg 1$, it becomes negligible, as expected from

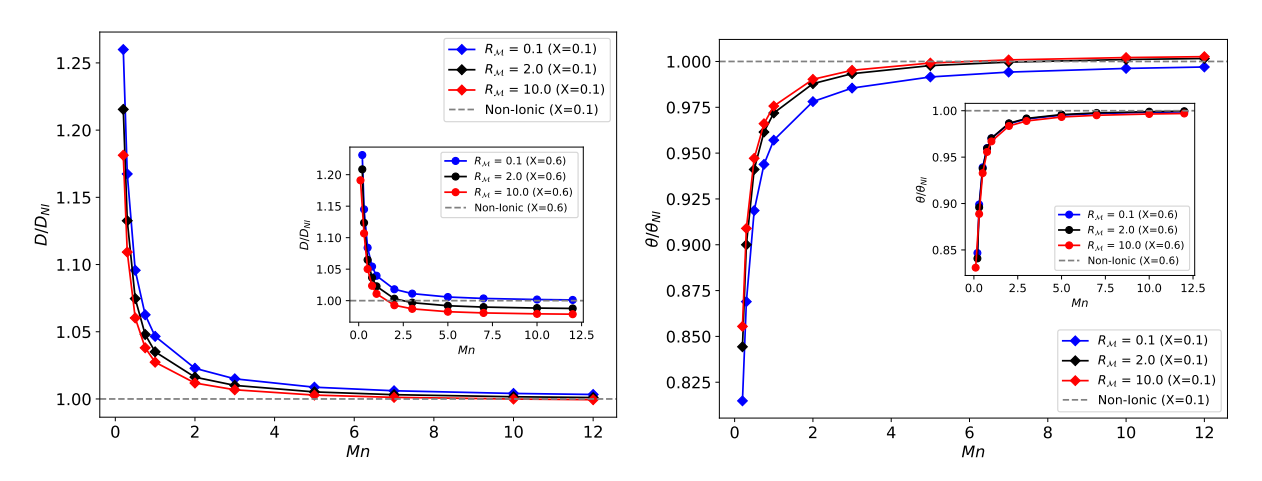
the deformation behavior in Fig. 17b. In contrast, for Mn \ll 1, the droplet undergoes significant deformation, adopting a peanut-like shape.

It can be said that the electromigration of surfactant along the droplet's surface, represented by $R_{\mathcal{M}}$, does not play a big role in droplet deformation and shape. Instead, the repulsive electric force, which becomes stronger for small Mn, is the primary agent responsible for changing the droplet morphology.

5.3.2 More detailed analysis of Mason number and Mobility ratio

To analyze the isolated effects of the Mason number and Mobility ratio, Fig. 19 presents both Taylor deformation and inclination as functions of the Mason number for different Mobility ratio values (0.1, 2, and 10) and Coverage (0.1 in the main plot and 0.6 in the inset plot). For these simulations, most parameters remain unchanged, except for Ca = 0.1 and E = 0.2. A non-square domain of $[15 \times 6]$ was used, discretized with a 400×160 regular cell mesh.

A horizontal dashed line represents the Non-Ionic case, which corresponds to the limiting case $Mn \to \infty$ and $R_{\mathcal{M}} \to 0$ of the Ionic case, as shown in the blue line of both Figs. 19a and 19b. Both deformation and inclination are normalized by their respective values from the Non-Ionic case, which are represented by the subscript NI.



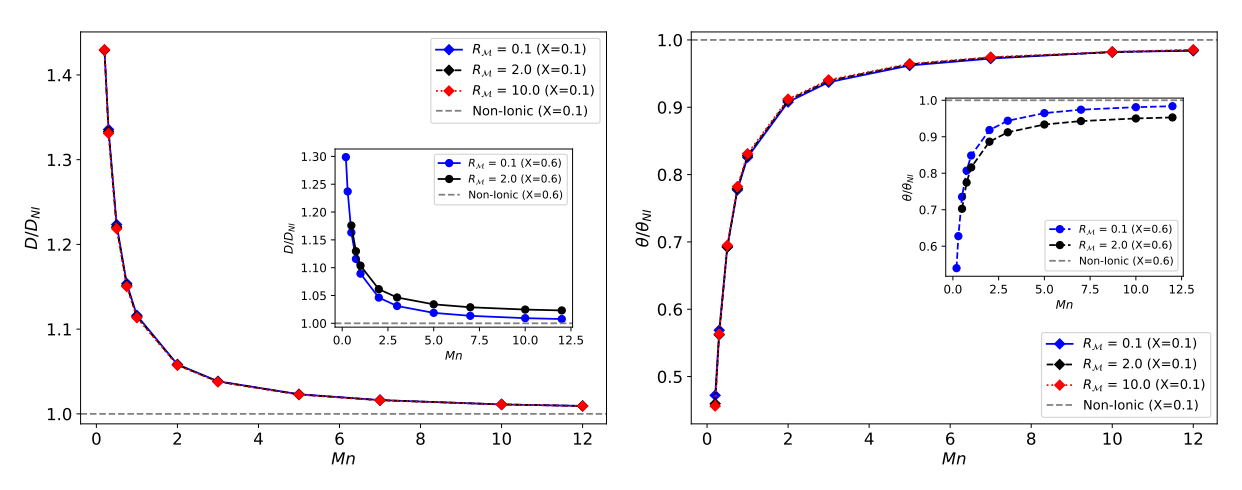
(a) Taylor deformation as a function of the Ma- (b) Inclination as a function of the Mason numson number. ber.

Figure 19 – Simulations for Re = 0.01, Ca = 0.1, Pe = 10, and E = 0.2. The steady-state Taylor deformation and inclination for the Non-Ionic case are $D_{NI} = 0.12$ and $\theta_{NI} = 37.8^{\circ}$ for X = 0.1, and $D_{NI} = 0.149$ and $\theta_{NI} = 35.8^{\circ}$ for X = 0.6.

For Mn < 1, the Taylor deformation reaches higher values and varies significantly with changes in the Mason number (the derivative dD/dMn diverges as Mn \rightarrow 0). In contrast, for larger Mason numbers (Mn > 6), the deformation remains nearly constant, approaching the Non-Ionic deformation values of 0.12 for X=0.1 and 0.149 for X=0.6. The inclination exhibits a similar trend, decreasing more noticeably for small Mason numbers and stabilizing at a plateau near the Non-Ionic steady inclination of 37.8° for

X = 0.1 and 35.8° for X = 0.6. As the Mobility ratio increases, the deformation curve shifts downward, while the inclination curve shifts upward.

Despite the described behavior in deformation and inclination, the magnitude of the changes is not very large: up to 25% more deformed and 20% less inclined compared to the Non-Ionic case for Mn = 0.2. Therefore, the same analysis were replicated using Ca = 0.5, which allows the droplet to deform more. For this configuration, the Non-Ionic deformation is 0.58 for X = 0.1 and 0.66 for X = 0.6, where the largest deviation is more than 40%, occurring at Mn = 0.2 as visualized in Fig. 20a.



(a) Taylor deformation as a function of the Ma- (b) Inclination as a function of the Mason numson number. ber.

Figure 20 – Simulations for Re = 0.01, Ca = 0.5, Pe = 10, and E = 0.2. The steady-state Taylor deformation and inclination for the Non-Ionic case are $D_{NI} = 0.58$ and $\theta_{NI} = 15.5^{\circ}$ for X = 0.1, and $D_{NI} = 0.66$ and $\theta_{NI} = 13.3^{\circ}$ for X = 0.6.

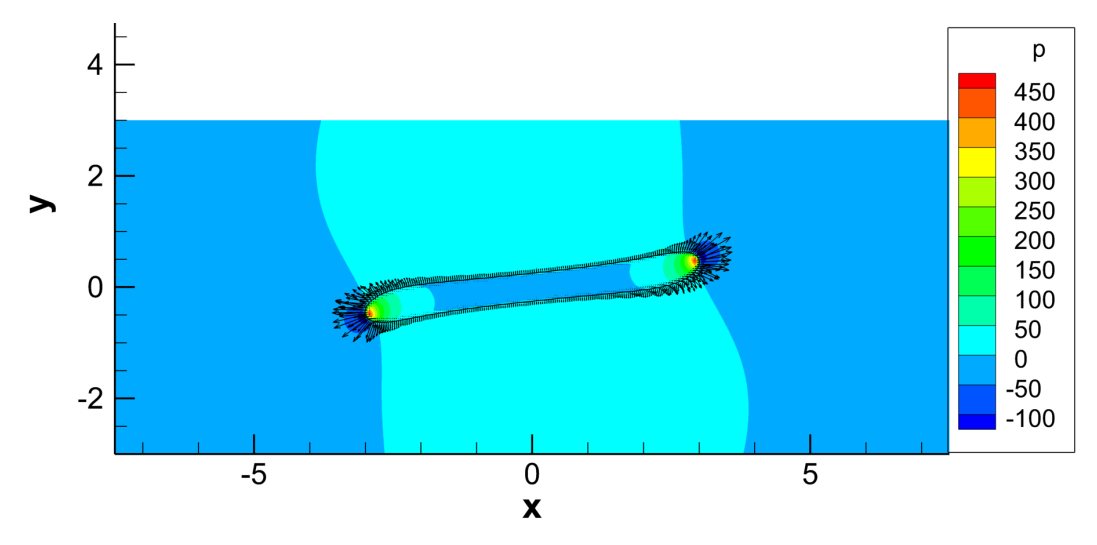


Figure 21 – Pressure contour and electric force vector field in steady-state for Re = 0.01, Ca = 0.5, Pe = 10, X = 0.1, E = 0.2, Mn = 0.2 and $R_{\mathcal{M}} = 0.1$.

The inclination decreases significantly for Ca = 0.5 compared to Ca = 0.1 for the Non-Ionic case and reaches a value of 15.5° for X = 0.1 and 13.3° for X = 0.6. For the Ionic case, the droplet inclination reduces up to more than 50% at Mn = 0.2 compared

to the Non-Ionic case. It means that the imposed shear flow doesn't have enough time to rotate the droplet due to the intense repulsive electric force repelling the extremities of the droplet as seen by the vector field in Fig. 21.

In Fig. 20a, both the deformation and inclination curves for X=0.1 almost overlap for all values of $R_{\mathcal{M}}$, whereas for X=0.6, the deformation curve shifts upwards and the inclination curve shifts downwards with the increase of the Mobility ratio. The simulations for X=0.6 and $R_{\mathcal{M}}=10$ could not be performed due to numerical instabilities.

5.4 Scalar field contours

The droplet's contour for the pressure field and streamlines are illustrated in Fig. 22, comparing the extreme cases from Figs. 19 and 20, evaluated at Mn = 0.2 and $R_{\mathcal{M}} = 0.1$. At Ca = 0.1, the droplet maintains a relatively compact and rounded shape, with minor elongation in the direction of shear flow. The pressure distribution in this case is concentrated, with the highest pressure (orange and red regions) appearing in a localized area near the droplet's tips and core. The streamlines remain nearly symmetric, with moderate perturbations around the droplet but no significant flow distortions. Additionally, the recirculation zones are observed to be confined within the droplet as well as outside the droplet, predominantly around the y = 0 axis.

In contrast, at Ca = 0.5, the droplet experiences greater elongation compared to the case at Ca = 0.1, as the viscous forces become more significant. The high-pressure regions, which were previously concentrated in a single localized zone, now appear at two distinct points near the ends of the stretched droplet. This shift in pressure distribution suggests an increased internal stress as the droplet stretches along the flow direction. The recirculation zones also become more elongated, extending along the droplet's stretched profile.

The same analysis can be applied to the surfactant distribution along the droplet's surface, as visualized in Fig. 23. At Ca = 0.1, the surfactant concentrates approximately 50% more at a small band near the tips compared to the initial condition, while the rest of the surface maintains a concentration of around 80% of the initial condition. In contrast, at Ca = 0.5, the surfactant concentration at the droplet's tips becomes more localized, showing only a 10% increase compared to the initial condition. Meanwhile, the rest of the surface experiences a significant reduction, with surfactant concentration dropping to as low as 70% less than the initial condition. This decrease in surfactant concentration is attributed to the expansion of the surface area due to droplet elongation and the additional area created by surfactant transport.

For the electric field intensity, visualized in Fig. 24, it is seen what was expected from the surfactant concentration. As the surfactant concentrates at the tips of the droplets in both cases for Ca = 0.1 and Ca = 0.5, the electric charges carried by the

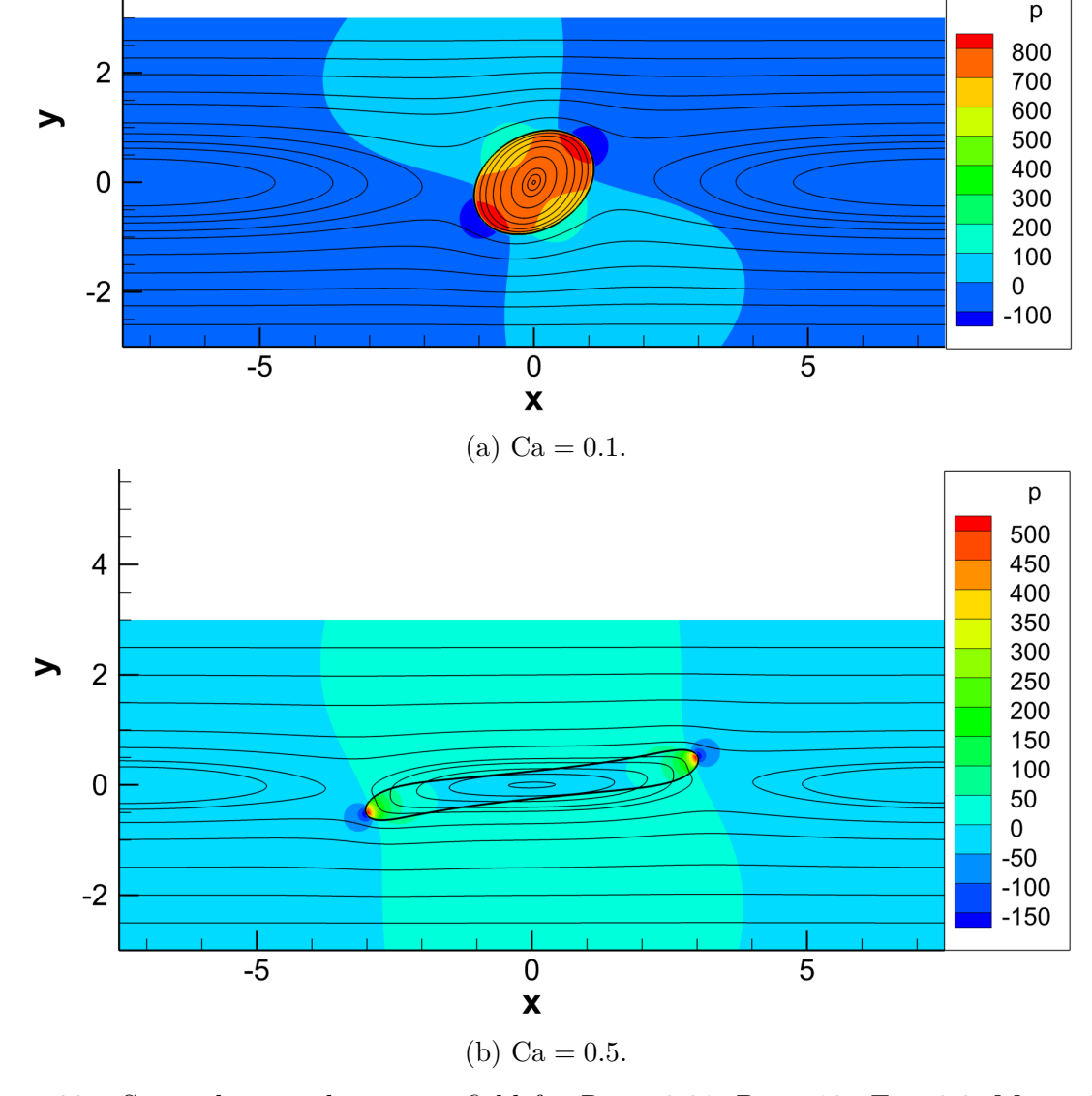
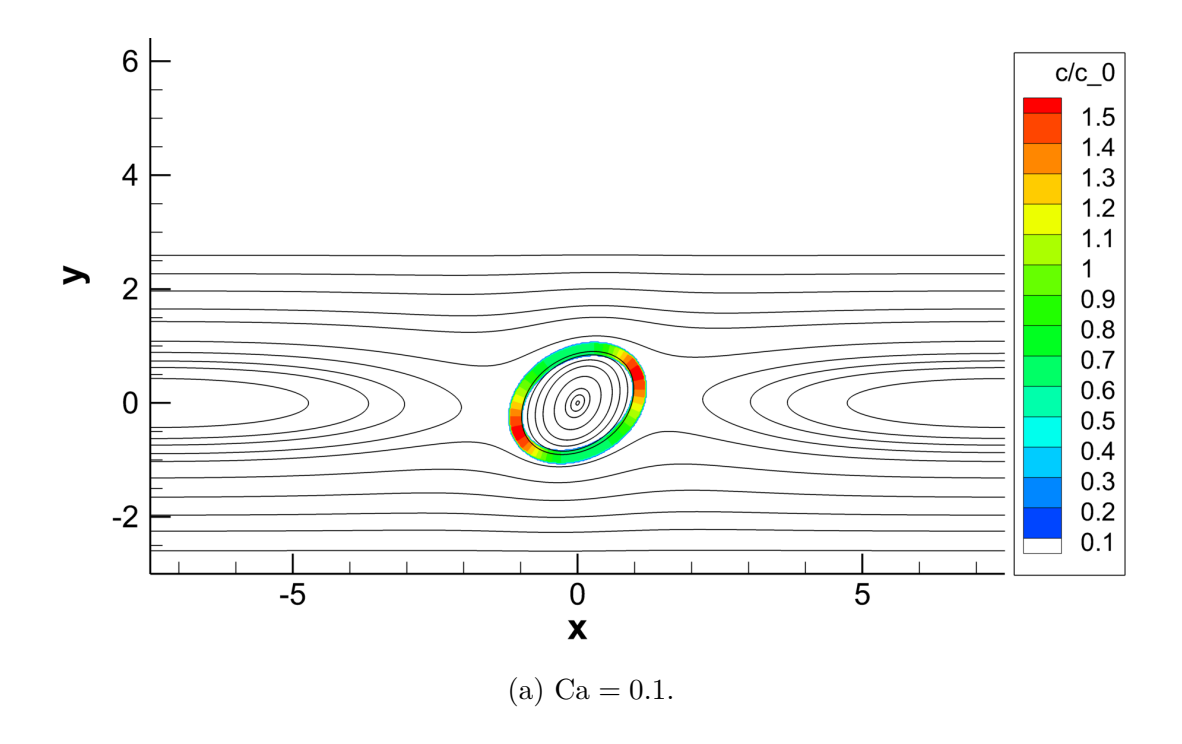


Figure 22 – Streamlines and pressure field for Re = 0.01, Pe = 10, E = 0.2, Mn = 0.2, and $R_{\mathcal{M}} = 0.1$.

charged surfactants at these places create a intense electric field (red zone), and it dissipates as it moves away from the tips, to outside the domain or to other less surfactant-concentrated regions on the surface. The electric field contours far away from the droplet are more vertically straight for Ca = 0.1, whereas the contours suffers more perturbation for Ca = 0.5 due to the more stretched droplet and more concentrated charges at the tips.

A simplified analytical expression for droplet elongation was derived, assuming that all charges are concentrated at two point charges at the tips, each with an intensity of Q/2, where $Q=q_sA_s$. By balancing the capillary force, the Coulomb force, and the pressure jump at the interface, it follows that $L/B \sim 1/\mathrm{Mn}$, where L and B are the semi-major and semi-minor axes of the droplet, respectively (detailed derivation in Appendix D). Figure 25 shows a linear behavior of the ratio L/B with $1/\mathrm{Mn}$. The simulations were performed for large Mason numbers and a small capillary number (Ca = 0.1), corresponding to small deformations and negligible viscous forces, which is a limiting case of the explicitly obtained analytical expression. Despite this, a noticeable difference is



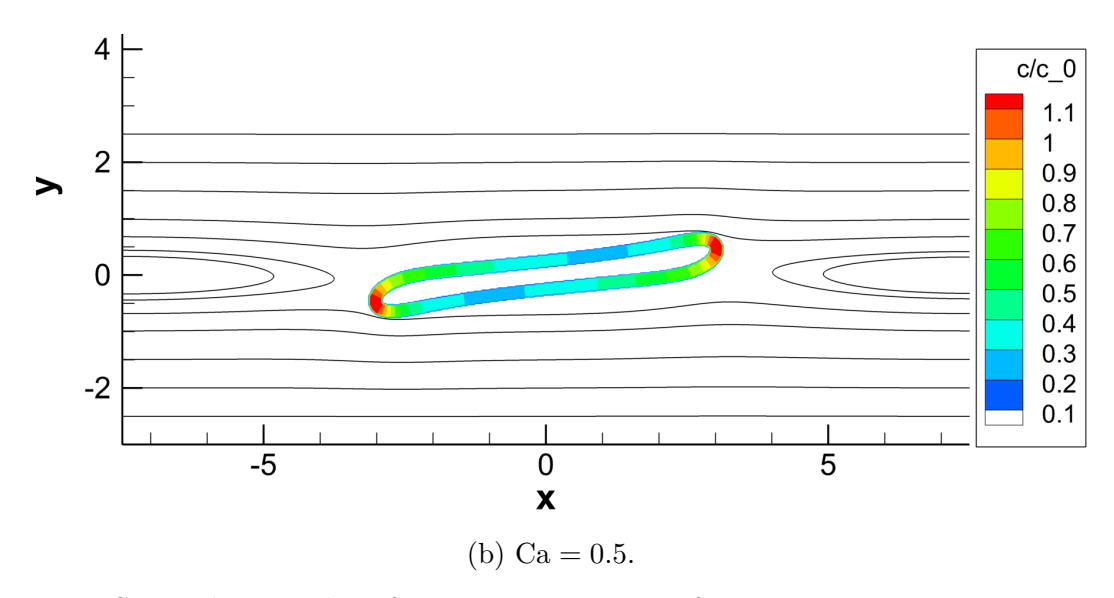
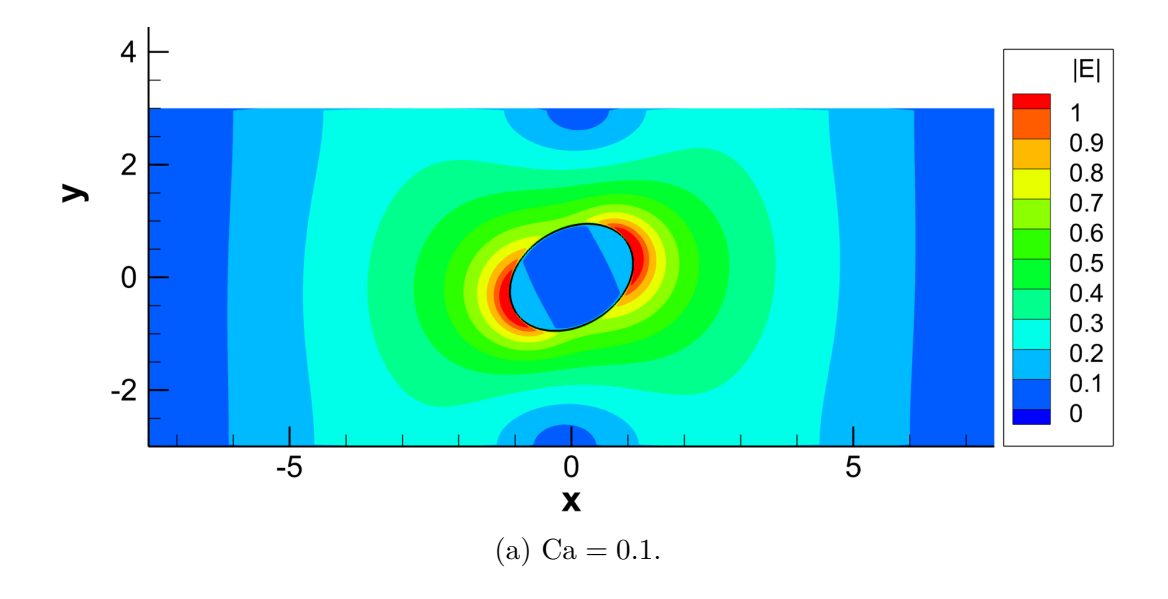


Figure 23 – Streamlines and surfactant concentration for Re = 0.01, Pe = 10, E = 0.2, Mn = 0.2, and $R_{\mathcal{M}} = 0.1$.

observed between the simulated data and the analytical results. This discrepancy arises from the simplifications in the analytical model, which assumes point charges and a ellipsoidal droplet shape. These assumptions deviate significantly from the actual behavior visualized in Fig. 23a, where charges are distributed across the entire droplet interface, with more significant concentration peaks at the tips. Nevertheless, the slope of the fitted line for the simulated data is 0.145, which is close to the value of 1/8 = 0.125 predicted by the analytical expression.



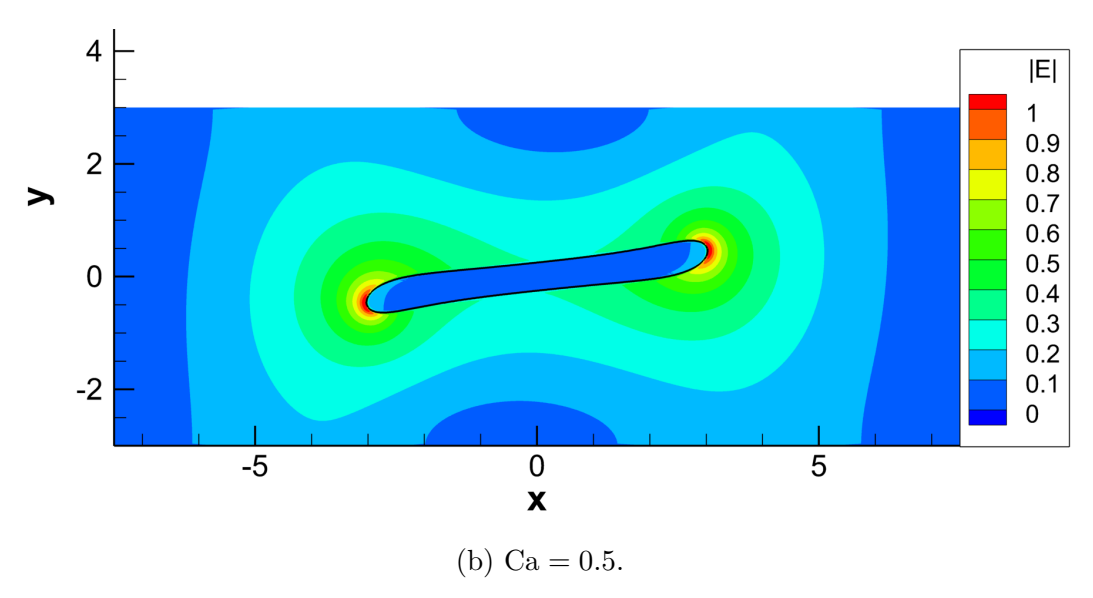


Figure 24 – Electric field magnitude for Re = 0.01, Pe = 10, E = 0.2, Mn = 0.2, and $R_{\mathcal{M}} = 0.1$.

5.5 Ionic and non-ionic surfactant concentration

The surfactant concentration along the droplet's surface governs its behavior, including deformation, inclination, and morphology. For the ionic case, the surfactant concentration is directly proportional to the electric charge, meaning that mapping the surfactant distribution is equivalent to mapping the electric charge distribution, apart from a scaling factor. Figure 26 shows the surfactant distribution, c/c_0 , as a function of the normalized arc length, s/L, along the droplet's surface. The parameter c_0 corresponds to the uniform and initial surfactant distribution, and L corresponds to the droplet's perimeter. In Fig. 26a, the surfactant distribution is presented for a fixed Mason number (Mn = 5) and different Mobility ratios, $R_{\mathcal{M}} = \{0.1, 1, 10\}$. Conversely, Fig. 26b shows the surfactant distribution for a fixed Mobility ratio ($R_{\mathcal{M}} = 1$) and three Mason number values, $M_{\mathcal{M}} = \{0.5, 5, 50\}$.

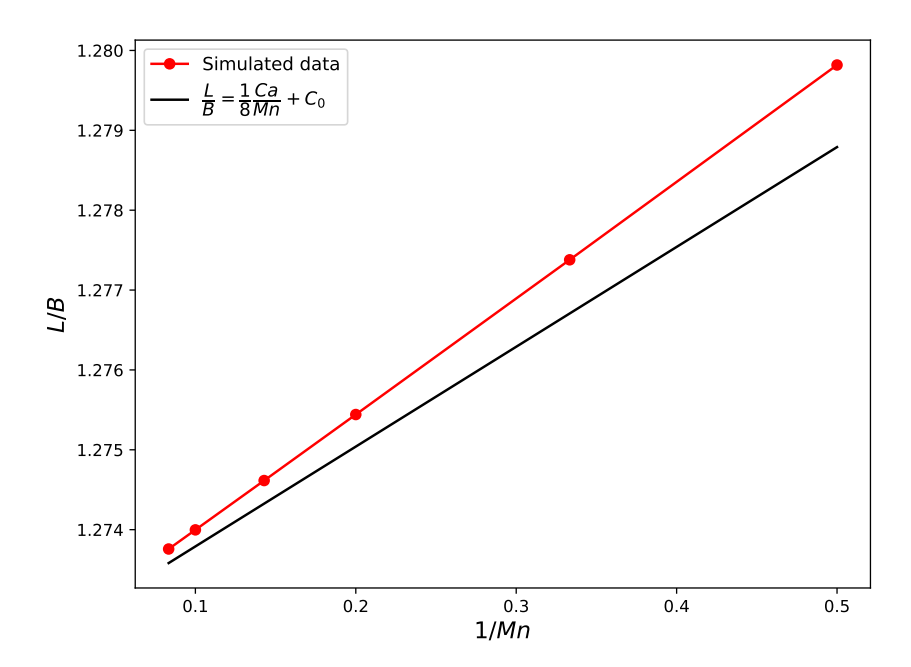


Figure 25 – Droplet elongation, represented by the aspect ratio L/B, as a function of 1/Mn for Re = 0.01, Ca = 0.1, Pe = 10, E = 0.2, and $R_{\mathcal{M}} = 0.1$. The parameter C_0 in the analytical expression accounts for the pressure jump across the interface.

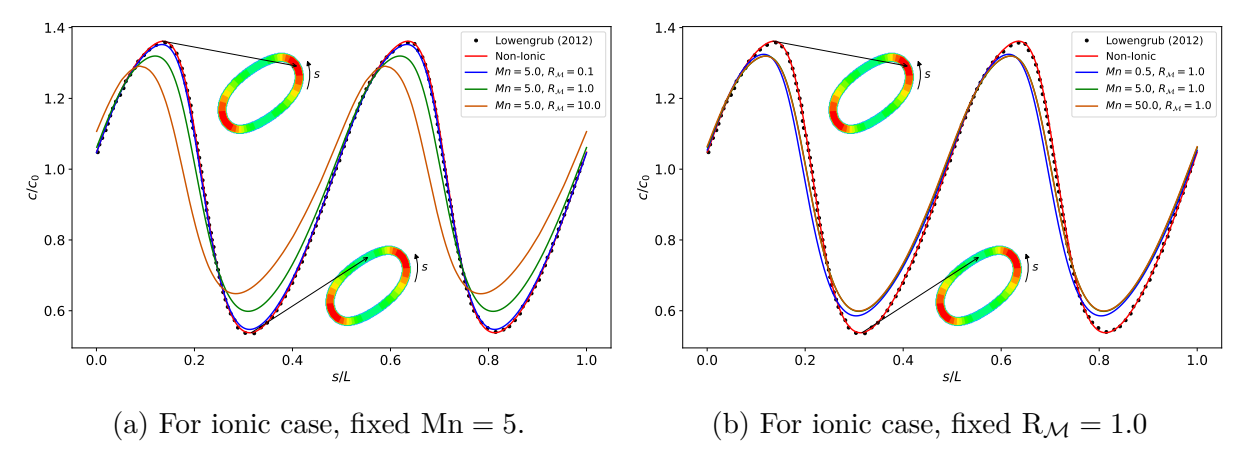


Figure 26 – Surfactant concentration as a function of the normalized arc length for Re = 10, Ca = 0.1, Pe = 10, X = 0.6, and E = 0.2, captured at t = 9. The insets show the surfactant concentration contours on the droplet surface, pointing out regions with higher and lower surfactant concentrations.

The work of Xu, Yang and Lowengrub (2012a) on non-ionic surfactant-covered droplets is represented by black dots and aligns closely with the present results, shown as a red line. The parameters used are identical to those in Xu, Yang and Lowengrub (2012a): Re = 10, Ca = 0.1, λ = 1, Pe = 10, X = 0.6, and E = 0.2. Notably, they initialized the flow with a linear velocity profile across the entire [10 × 4] domain, rather than relying solely on the movement of the top and bottom plates. This initialization was replicated to ensure consistency with their results at the dimensionless time t = 9.

It can be noticed that the increase of $R_{\mathcal{M}}$ reduces the point of maximum surfactant concentration and raises the minimum surfactant concentration, also shifting these points

to the left as seen in Fig. 26a. On the other hand, the increase of Mn (Fig. 26b) does not affect the surfactant distribution much, with only a small, though not very significant, change observed at the lower values of surfactant concentration for Mn = 50.

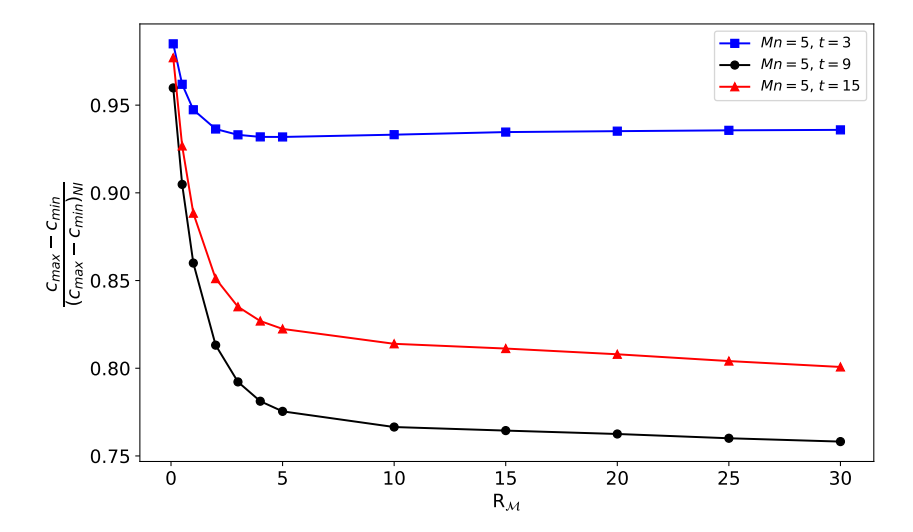
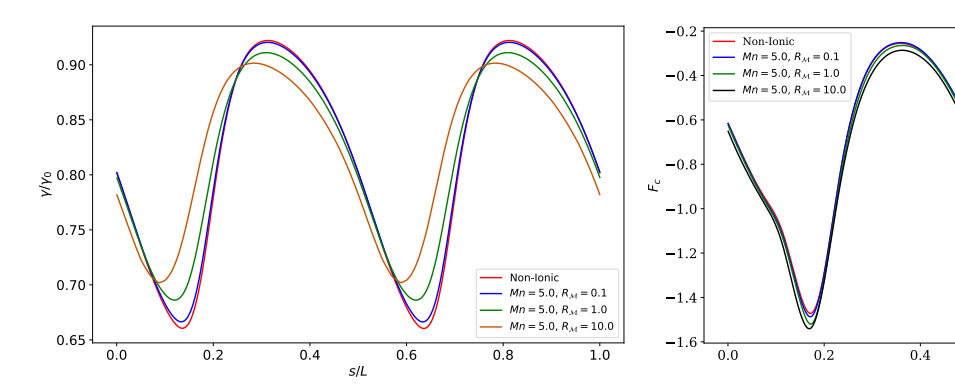


Figure 27 – Peak-to-peak amplitude of the surfactant concentration as a function of the Mobility ratio for Re = 10, Ca = 0.1, Pe = 10, X = 0.6, E = 0.2, and Mn = 5 for different instant times.

As the difference between the maximum peak and minimum peak of surfactant concentration decreases with increasing $R_{\mathcal{M}}$, Fig. 27 illustrates this trend across a wide range of Mobility ratios. The results suggest that the peak-to-peak surfactant concentration stabilizes at approximately 80% of the peak-to-peak concentration of the Non-Ionic case, denoted as $(c_{\text{max}} - c_{\text{min}})_{\text{NI}}$, for high $R_{\mathcal{M}}$ values. Figure 27 also shows the variation of the peak-to-peak amplitude at three distinct instants during the simulation: at the beginning (t=3), at an intermediate time (t=9), and at steady-state (t=15). The behavior is non-monotonic, as the amplitude at t=3 is higher than at t=15, while the amplitude at t=9 is lower than at both t=3 and t=15. This indicates that the system undergoes fluctuations in amplitude before reaching a steady state, rather than following a simple increasing or decreasing trend.

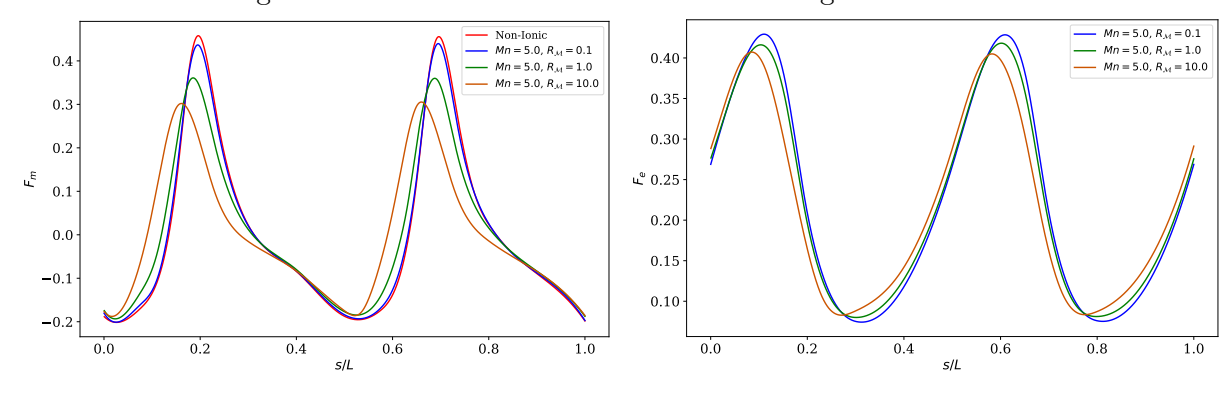
The surfactant distribution impacts all interfacial quantities such as interfacial tension and interfacial forces. Figure 28 is an extension of the results presented in Fig. 26a, and presents these quantities along the arc length of the droplet's interface. The interfacial tension, in Fig. 28a, exibits a opposite behavior compared to the surfactant concentration in Fig. 26a, in which the higher peaks in interfacial tension occur at the lower peaks in the surfactant concentration, and viceversa. The increase in $R_{\mathcal{M}}$ also shifts the interfacial tension's curves to the left as expected by the behavior in surfactant concentration. Increasing $R_{\mathcal{M}}$ reduces the amplitude of the high peaks and raises the amplitude of the low peaks.

The capillary force (F_c) , which represents the normal component of the interfacial tension effect (Fig. 28b), exhibits a behavior closely linked to the surfactant distribution: higher surfactant concentration leads to a stronger capillary force. This force is always



(a) Interfacial tension as a function of the nor- (b) Capillary force as a function of the normal-malized arc length.

1.0



(c) Marangoni force as a function of the nor- (d) Electric force as a function of the normal-malized arc length.

Figure 28 – Interfacial tension and forces for Re = 10, Ca = 0.1, Pe = 10, X = 0.6, E = 0.2, and Mn = 5.0 captured at t = 9.

negative, acting as a restoring mechanism that opposes deformation. While the role of $R_{\mathcal{M}}$ is not particularly significant, its increase slightly amplifies the capillary force at the peaks.

The Marangoni force (F_m) , the tangential component of the interfacial tension effect, is strongest where surface tension gradients are most pronounced. A comparison between Figs. 28a and 28c reveals that regions with steep surface tension gradients—such as at $s/L \approx 0.2$ —experience higher Marangoni effects. Conversely, at surface tension peaks, where the derivative is zero, the Marangoni force vanishes. Increasing $R_{\mathcal{M}}$ shifts the force distribution slightly to the left while reducing its peak values.

The electric force (F_e) at the interface (Fig. 28d) closely follows the surfactant concentration curve, as expected from the relationship $F_e \sim c$. However, a key distinction arises: while F_e exhibits high peaks in regions of high surfactant concentration, it drops significantly at lower concentration peaks despite the significant presence of surfactant. This behavior is caused by the weaker electric field away from the droplet tips, evidencing the dependence of F_e on the local electric field strength ($F_e \sim E$).

To maintain consistency with the results from the previous section, the Reynolds number is set to 0.01, which is appropriate for creeping flow, and the fluid starts from rest throughout the domain. The surfactant distribution for this configuration is presented in Fig. 29. A key difference from the previous analysis in Fig. 26a is that the highest surfactant concentration for $R_{\mathcal{M}} = 10$ (black curve) now lies above the curve for $R_{\mathcal{M}} = 1$.

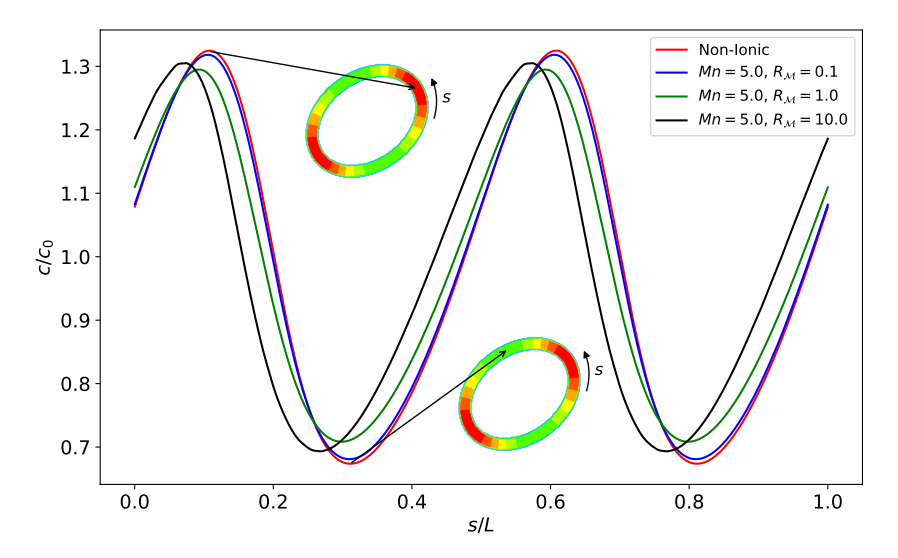


Figure 29 – Surfactant concentration as a function of the normalized arc length for Re = 0.01, Ca = 0.1, Pe = 10, X = 0.6, and E = 0.2 at steady-state.

The peak-to-peak amplitude of the surfactant concentration, shown in Fig. 30, reveals a non-monotonic behavior: it decreases for $R_{\mathcal{M}} < 1$, reaches its minimum at $R_{\mathcal{M}} = 1$, and increases for $R_{\mathcal{M}} > 1$, eventually stabilizing close to the peak-to-peak amplitude of the non-ionic case for high Mobility ratios. The transient behavior is also non-monotonic, with the surfactant concentration at the beginning (t = 0.75) being higher than the non-ionic case for high $R_{\mathcal{M}}$. As the simulation progresses, the peak-to-peak amplitude decreases to a range of 90% to 100% of the non-ionic case.

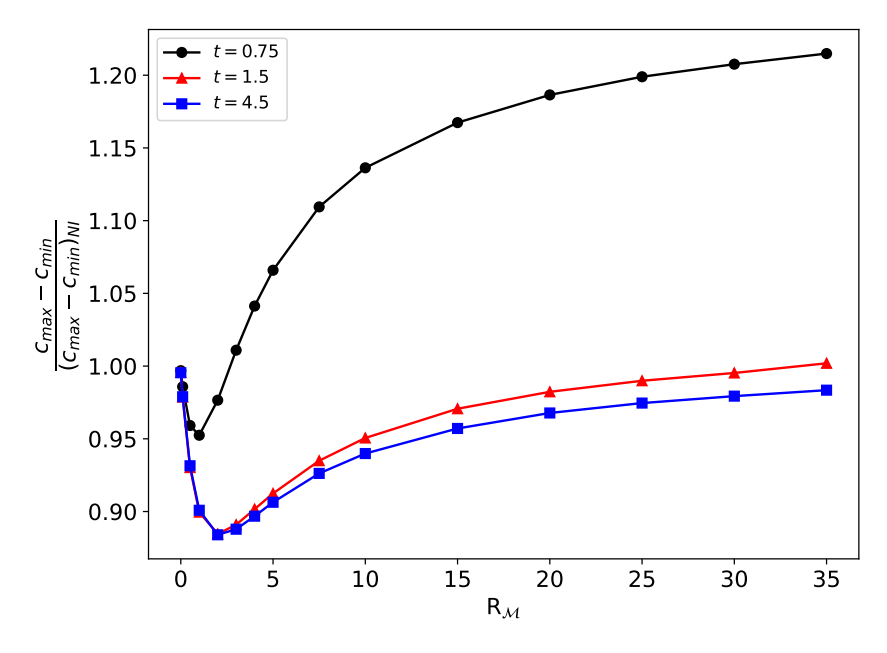


Figure 30 – Peak-to-peak amplitude of the surfactant concentration as a function of the Mobility ratio for Re = 0.01, Ca = 0.1, Pe = 10, X = 0.6, E = 0.2, and Mn = 5 for different instant times.

Furthermore, the surfactant distribution curve continues to shift to the left, as better visualized in Fig. 31. Here, the arc-length position of the first peak in surfactant concentration, denoted by s^* , is captured and normalized by the position of the first peak in the non-ionic case, s_{NI}^* . The value of s_{NI}^* is approximately 0.12L, as observed in Fig. 29 (red curve). It can be observed that for $R_{\mathcal{M}} < 7$, the position of the first peak is highly sensitive to increases in $R_{\mathcal{M}}$, whereas for $R_{\mathcal{M}} > 10$, it stabilizes. The transient behavior reveals that the peak surfactant concentration initially starts around 60% of the non-ionic peak position and shifts to approximately 70% for high Mobility ratios.

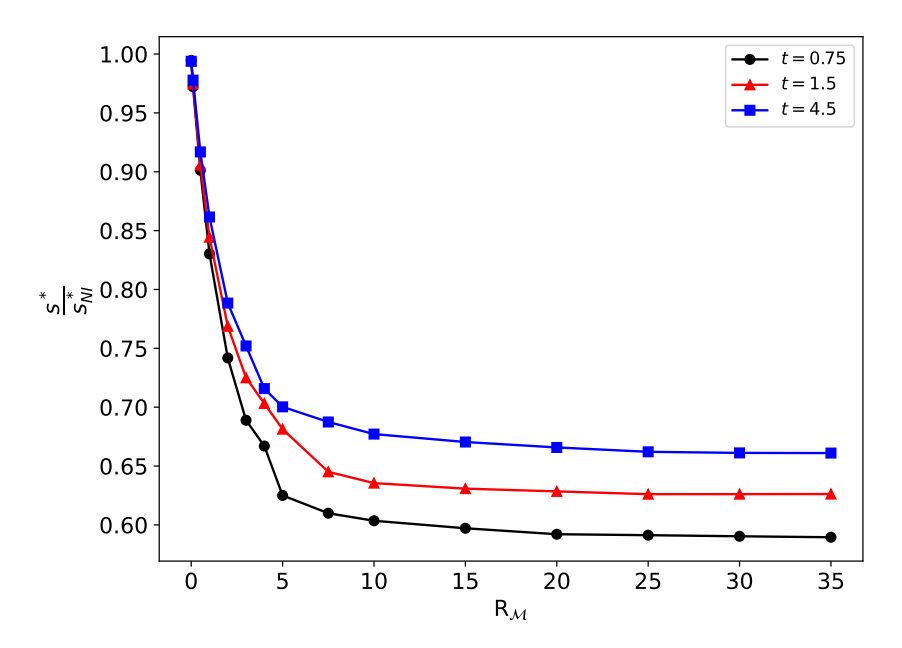
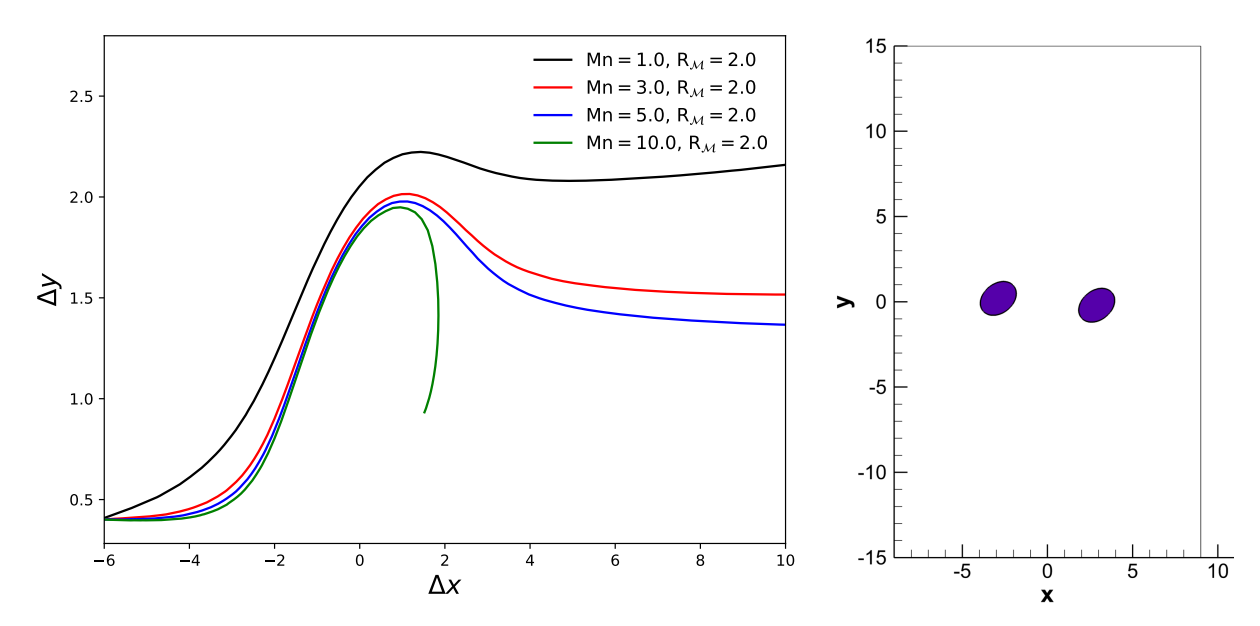


Figure 31 – Position of the first peak in surfactant concentration as a function of the Mobility ratio for Re = 0.01, Ca = 0.1, Pe = 10, X = 0.6, E = 0.2, and Mn = 5 for different instant times.

5.6 Pairwise droplet interaction

Figure 32a illustrates the trajectories of two droplets initially positioned at (-3, 0.2) and (3, -0.2) in a simple shear flow, with $\Delta x = -6$ and $\Delta y = 0.4$ representing their initial horizontal and vertical separations as shown in Fig. 32b. The trajectories are computed for varying Mason numbers (Mn = $\{1.0, 3.0, 5.0, 10.0\}$) under fixed parameters Re = 0.01, Ca = 0.2, λ = 1, X = 0.1, E = 0.2, Pe = 10.0, and R_M = 2.0. The domain size and mesh resolution (18 × 30 discretized into 480 × 800 cells) ensure numerical stability while balancing computational cost.

At low Mn (e.g., Mn = 1.0, black curve), electric forces dominate over viscous effects, inducing significant lateral migration. The droplets exhibit a pronounced rise in Δy , reaching a peak value of ~ 2.3 before equilibrating as shear flow advects them apart. As Mn increases, viscous forces progressively suppress electric interactions, reducing the peak Δy for $\Delta y \sim 2.0$ at Mn = 3.0 (red curve) and $\Delta y \sim 1.9$ at Mn = 5.0 (red curve). For



(a) Trajectories of droplet pairs in simple shear flow for vary- (b) 18×30 domain with two ing Mason numbers. Δx and Δy denote the relative cendroplets positioned at troid separations. (-3,0.2) and (3,-0.2).

Figure 32 – Behavior of droplet pairs in simple shear flow for Re = 0.01, Ca = 0.2, λ = 1, X = 0.1, E = 0.2, Pe = 10.0, and $R_{\mathcal{M}} = 2.0$.

Mn = 10.0 (green curve), the trajectory terminates abruptly due to coalescence, as the uniform mesh cannot resolve lubrication forces in the thin interfacial gap. A finer adaptive mesh would prevent coalescence but entails prohibitive computational cost. The final Δy values correlate with migration rates, which can inform diffusion coefficient calculations in emulsion models (suggests future works).

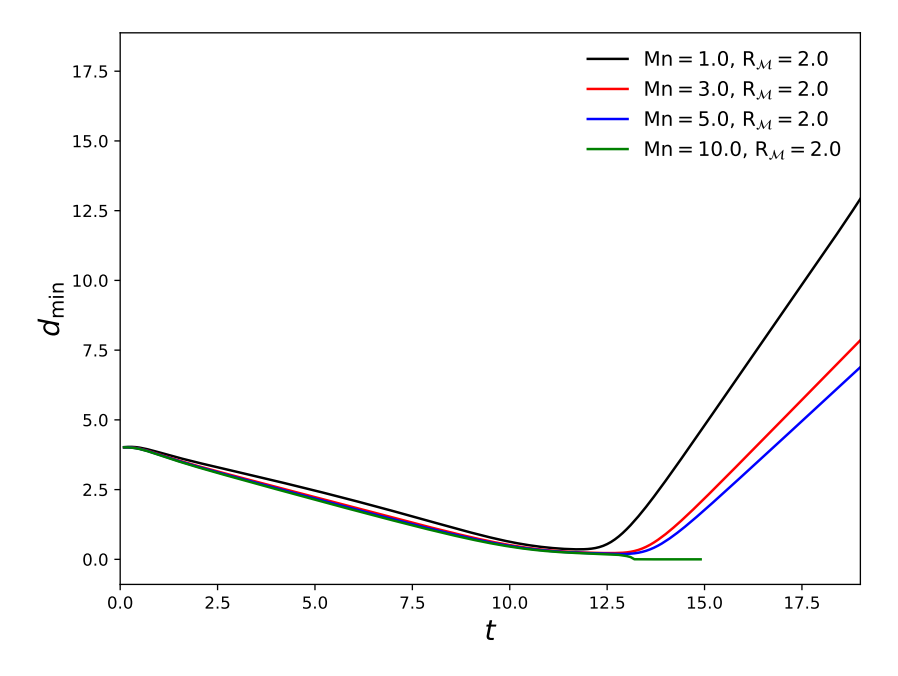


Figure 33 – Minimum interface-to-interface distance (d_{\min}) between droplets over time. Coalescence occurs at Mn = 10.0 (green curve), where $d_{\min} \to 0$.

Figure 33 complements the trajectory analysis by quantifying the closest ap-

proach between droplets. At Mn = 1.0 (black curve), strong electric repulsion maintains $d_{\rm min} > 0.35$, followed by rapid separation. Intermediate Mn values (blue/red curves) show prolonged interaction periods with smaller $d_{\rm min}$, reflecting weaker repulsion. For Mn = 10.0 (green curve), viscous forces overwhelm repulsion, causing $d_{\rm min}$ to collapse to zero (coalescence) at $t \approx 12.5$. This behavior aligns with the truncated trajectory in Fig. 32a, indicating that the simulation fails to accurately capture the thin gap between droplets at high Mn due to insufficient mesh resolution and the overwhelming influence of viscous forces.

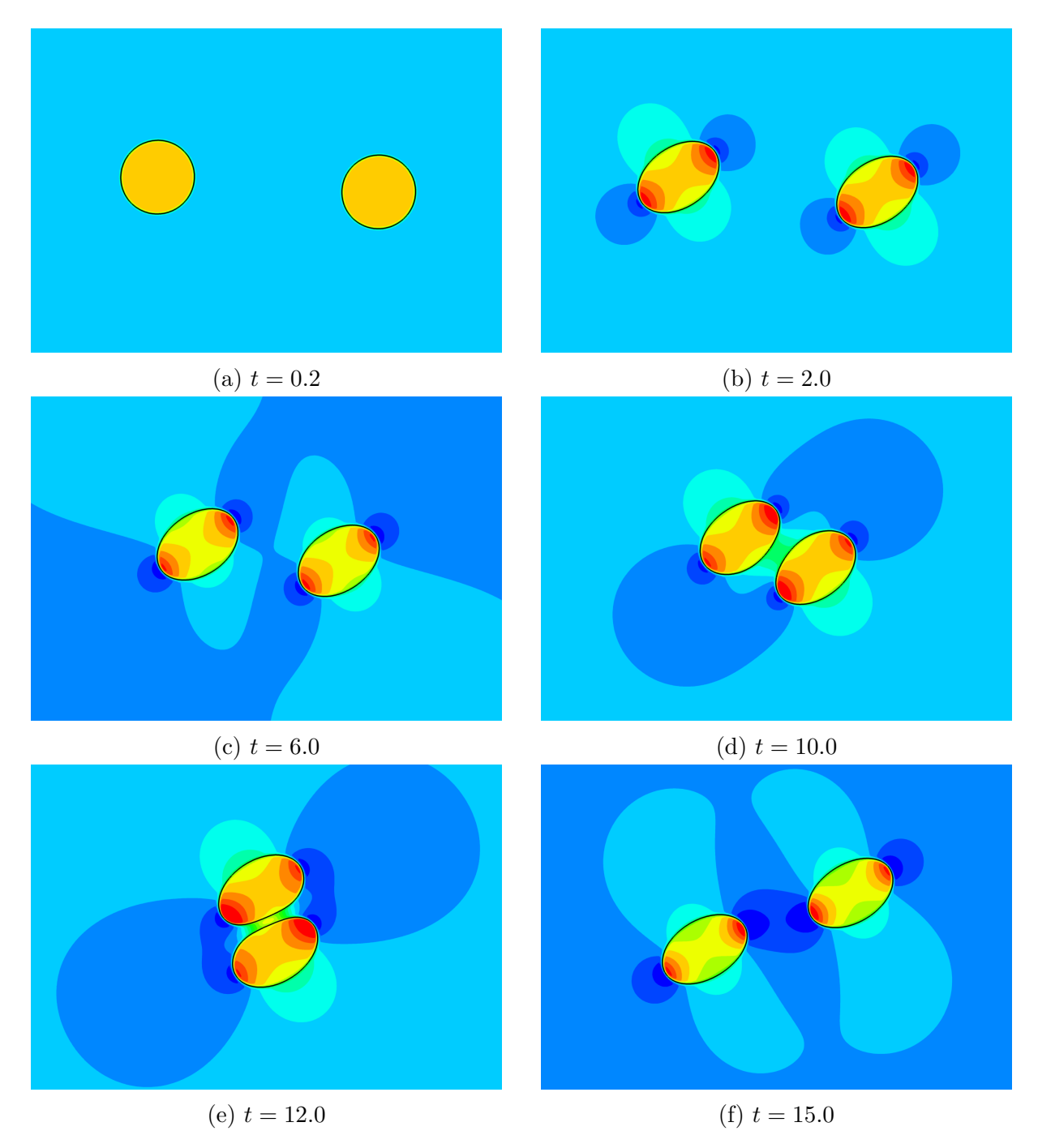


Figure 34 – Pressure contour and evolution of droplet pairs in simple shear flow at different timestamps Re = 0.01, Ca = 0.2, λ = 1, X = 0.1, E = 0.2, Pe = 10.0, Mn = 5.0, and R_M = 2.0.

Figure 34 illustrates the pressure contours and the evolution of a pair of droplets for the case where Mn = 5.0.

At t = 0.2, the droplets are nearly spherical and close to their initial positions at (-3, 0.2) and (3, -0.2). The pressure contours are symmetric, reflecting the initial balance of forces. The droplets have not yet experienced significant deformation or interaction. Between t = 2.0 and t = 6.0, the droplets begin to deform and move closer together under the influence of shear flow and the interplay of electric and viscous forces.

At t=10.0, the droplets continue to approach each other, and the pressure field in the gap starts to intensify more significantly. The symmetry of the pressure distribution is preserved, with the most intense pressure localized in the thin gap between the droplets. By t=12.0, the droplets achieve their maximum approximation, corresponding to the minimum gap distance (as seen Fig. 33 during 12 < t < 13). The pressure contours show a highly localized and intense pressure field in the gap, with the symmetry of the pressure distribution still maintained. The droplets exhibit significant deformation, with the interface near the gap developing a negative curvature due to the strong localized electrostatic repulsion.

At t = 15.0, the droplets begin to separate as the shear flow advects them apart. The pressure field starts to relax, and the droplets gradually regain a more ellipsoidal shape, reflecting the reduction in electrostatic and hydrodynamic interactions.

At Mn = 5.0, the balance between electric and viscous forces leads to moderate droplet deformation and interaction, but the electrostatic repulsion is strong enough to prevent coalescence. The pressure field plays a critical role in mediating the interaction between the droplets. The intensification of pressure in the thin gap at t = 10.0 and t = 12.0 demonstrates the importance of hydrodynamic forces in determining droplet behavior, while the symmetry of the pressure contours reflects the balanced nature of the interaction.

6 Results for Electrohydrodynamics of Droplets

This chapter begins with the validation of the two interface models described in the methodology: the Sharp Interface Model and the Smoothed Interface Model. Validation is conducted by comparing the Taylor steady deformation of the droplet with results of Cui, Wang and Liu (2019), which use the leaky dielectric theory, and the small-deformation theory developed by Feng (2002). Following the validation, the effect of surface charge convection is examined by varying the electric Reynolds number. Finally, by further increasing the effect of surface charge convection and the electric field intensity, the system can reach the Quincke regime (electrorotation), which will also be investigated.

6.1 Validation of the method using Smoothed and Sharp interface models

Figure 35 compares the Taylor deformation as a function of the electric Capillary number for different conductivity ratios (R = $\{1.75, 3.25, 4.75\}$), with a fixed dielectric constant ratio (S = 3.5), viscosity ratio (λ = 1), and electric Reynolds number (Re_E = 0.01). The results include both sharp and smoothed interface models and are compared with the numerical findings of Cui, Wang and Liu (2019) and the theoretical predictions by Feng (2002), where no charge convection is considered, i.e., Re_E \rightarrow 0.

When the droplet deformation (Eq. 4.133) is negative, it indicates that the droplet deforms along the axis perpendicular to the direction of the applied electric field, resulting in a **oblate** shape. Conversely, positive deformation values represent deformation along the same direction as the applied electric field, leading to an **prolate** shape. The work of Feng (2002) introduced a first-order small deformation model, given by:

$$D = \frac{f_d(R, S)}{3(1+R)^2},$$
(6.1)

where $f_d = R^2 + R + 1 - 3S$ is a discriminating function that determines whether the droplet deforms into a prolate or oblate shape. Solving it for $f_d = 0$, the deformation regimes diagram for a single droplet under an applied electric field is mapped and visualized in Fig. 36, where three distinct regions are defined:

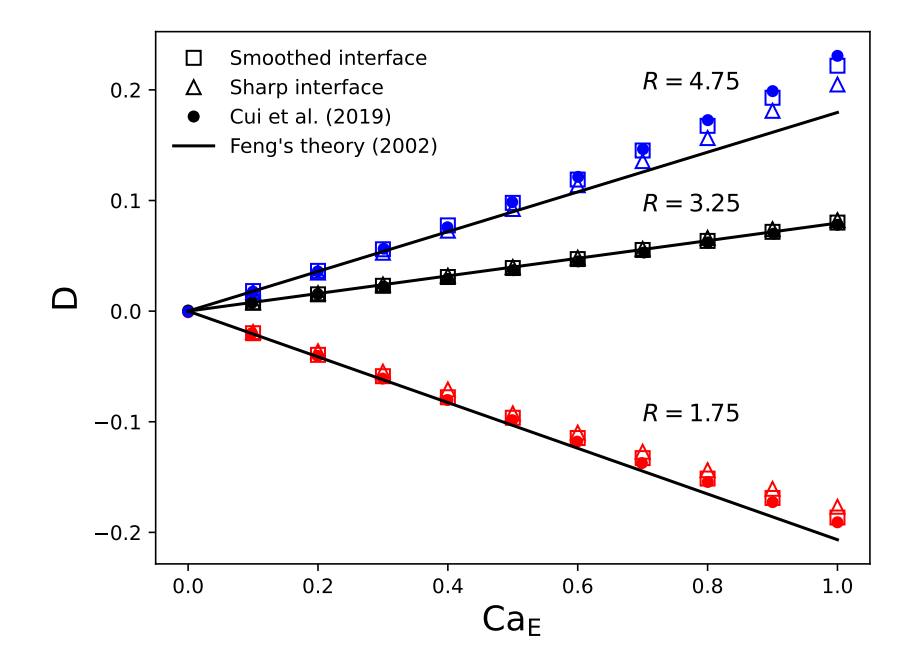


Figure 35 – Effects of Ca_E and R on droplet's deformation at S=3.5 and $Re_E=0.01$, and comparison with previous numerical results of Cui, Wang and Liu (2019).

- I. For S/R < 1, the droplet adopts a prolate shape with circulation directed from the equator to the poles.
- II. When S/R > 1, the droplet remains prolate, but the circulation reverses, flowing from the poles toward the equator.
- III. At sufficiently high S, the droplet deforms into an oblate shape while maintaining circulation from the poles to the equator.

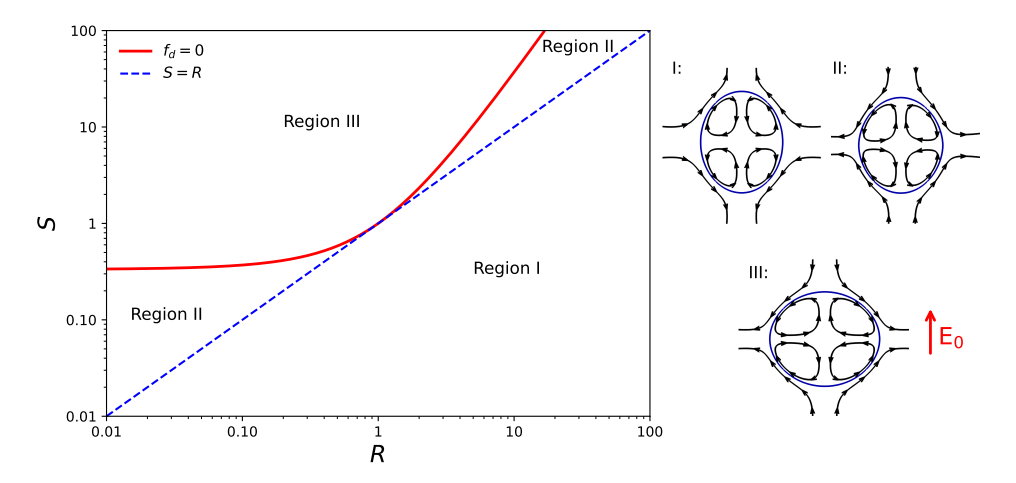


Figure 36 – Deformation regime diagram for a single droplet subjected to an applied electric field. The contour red line representing $f_d = 0$ delineates the transition between the prolate and oblate droplet shapes, depending on the values of S and R. The dashed blue line separates regions where the circulation flows from the equator to the poles (Region I) from regions where the circulation flows from the poles to the equator (Regions II and III).

In the context of the results presented in Fig. 35, where S=3.5, the transition value of R is 2.62. This implies that the droplet shape is oblate for R<2.62 and prolate for R>2.62, then only the results for R=1.75 exhibit an oblate shape. Both the smoothed and sharp interface models show close agreement with each other and with the results of Cui, Wang and Liu (2019). For R=3.25, close agreement is also observed, even at high electric capillary number ($Ca_E>0.6$), with the theoretical predictions of Feng (2002). However, for R=4.75, a slight mismatch occurs for $Ca_E>0.7$. Specifically, Cui, Wang and Liu (2019) reports a maximum deformation of 0.23, while the smoothed interface model predicts 0.22 and the sharp interface model predicts 0.20.

To further compare both interface models, Fig. 37 shows the pressure field contours for $S=3.5,\,R=1.75,\,\mathrm{and}\,\,\mathrm{Ca_E}=0.5$. The pressure range is consistent across both models, but a slight difference is observed in the width of the dark blue region (indicating low pressure) at the top and bottom of the domain. Specifically, the sharp interface model exhibits a broader low-pressure region compared to the smoothed interface model.

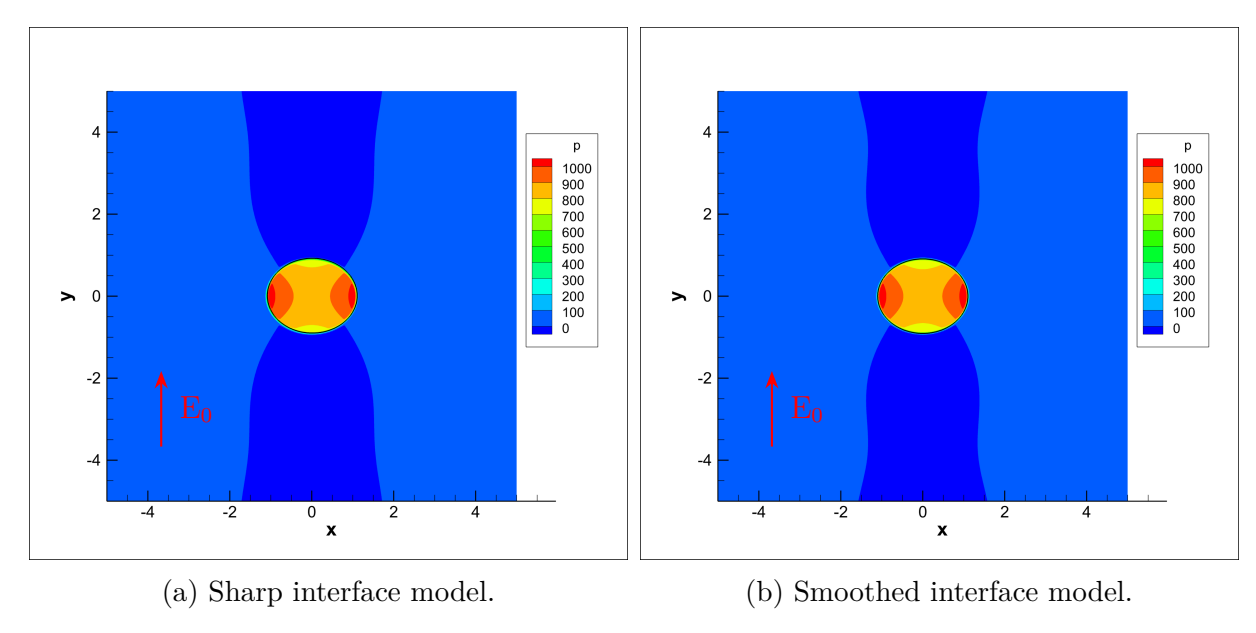


Figure 37 – Pressure contours for electrohydrodynamic flow for S=3.5, R=1.75, and $Ca_E=0.5.$ Results are shown for both sharp and smoothed interface models.

Contour maps of the electric charge density are shown in Fig. 38, along with the streamlines of the induced electrohydrodynamic flow. For the sharp interface model, the electric charge density q_s is concentrated precisely at the interface and varies only in the tangential direction. This is achieved using the closest point method, which ensures that q_s is strictly concentrated at the interface. In contrast, for the smoothed interface model, the electric charge density q_s is distributed around the interface and treated as a bulk quantity, rather than being confined strictly to the interface. The physically relevant quantity is the charge density at the interface, i.e., at $\phi = 0$, which is the main focus of both models.

The flow direction, from the poles to the equator, explains the oblate shape of the droplet. This occurs because the electrohydrodynamic forces stretch the droplet along the

x-axis, which is perpendicular to the direction of the applied electric field.

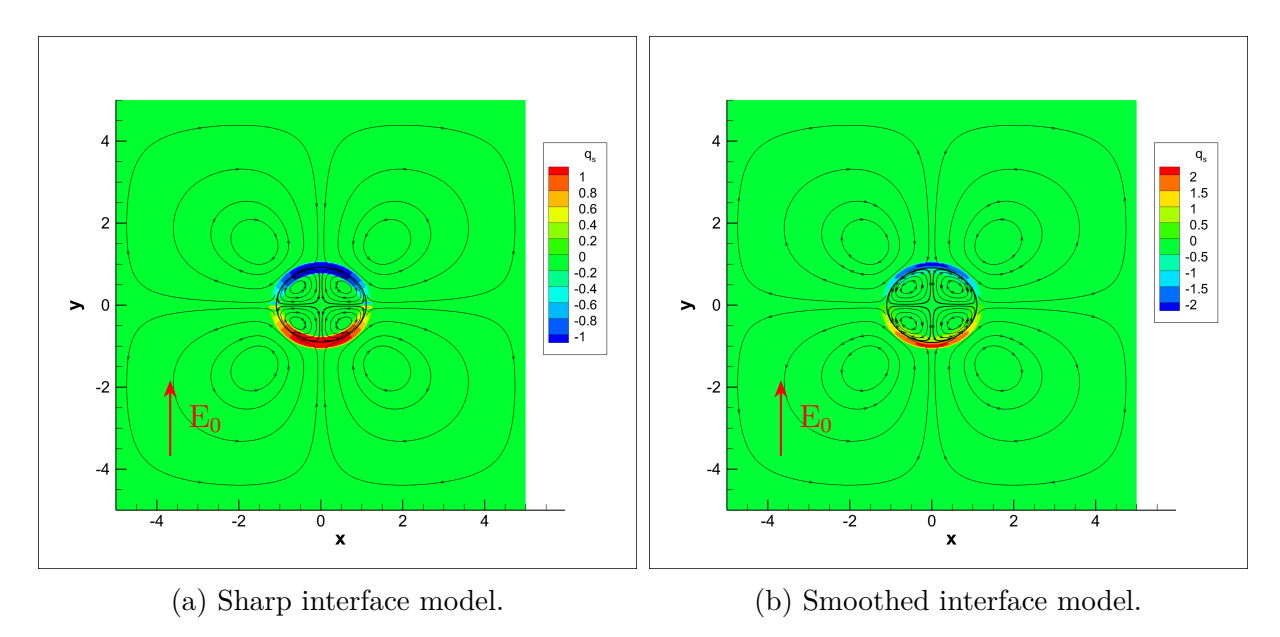


Figure 38 – Electric charge density contours and streamlines for electrohydrodynamic flow for S=3.5, R=1.75, and $Ca_E=0.5$. Results are shown for both sharp and smoothed interface models.

The main visual difference between the interface models lies in the electric field behavior. In the sharp interface model, the electric field exhibits a clear discontinuity across the droplet interface, as visualized in Fig. 39a. In contrast, the smoothed interface model shows a smooth transition between the electric field inside and outside the droplet (Figure 39b). Apart from this distinction, the contour ranges are nearly identical, with no other significant visual differences between the two models.

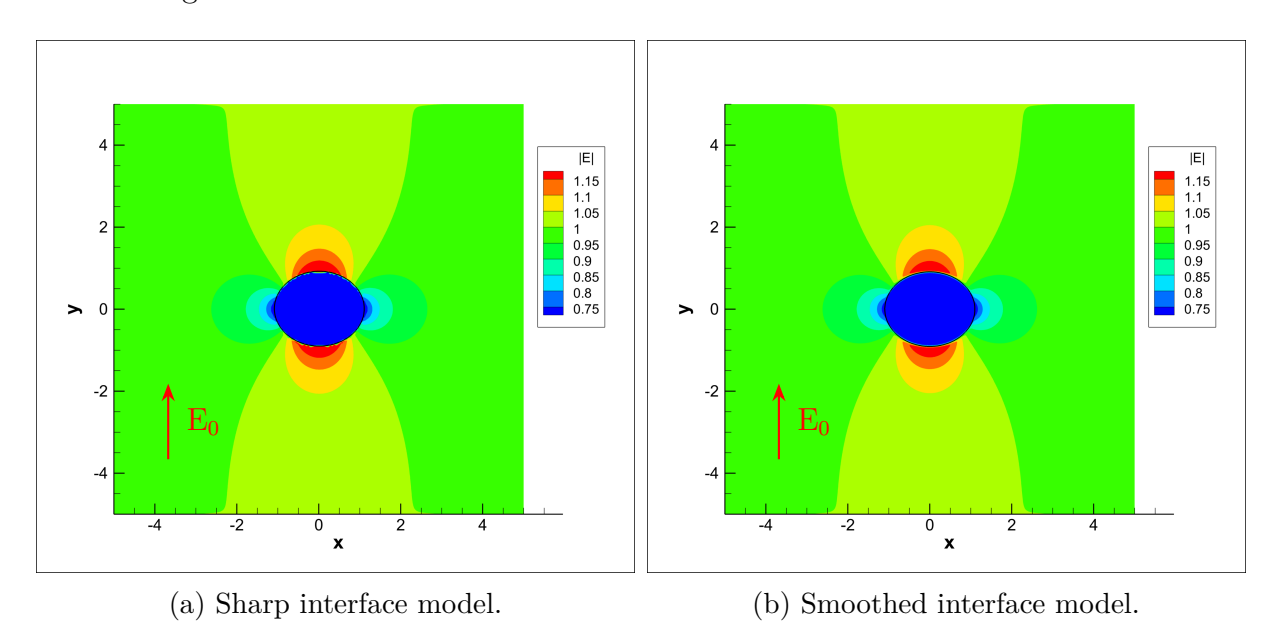


Figure 39 – Electric field magnitude contours for electrohydrodynamic flow for S=3.5, R=1.75, and $Ca_E=0.5$. Results are shown for both sharp and smoothed interface models.

Figure 40 presents a comparison of the Taylor deformation as a function of the

electric conductivity ratio for both sharp and smoothed interface models with the results of Dong and Sau (2018), and also theoretical predictions of Taylor (1966) and Feng (2002). The parameters fixed in these simulations were S=10, $Ca_E=0.18$, $Re_E=0.01$ and $\lambda=1$. For small values of R, the present results show a good agreement with both numerical simulation of Dong and Sau (2018) and theoretical predictions of Taylor (1966) and Feng (2002). Interestingly, while the present results begin to deviate from of Dong and Sau's results at higher R, the sharp interface model maintains a closer agreement with Feng's theoretical predictions. The smoothed interface model also shows a deviation from the sharp interface model at both low and high values of R, but the droplet shapes are virtually the same, as observed for R=1.8 and R=14.5 in Fig 40.

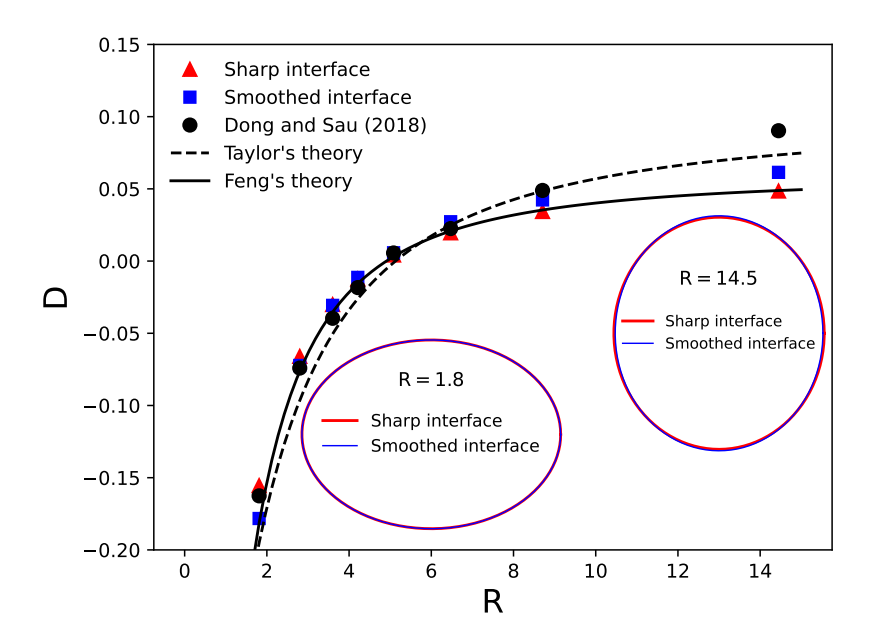


Figure 40 – Taylor deformation as a function of the electric conductivity ratio for S=10, $Ca_E=0.18$, $Re_E=0.01$ and $\lambda=1$. The insets show droplet contour for both interface models at R=1.8 and R=14.5.

6.2 Influence of surface charge convection on steady-deformation

The results in Section 6.1 were presented considering a simplified version of the Leaky Dielectric Model, which accounts for charge accumulation at the interface due to ohmic charge conduction. A more complex problem accounts for surface charge convection caused by the induced flow, whose intensity can be controlled by the electric Reynolds number. The effect of surface charge convection depends on the droplet shape. For oblate droplets, surface charge convection tends to suppress deformation, as shown in Fig. 41, where the droplet deformation (D), normalized by the deformation without surface charge convection (D_0) , decreases with the increase of Re_E for both interface models. These results are compared with those of Luo et al. (2020). The analysis was conducted for S = 3.5 and R = 1.75, which result in an oblate shape according to the phase diagram shown in Fig. 36, and for fixed $Ca_E = 0.5$.

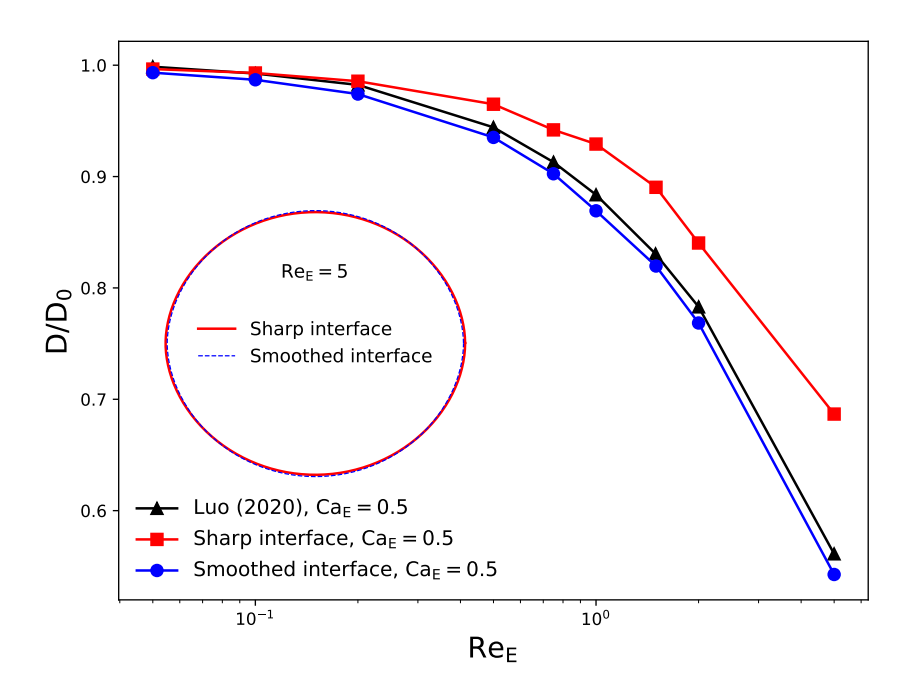


Figure 41 – Normalized deformation as a function of the electric Reynolds number for $S=3.5, R=1.75, Ca_E=0.5$ and $\lambda=1$. The deformations of the case without surface charge convection are $D_0=0.093$ and $D_0=0.096$ for the Sharp and Smoothed interface models, respectively. The inset presents the shape contour of the droplet for both interface models at $Re_E=5$.

The Smoothed interface model shows good agreement with the results of Luo et al. (2020), while the Sharp interface model shows greater deviation. At $Re_E = 5$, surface charge convection suppresses almost 50% of the deformation for the Smoothed interface model, while for the Sharp Interface Model, the suppression is slightly more than 30%. Despite this difference, the droplet shape remains nearly the same, as shown in the inset of Fig. 41.

In the case of a prolate shape, surface charge convection plays the opposite role: it enhances deformation. In Fig. 42, the normalized deformation increases with the increase of Re_E for S=0.5, R=2.0, $Ca_E=0.5$, and $\lambda=1$. Neither the Sharp interface model nor the Smoothed interface model matched the results of Luo et al. (2020). The effect of surface charge convection was smaller in the Sharp interface model compared to the Smoothed interface model, but in both cases, surface charge convection increased deformation by less than 1% compared to the case without surface charge convection. Although the results do not match quantitatively, they qualitatively predict the linear increase in deformation with the increase of Re_E . One possible reason for the discrepancy is the lack of upwinding in the numerical schemes used for surface charge convection. Upwinding is crucial for accurately capturing convective effects, especially in systems with strong directional flows, such as those induced by electric fields. Its absence in the current models may lead to an underestimation of the surface charge convection effects. Implementing upwinding could significantly improve the quantitative agreement with experimental or reference data, as it would better resolve the charge distribution and its impact on droplet deformation.

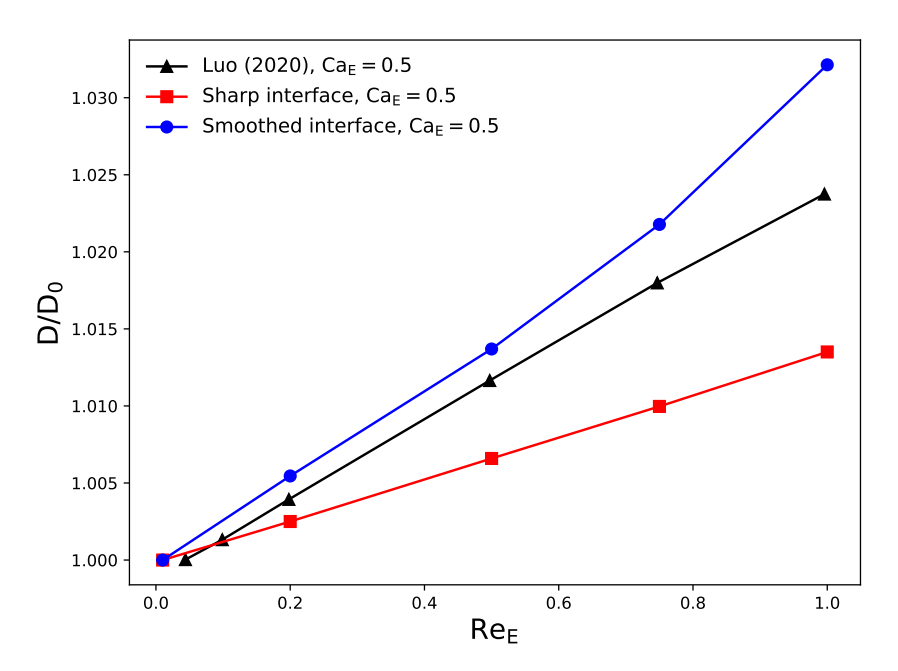


Figure 42 – Normalized deformation as a function of the electric Reynolds number for S = 0.5, R = 2.0, $Ca_E = 0.5$ and $\lambda = 1$. The deformations of the case without surface charge convection are $D_0 = 0.102$ and $D_0 = 0.106$ for the Sharp and Smoothed interface models, respectively.

6.3 Transient behavior

An interesting aspect to analyze is the transient droplet deformation of both oblate and prolate droplet shapes in the presence of surface charge convection. From this point forward, all results presented in this work will focus exclusively on the sharp interface model, as it provides robust capability to handle high variations in physico-chemical property ratios. Figure 43 illustrates the transient deformation for the two systems analyzed in the previous section at $Ca_E = 0.5$. For the oblate shape with S = 3.5 and R = 1.75, the influence of surface charge convection is significant compared to the prolate shape with S = 0.5 and S = 0.5 and S = 0.5 and S = 0.5.

For the oblate droplet at $Re_E = 0.01$ (with weak surface charge convection), the deformation exhibits a monotonic behavior and rapidly reaches a steady state. This indicates that the electric charge relaxation time is much smaller than the flow convection time ($t_e \ll t_f$). However, for $Re_E = 1.0$, the droplet initially exhibits a prolate deformation for t < 1.5. This behavior arises due to the delayed migration of electric charge from the bulk to the droplet surface, resulting in a significantly larger charge relaxation time compared to the case without surface charge convection ($t_{e,Re_E=1.0} \gg t_{e,Re_E=0.01}$). Beyond t > 1.5, the oblate deformation increases gradually until it reaches a steady state at approximately t = 13. For $Re_E = 5.0$, the initial prolate deformation is even more pronounced, persisting until t = 6.5. This extended duration is attributed to a further increase in the electric charge relaxation time ($t_{e,Re_E=5}$). In contrast, for the prolate configuration (blue lines in Fig. 43), the deformation increases monotonically, and the value

of Re_E has a small impact on the transient behavior.

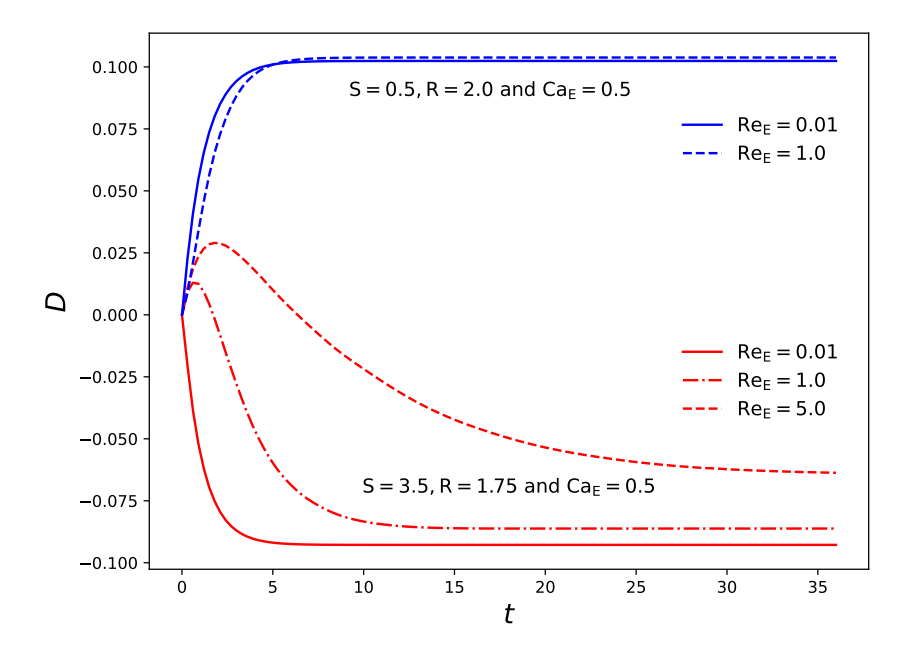


Figure 43 – Transient deformation for two configurations: oblate droplet (red) with $S=3.5,\ R=1.75,\ and\ Ca_E=0.5;$ prolate droplet (blue) with $S=0.5,\ R=2.0,\ and\ Ca_E=0.5.$

Another interesting transient behavior to analyze is the charge accumulation and convection over time for oblate droplets. Figure 44 presents the surface charge density q_s along the angular position θ along the droplet surface, as depicted in the inset, where $\theta=0$ and $\theta=\pi$ correspond to the poles, while $\theta=\pi/2$ represents the equatorial region. Note that the figure only displays half of the droplet surface due to symmetry, as the charge distribution is expected to be mirrored across the opposite hemisphere. Since the droplet shape is oblate, the circulation flows from the poles to the equator.

At the earliest time shown in Fig. 44 (t=3), the charge distribution is relatively smooth, with a gradual transition across the interface. The surface charge remains weakly negative for $\theta < \pi/2$ and weakly positive for $\theta > \pi/2$, indicating that at this stage, convection and accumulation effects are not yet dominant. As time progresses (t=9 and t=18), the charge distribution becomes more pronounced, with an increasing separation between the negatively charged upper hemisphere and the positively charged lower hemisphere. The transition at $\theta = \pi/2$ becomes steeper, suggesting an enhanced transport of charge along the interface.

At the latest time (t=36), the charge separation reaches its most intense state, with significant negative charge accumulation in the upper hemisphere and a strong positive charge in the lower hemisphere. The steep gradient observed near $\theta=\pi/2$ indicates a highly localized transition between charge regions. Additionally, small oscillations appear in the distribution, particularly near the equator, suggesting the emergence of more complex charge dynamics, potentially due to nonlinear interactions between charge transport mechanisms. The distinct separation of charges at the equator is a signature of a boundary

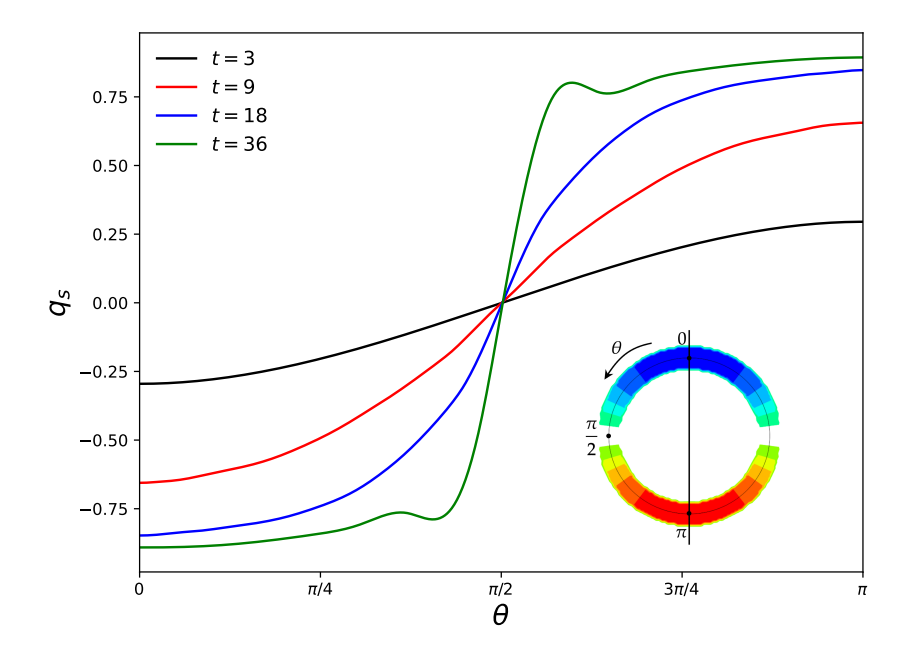


Figure 44 – Surface charge density as a function of the angular position θ for different time instants. Results are shown for S = 3.5, R = 1.75, Ca_E = 0.5 and Re_E = 5 for an oblate droplet. The inset defines θ around the droplet.

layer build up in this region due to the shock of unlike charges driven by the EHD flow. Recent analytical supports this result showing a finite-time singularity in surface charge density due to a shock of charges at the equator in the limit of strong surface charge convection (Peng et al., 2024).

For prolate droplets, when the circulation flows from the equator to the pole, the charge distribution exhibits distinct characteristics compared to the oblate droplet, as shown in Fig. 45. While charge accumulation over time remains a general phenomenon independent of the droplet shape, the surface charge convection in this case preferentially transports charge from the equatorial region towards the poles. This effect leads to a pronounced accumulation of positive charge in the upper hemisphere and negative charge in the lower hemisphere, leading to the formation of polar caps in agreement with recent analytical work (Peng et al., 2024). Additionally, the transition between hemispheres is notably smoother compared to other oblate case, indicating a more gradual redistribution of charge. The surface charge density evolves over time with charge progressively accumulating at the poles while the equatorial region depletes. The charge gradient becomes steeper as time advances, but it remains smooth rather than developing sharp transitions. At early times (t = 0.3), the charge distribution is relatively uniform, but as the system evolves, the convection-driven transport redistributes charge more efficiently towards the poles. Notably, in this case, the droplet reaches a steady-state configuration more quickly due to the weaker convective effects associated with $Re_E = 1$. In contrast, as shown in Fig. 44, when $Re_E = 5$, the stronger convection results in a longer accumulation time, delaying the steady-state charge distribution as a boundary layer builds up near the equator.

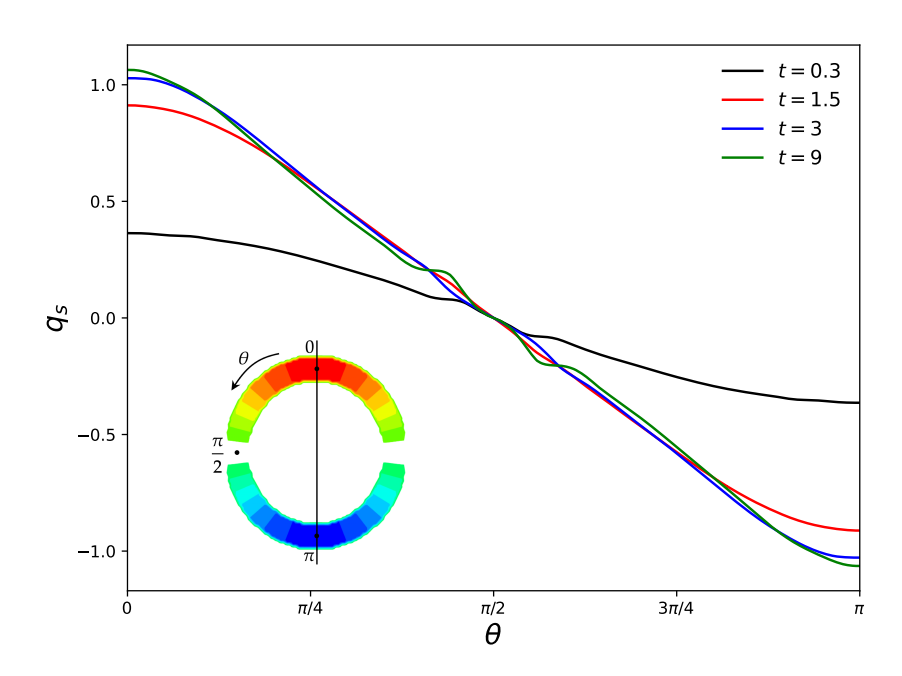


Figure 45 – Surface charge density as a function of the angular position θ for different time instants. Results are shown for S=0.5, R=2, $Ca_E=0.5$ and $Re_E=1$. The inset defines θ around the droplet.

6.4 Quincke Regime

Quincke rotation is a phenomenon in which a particle or droplet placed in an electric field begins to spontaneously rotate due to the interaction between the induced dipole moment and the applied field. This effect was first observed in rigid particles but has since been studied in fluid droplets as well (Quincke, 1896).

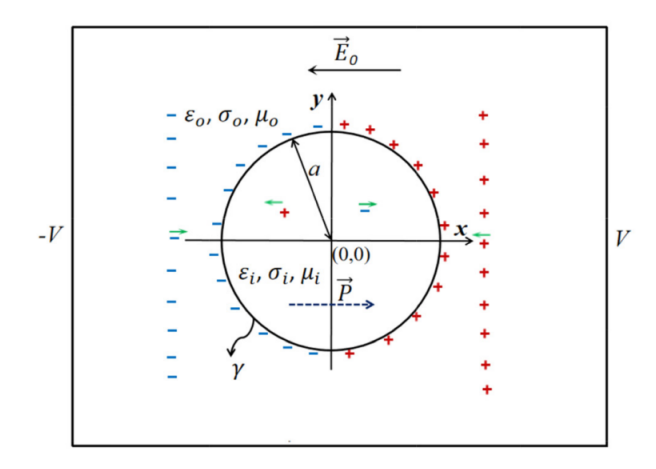
For a binary system, the key condition for Quincke rotation to occur is that the electric relaxation time of the inner phase $(\tau_{e,o})$ is greater than that of the outer phase $(\tau_{e,o})$, which can be expressed as S > R. This means that the free charge in the outer fluid reaches the interface more quickly, making the charge supply at the interface dependent primarily on the bulk phase charge (Dong; Sau, 2023). For rotation to be sustained, the applied electric field (E_0) must exceed a critical threshold (E_c) , which is the minimum field strength required to induce continuous rotation. For 2D droplets, this threshold is given by the expression derived by Feng (2002):

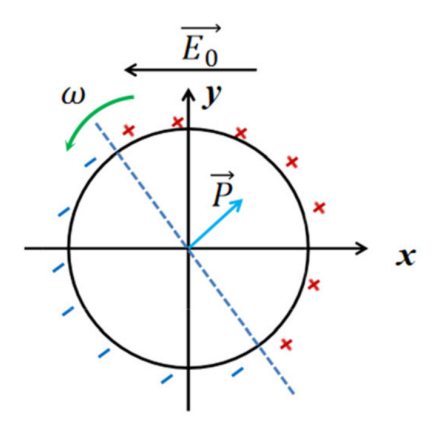
$$E_c = \sqrt{\frac{(1 + \frac{1}{S})(1 + R)\mu_o}{(1 - \frac{R}{S})\tau_e \epsilon_o}},$$
(6.2)

where τ_e is the electric relaxation time, expressed by ϵ_o/σ_o in this work.

As illustrated in Fig. 46, the induced dipole moment \mathbf{P} initially aligns opposite to the applied electric field \mathbf{E}_0 . If a perturbation displaces \mathbf{P} , a torque $\mathbf{T} = \mathbf{P} \times \mathbf{E}_0$ is generated, causing the droplet to rotate around an axis perpendicular to the electric field direction—this marks the onset of Quincke rotation. When the applied field strength exceeds the critical threshold ($\mathbf{E}_0 > \mathbf{E}_c$), the dipole no longer stabilizes in a fixed orientation.

Instead, it undergoes continuous reorientation, sustaining the rotational motion.





- (a) A weakly conducting droplet in an external electric field, where charge polarization induces a dipole moment ${\bf P}$ in the opposite direction to ${\bf E}_0$.
- (b) Formation of a misaligned dipole moment **P** due to the dynamic nature of interfacial charge redistribution.

Figure 46 – Illustration of a single droplet subjected to an applied electric field \mathbf{E}_0 . The misalignment of the induced dipole moment \mathbf{P} generates a torque, leading to the droplet's electrohydrodynamic rotation. (Adapted from Dong and Sau (2023)).

6.4.1 Single Quincke droplet rotation

The flow pattern around a droplet in the Quincke regime is investigated for a system with S=0.5 and R=0.01, ensuring the necessary conditions for Quincke rotation. The electric field intensity, maintained above the critical threshold, is controlled by $Ca_E=0.6$ and $Re_E=6.0$. Figure 47 illustrates the transition from an initial quadrupolar flow structure to a final circular flow, a hallmark of Quincke rotation. The flow, directed from the poles to the equator—a configuration previewed by Region III in Fig. 36—significantly deforms the droplet, transforming it into an oblate shape.

At the early stage (t = 50), the system exhibits a symmetric quadrupolar flow characterized by counter-rotating vortices around the droplet. The droplet remains centered, and the field-induced convection results in symmetric charge transport.

At t=100, the quadrupolar flow structure persists outside the droplet, but noticeable changes occur: the symmetric vortex pairs are positioned opposite to each other along the diagonal of the square domain, as if the symmetry axis had rotated by 45° relative to the initial stage. Inside the droplet, a break in symmetry becomes evident as the internal vortices start merging into a single central vortex.

By t = 115, a complete asymmetry emerges in the flow structure, marking the onset of Quincke rotation. The initially symmetric quadrupolar pattern collapses to a circular

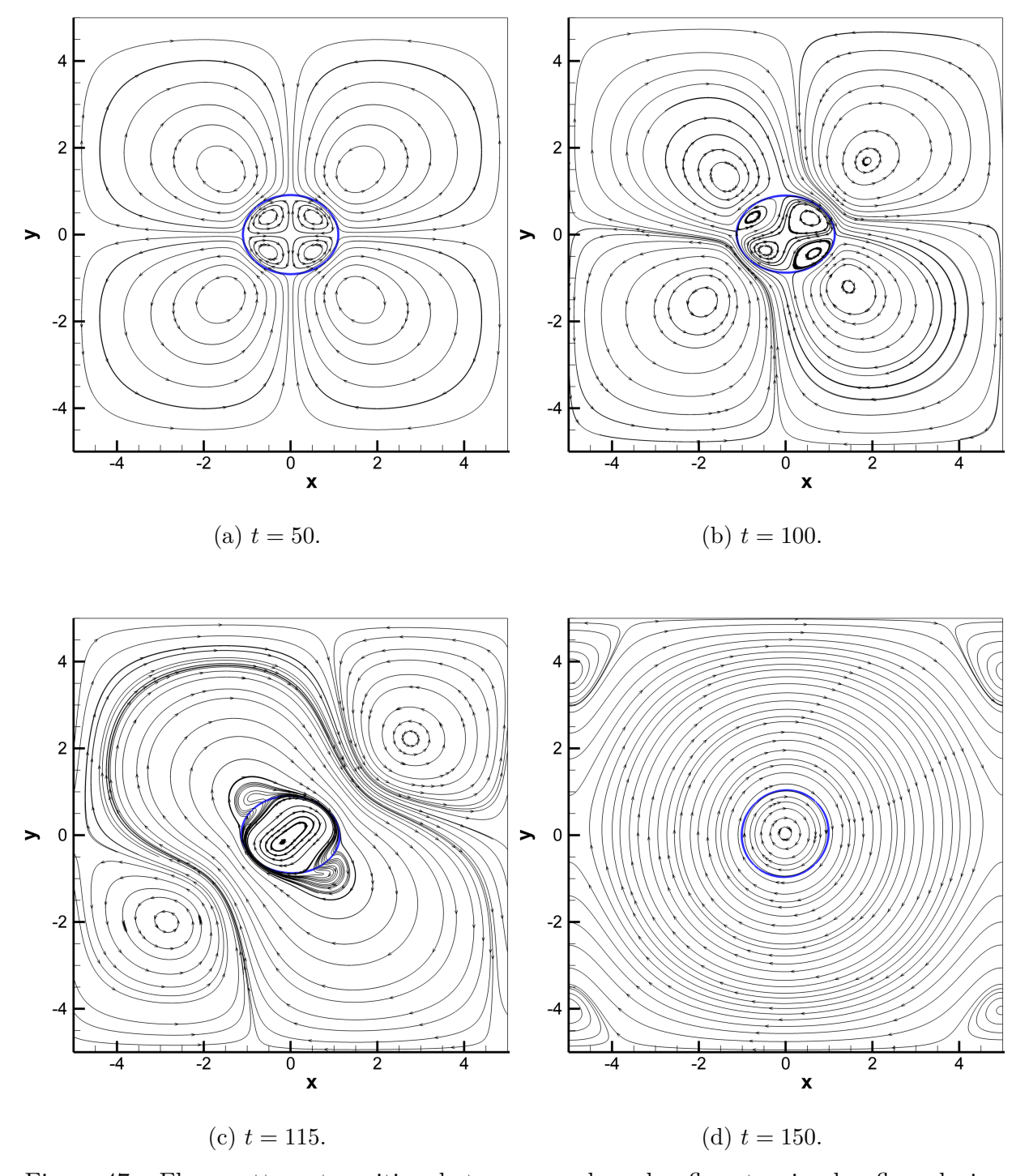


Figure 47 – Flow pattern transition between quadrupolar flow to circular flow during Quincke regime of a droplet for $S=0.5, R=0.01, Ca_E=0.6, Re_E=6.0$ and $\lambda=20$. The streamlines are plotted in black and droplet contour in blue.

deformed and elongated flow pattern. Assymetric irregular vortices are also visualized crossing the periodic boundaries.

At the final stage, shown at t=150, the flow transitions into a circular pattern, marking the fully developed Quincke rotation. The droplet rotates and restores its initial circular shape almost completely, eliminating most of the previous deformation. This occurs because the circular flow pattern no longer contains a stretching component,

preventing further deformation.

The deformation transition during Quincke rotation is illustrated in Fig. 48. For t < 100, the droplet remains in the Taylor regime, deforming into an oblate shape. During the interval 100 < t < 130, the deformation peaks at D = -0.12, after which the induced convection transports charges toward the equator, destabilizing the charge distribution and initiating the Quincke regime (as seen in Figs. 47b and 47c). Between 130 < t < 150, the deformation decreases significantly due to intense electro-rotation and build up of a circular flow. For t > 150, the deformation oscillates around D = -0.019, stabilizing at this value by t = 240.

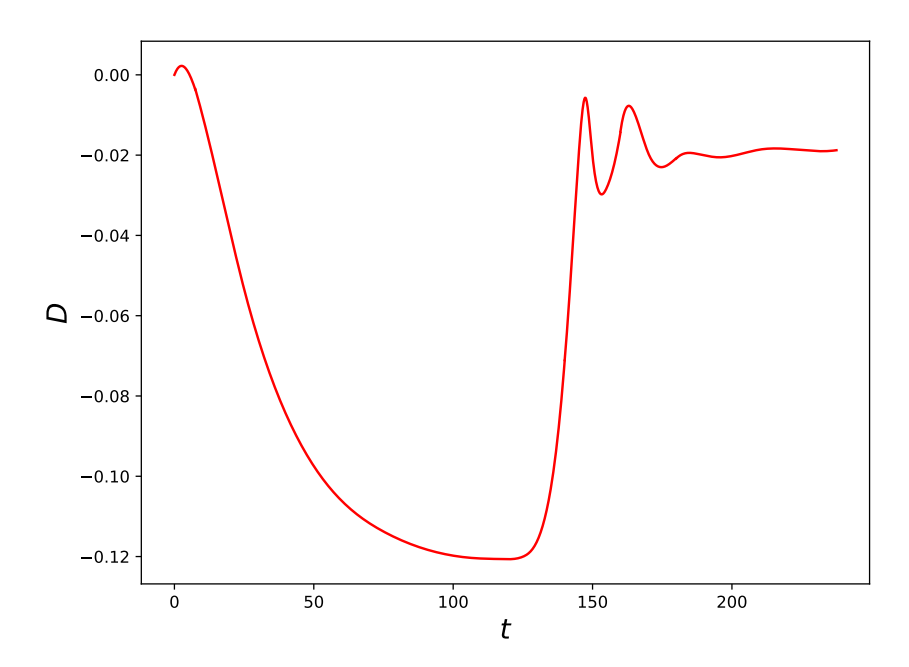


Figure 48 – Transient deformation during Quincke rotation of Fig. 47.

6.4.2 Tilt angle compared to rigid sphere

The dipole tilt angle, α , represents the angle between the induced dipole moment of the droplet and the direction of the applied electric field. This angle plays a crucial role in the dynamics of Quincke rotation, as it directly influences the induced torque and the resulting rotational motion. In this section, we compare the tilt angle of a viscous droplet to that of a rigid sphere.

For a high viscosity ratio ($\lambda \gg 1$), rotation is facilitated as the critical electric field strength, E_c , decreases. In this regime, the threshold for Quincke rotation of a droplet approaches that of a rigid sphere, making it easier for the droplet to rotate under an applied electric field. This behavior is consistent with Quincke rotation theory, which predicts that for sufficiently high viscosity ratios, the critical field strength is well approximated by $E_c \approx E_Q$ (Salipante; Vlahovska, 2010). To analyze this effect, we consider a system with material properties corresponding to those used in the work of Salipante and Vlahovska (2010), as detailed in Table 3.

Another key parameter governing this behavior is the Maxwell–Wagner capillary number, Ca_{MW} , which represents the ratio between the surface tension and charge relaxation timescales:

$$Ca_{MW} = \frac{t_{\gamma}}{t_{MW}} = \frac{\sigma_o \mu_o a}{\epsilon_o \gamma} \frac{(R+2)(\lambda+1)}{S+2}.$$
 (6.3)

This parameter reflects the balance between shape-restoring mechanisms and charge-induced deformation. For a fixed set of material properties, varying Ca_{MW} is equivalent to varying the drop size a. For small droplets, where Ca_{MW} is low, surface tension forces dominate, maintaining the droplet's approximately spherical shape and making its behavior more comparable to that of a rigid sphere. Conversely, for larger droplets with higher Ca_{MW} , deformation effects become more pronounced, potentially altering the dipole tilt angle and the onset conditions for Quincke rotation.

Table 3 – Material properties corresponding to the system used in experiments of Salipante and Vlahovska (2010) and other dimensional parameters.

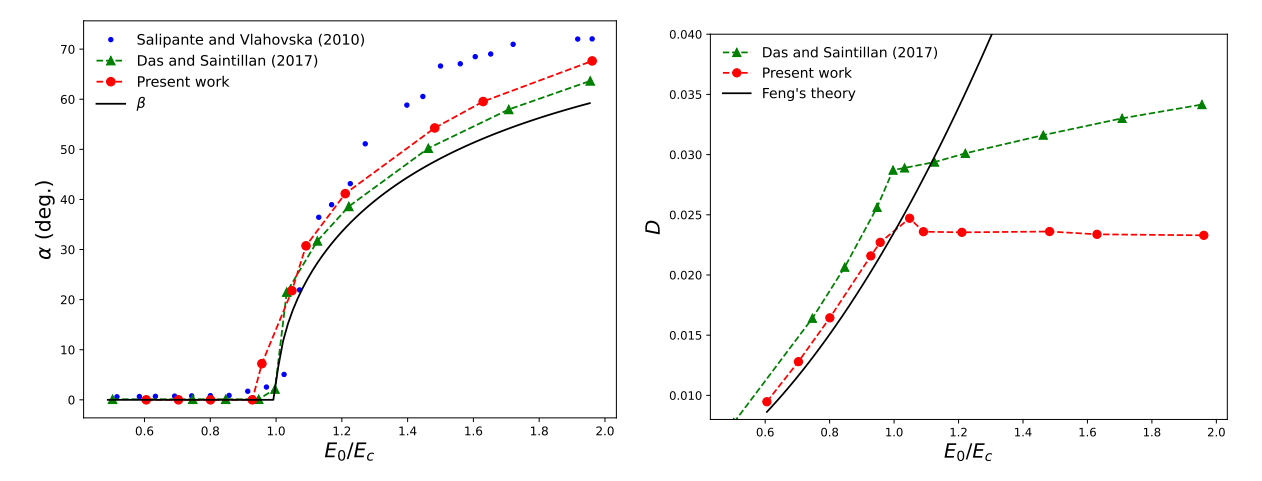
Parameter	Symbol	Typical Value
Dielectric constant (inner phase)	ϵ_i/ϵ_0	5.3
Dielectric constant (outer phase)	ϵ_o/ϵ_0	3.0
Electric conductivity (inner phase)	σ_i	$4.5 \times 10^{-11} \; \mathrm{S} \; \mathrm{m}^{-1}$
Electric conductivity (outer phase)	σ_o	$1.23 \times 10^{-12} \; \mathrm{S} \; \mathrm{m}^{-1}$
Viscosity (inner phase)	μ_i	$0.69 \mathrm{\ Pa\ s}$
Viscosity (outer phase)	μ_o	$9.74 \mathrm{\ Pa\ s}$
Interfacial tension	γ	$4.5~\mathrm{mN~m^{-1}}$
Droplet radius	a	$0.25, 0.90 \mathrm{mm}$
Electric field intensity	E_0	$1.0-4.0 \text{ kV cm}^{-1}$

Table 4 – Dimensionless parameters calculated using the material properties shown in Table 3.

Parameter	Symbol	Typical Value
Electric conductivity ratio	R	0.027
Dielectric permittivity	S	0.57
Viscosity ratio	λ	14.1
Maxwell-Wagner Capillary number	$\mathrm{Ca}_{\mathrm{MW}}$	0.44, 1.58
Electric Capillary number	$\mathrm{Ca_E}$	0.04 – 0.42
Electric Reynolds number	Re_E	1.07–11.34

In the following, the tilt angle as a function of the applied electric field normalized by the critical threshold electric field, calculated using Eq. (6.2), is visualized in Fig. 49a. The solid black line is the complementary of the angle between the steady dipole and applied electric field in the case of a rigid sphere, which can be denoted by β (Salipante; Vlahovska, 2010):

$$\beta = \frac{\pi}{2} - \arctan\left[\left(\frac{E_0^2}{E_c^2} - 1\right)^{-\frac{1}{2}}\right] \tag{6.4}$$



(a) Steady tilt angle as a function of the nor- (b) Steady deformation as a function of the nor- malized electric field.

Figure 49 – Both numerical and experimental results correspond to the system described in Table 3. The experimental data from Salipante and Vlahovska (2010) were obtained at $Ca_{MW} = 1.58$, whereas the present work and the simulations of Das and Saintillan (2017) were conducted at $Ca_{MW} = 0.44$.

Except for the early onset of the Quincke regime at $E_0/E_c \approx 0.93$ in the present work, the numerical results from this study (red circles) and those of Das and Saintillan (2017) (green triangles) closely match the experimental data of Salipante and Vlahovska (2010) (blue dots) for $E_0/E_c < 1.2$. However, for $E_0/E_c > 1.2$, the experimental tilt angles increase more steeply than the numerical predictions. This deviation can be attributed to the higher capillary number ($Ca_{MW} = 1.58$) in the experiments, which enhances droplet deformation and modifies the induced dipole dynamics.

The differences in computational approaches further contribute to the observed discrepancies. While Das and Saintillan (2017) employed a 3D Boundary Element Method (BEM), which inherently accounts for more complex interfacial dynamics, the present study follows a 2D formulation. As a result, the 3D model exhibits slightly lower tilt angles across the entire range of E_0/E_c , whereas the 2D approach captures the overall trends but lacks certain interfacial degrees of freedom, and possible curvature-induced effects in the azimuthal direction.

The presence of deformation also plays a crucial role in distinguishing the behavior of a droplet from that of a rigid sphere. Even at low Ca_{MW} values, the droplet's shape deviates from a perfect sphere, leading to systematically higher tilt angles compared to the rigid case. The reference black line in Fig. 49a serves as a benchmark, showing that for most cases, the droplet exhibits larger tilt angles than a rigid sphere due to its ability to deform. This effect becomes even more pronounced at higher electric field strengths, where deformation and charge redistribution further alter the droplet's rotational response.

In terms of deformation (seen in Fig. 49b), the present work captures the transition between the Taylor and Quincke regimes, demonstrating consistency with Das and Saintillan (2017) results for $E_0/E_c < 1.0$. However, in the Quincke regime, the deformation

behavior differs: the present work shows a stabilization at $D \approx 0.024$, whereas Das and Saintillan's BEM simulations indicate a gradual increase in deformation. This distinction arises from the additional degrees of freedom in the 3D formulation, which allow for more complex interfacial effects and local charge redistribution.

7 Conclusion

This master's thesis advances the understanding of droplet dynamics in multifield environments by systematically investigating two critical aspects: (1) the interplay of ionic surfactants, shear flow, and electrostatic effects on droplet dynamics, and (2) the electrohydrodynamic response of clean droplets under applied electric fields, with a focus on droplet deformation, charge convection, and Quincke rotation.

Through a robust numerical framework integrating level-set and closest-point methods, we demonstrate that insoluble ionic surfactants dynamically redistribute under shear and self-generated electric fields, governing droplet deformation through competing mechanisms of advection, diffusion, and electromigration. The Mason number, that controls the charge intensity of the ionic surfactant, plays a pivotal role: small Mason numbers lead to significant droplet deformation due to strong electrostatic effects, while high Mason numbers diminish these effects, resulting only in the deformation provided by the extensional component of shear flow. The mobility ratio, which governs electromigration along the droplet interface, shifts the peak surfactant concentration away from the droplet tips, altering the charge distribution and influencing the overall shape evolution.

For the electrohydrodynamics of droplets, two interface representations were proposed: a sharp interface model, integrating level-set, closest point, and ghost fluid methods; and a smoothed interface model, relying solely on the level-set method. Both models excelled in predicting steady deformation in weak electric field regimes, and the influence of surface charge convection with the electric Reynolds number. However, only the sharp interface model could handle strong variations of property ratios, enabling a deeper analysis of the transition to Quincke rotation. The transition in flow pattern during Quincke rotation was also investigated and the tilt angle was compared with numerical and experimental results, showing good agreement while deviating slightly from rigid sphere theory, underscoring the role of droplet deformation and interface mobility.

These findings provide foundational insights and open numerous opportunities for future research, as outlined below:

Emulsion Stabilization and Droplet Interactions:

- Extend the current framework to study pairwise droplet interactions under electrostatic forces, focusing on how electrostatic effects and surfactant-mediated repulsion influence coalescence and emulsion microstructure.
- Investigate diffusion dynamics in concentrated emulsions, incorporating long-range electrostatic interactions to predict bulk rheological properties (e.g., effective vis-

cosity and normal stress differences).

Electrohydrodynamics and Collective Phenomena:

- Explore collective propulsion via synchronized electrorotation of droplet arrays, where hydrodynamic and electrostatic interactions generate coordinated motion. Such systems could enable novel applications in targeted drug delivery, microfluidic mixing, and wireless control of microscale devices.
- Integrate both studies by investigating the electrohydrodynamics of surfactantcovered droplets to understand how surface-active molecules impact droplet deformation, electrorotation, and interactions in both pairwise and multi-droplet systems.

This work is innovative in integrating surfactant transport dynamics with electrostatic effects mediated by charged ions, providing a comprehensive framework to study the coupled interplay of interfacial mechanics and electrostatics. In addition, by proposing an efficient and versatile numerical methodology, we have established the groundwork for investigating more complex phenomena in droplet electrohydrodynamics, such as collective droplet interactions and field-induced Quincke rotation.

Bibliography

- Abbasi, M. S. et al. Electro-hydrodynamics of emulsion droplets: Physical insights to applications. *Micromachines*, v. 11, p. 942, 2020. Cited on page 7.
- Adami, S.; Hu, X.; Adams, N. A conservative sph method for surfactant dynamics. Journal of Computational Physics, v. 229, p. 1909–1926, 03 2010. Cited on page 4.
- Ajayi, O. O. A note on taylor's electrohydrodynamic theory. *Proceedings of the Royal Society of London. Series A. Mathematical and Physical Sciences*, v. 364, p. 499–507, 1978. Cited on page 6.
- Alidoost, M.; Pishevar, A. On importance of the surface charge transport equation in numerical simulation of drop deformation in a direct current field. *Journal of Fluids Engineering*, v. 140, p. 121201, 06 2018. Cited on page 9.
- Allan, R. S.; Mason, S. G. Particle behaviour in shear and electric fields: I. deformation and burst of fluid drops. *Proceedings of the Royal Society of London. Series A. Mathematical and Physical Sciences*, v. 267, p. 45–61, 1962. Cited 2 times on pages 5 and 6.
- Alvarez, N. J. et al. Using bulk convection in a microtensiometer to approach kinetic-limited surfactant dynamics at fluid-fluid interfaces. *Journal of Colloid and Interface Science*, v. 372, n. 1, p. 183–191, 2012. ISSN 0021-9797. Available on: https://www.sciencedirect.com/science/article/pii/S0021979711015232. Cited on page 3.
- Alvarez, N. J.; Walker, L. M.; Anna, S. L. A microtensiometer to probe the effect of radius of curvature on surfactant transport to a spherical interface. *Langmuir*, v. 26, n. 16, p. 13310–13319, 2010. PMID: 20695573. Available on: https://doi.org/10.1021/la101870m. Cited on page 3.
- Aris, R. Vectors, Tensors, and the Basic Equations of Fluid Mechanics. : Dover Publications, 1989. ISBN 978-0486661100. Cited on page 13.
- Arp, P. A.; Foister, R. T.; Mason, S. G. Some electrohydrodynamic effects in fluid dispersions. *Advances in Colloid and Interface Science*, v. 12, p. 295–356, 1980. Cited on page 6.
- Badalassi, V.; Ceniceros, H.; Banerjee, S. Computation of multiphase systems with phase field models. *Journal of Computational Physics*, v. 190, p. 371–397, 09 2003. Cited on page 41.
- Bancroft, W. D. The theory of emulsification. *Journal of Physical Chemistry*, ACS Publications, v. 17, 1913. Cited on page 1.
- Barrett, J. W.; Garcke, H.; Nürnberg, R. On the stable numerical approximation of two-phase flow with insoluble surfactant. *ESAIM: Mathematical Modelling and Numerical Analysis*, v. 49, n. 2, p. 421–458, 2015. Available on: http://www.numdam.org/articles/10.1051/m2an/2014039/>. Cited on page 3.

- Barrett, J. W.; Garcke, H.; Nürnberg, R. Stable finite element approximations of two-phase flow with soluble surfactant. *Journal of Computational Physics*, v. 297, p. 530–564, 2015. ISSN 0021-9991. Available on: https://www.sciencedirect.com/science/article/pii/S0021999115003630. Cited on page 3.
- Basaran, O. A. Small-scale free surface flows with breakup: Drop formation and emerging applications. *Annual Review of Fluid Mechanics*, v. 34, p. 1–32, 2002. Cited on page 5.
- Baygents, J. C.; Rivette, N. J.; Stone, H. A. Electrohydrodynamic deformation and interaction of drop pairs. *Journal of Fluid Mechanics*, v. 368, p. 359–375, 1998. Cited 2 times on pages 6 and 7.
- Behera, N.; Mandal, S.; Chakraborty, S. Electrohydrodynamic settling of drop in uniform electric field: Beyond stokes regime. *Journal of Fluid Mechanics*, v. 881, p. 498–523, 2019. Cited on page 7.
- Bibette, J.; Calderon, L.; Poulin, P. Emulsions: Basic principles. *Reports on Progress in Physics*, IOP Publishing, v. 62, n. 6, p. 969–1033, 1999. Cited on page 1.
- Binks, B. Particles as surfactants—similarities and differences. Current Opinion in Colloid & Interface Science, Elsevier, v. 9, n. 5, p. 381–388, 2004. Cited on page 1.
- Borwankar, R.; Wasan, D. The kinetics of adsorption of ionic surfactants at gas-liquid surfaces. *Chemical Engineering Science*, v. 41, n. 1, p. 199–201, 1986. ISSN 0009-2509. Available on: https://www.sciencedirect.com/science/article/pii/0009250986852174. Cited on page 2.
- Borwankar, R.; Wasan, D. Equilibrium and dynamics of adsorption of surfactants at fluid-fluid interfaces. *Chemical Engineering Science*, v. 43, n. 6, p. 1323–1337, 1988. ISSN 0009-2509. Available on: https://www.sciencedirect.com/science/article/pii/0009250988851066. Cited on page 2.
- Bouasse, H. Capillarité. Phénomènes Superficiels. Coulommiers: Impr. Paul Brodard, 1924. (Bibliothèque Scientifique de l'Ingénieur et du Physicien). In-8, XXI-437 p. avec figures [21]. Cited on page 1.
- Brackbill, J.; Kothe, D.; Zemach, C. A continuum method for modeling surface tension. Journal of Computational Physics, v. 100, n. 2, p. 335–354, 1992. ISSN 0021-9991. Available on: https://www.sciencedirect.com/science/article/pii/002199919290240Y. Cited on page 14.
- Brazier-Smith, P. R.; Jennings, S. G.; Latham, J. An investigation of the behaviour of drops and drop-pairs subjected to strong electrical forces. *Proceedings of the Royal Society of London. Series A. Mathematical and Physical Sciences*, v. 325, p. 363–376, 1971. Cited on page 6.
- Brooks, D. E. et al. Electrostatic and electrokinetic potentials in two polymer aqueous phase systems. *Journal of Colloid and Interface Science*, v. 102, p. 1–13, 1984. Cited on page 6.
- Casandra, A. et al. Adsorption kinetics of the ionic surfactant decanoic acid. *International Journal of Heat and Mass Transfer*, v. 102, p. 36–44, 2016. ISSN 0017-9310. Available on: https://www.sciencedirect.com/science/article/pii/S0017931015303732. Cited on page 3.

- Casandra, A. et al. Adsorption kinetics of the partially dissociated ionic surfactants: The effect of degree of dissociation. *Journal of the Taiwan Institute of Chemical Engineers*, v. 92, 02 2018. Cited on page 3.
- Chu, J.; Tsai, R. Volumetric variational principles for a class of partial differential equations defined on surfaces and curves. *Research in the Mathematical Sciences*, v. 5, 04 2018. Cited on page 4.
- Cui, Y.; Wang, N.; Liu, H. Numerical study of droplet dynamics in a steady electric field using a hybrid lattice boltzmann and finite volume method. *Physics of Fluids*, v. 31, 02 2019. Cited 4 times on pages x, 71, 72, and 73.
- Das, D.; Saintillan, D. A nonlinear small-deformation theory for transient droplet electrohydrodynamics. *J. Fluid Mech.*, v. 810, p. 225–253, 2016. Cited on page 7.
- Das, D.; Saintillan, D. Electrohydrodynamics of viscous drops in strong electric fields: numerical simulations. *J. Fluid Mech.*, v. 829, p. 127–152, 2017. Cited 4 times on pages xi, 7, 8, and 85.
- Datwani, S. S.; Stebe, K. J. The dynamic adsorption of charged amphiphiles: The evolution of the surface concentration, surface potential, and surface tension. *Journal of Colloid and Interface Science*, v. 219, n. 2, p. 282–297, 1999. ISSN 0021-9797. Available on: https://www.sciencedirect.com/science/article/pii/S0021979799964949. Cited on page 15.
- Davies, J.; Rideal, E. Interfacial phenomena.: Academic Press, 1963. Cited on page 2.
- Davies, J. T. The distribution of ions under a charged monolayer, and a surface equation of state for charged films. *Proceedings of the Royal Society of London. Series A, Mathematical and Physical Sciences*, v. 208, p. 224–247, 1951. Cited on page 2.
- Deng, B.; Schroën, K.; de Ruiter, J. Dynamics of bubble formation in spontaneous microfluidic devices: Controlling dynamic adsorption via liquid phase properties. *Journal of Colloid and Interface Science*, v. 622, p. 218–227, 2022. ISSN 0021-9797. Available on: https://www.sciencedirect.com/science/article/pii/S0021979722006841. Cited on page 3.
- Dong, Q.; Sau, A. Electrohydrodynamic interaction, deformation, and coalescence of suspended drop pairs at varied angle of incidence. *Physical Review Fluids*, v. 3, 07 2018. Cited 2 times on pages 7 and 75.
- Dong, Q.; Sau, A. Unsteady electrorotation of a viscous drop in a uniform electric field. *Physics of Fluids*, v. 35, p. 047116, 2023. Cited 5 times on pages xi, 7, 22, 80, and 81.
- Dong, X. et al. Collective propulsion of viscous drop pairs based on quincke rotation in a uniform electric field. *Physics of Fluids*, v. 36, p. 017134, 2024. Cited on page 8.
- Dukhin, S.; Miller, R. On the theory of adsorption kinetics of ionic surfactants at fluid interfaces 3. generalization of the model. *Colloid & Polymer Science*, v. 269, p. 923–928, 1991. Cited on page 2.
- Dukhin, S.; Miller, R.; Kretzschmar, G. On the theory of adsorption kinetics of ionic surfactants at fluid interfaces. *Colloid & Polymer Science*, v. 261, p. 335–339, 1983. Cited on page 2.

- Dziuk, G.; Elliott, C. M. Finite elements on evolving surfaces. *IMA Journal of Numerical Analysis*, v. 27, n. 2, p. 262–292, 04 2007. ISSN 0272-4979. Available on: https://doi.org/10.1093/imanum/drl023. Cited on page 3.
- Dziuk, G.; Elliott, C. M. A fully discrete evolving surface finite element method. SIAM Journal on Numerical Analysis, v. 50, n. 5, p. 2677–2694, 2012. Available on: https://doi.org/10.1137/110828642. Cited on page 3.
- Dziuk, G.; Elliott, C. M. Finite element methods for surface pdes. *Acta Numerica*, v. 22, p. 289–396, 2013. Cited on page 3.
- Eastoe, J.; Dalton, J. Dynamic surface tension and adsorption mechanisms of surfactants at the air-water interface. *Advances in colloid and interface science*, v. 85, p. 103–44, 04 2000. Cited on page 2.
- Einstein, A. On the movement of small particles suspended in stationary liquids required by the molecular-kinetic theory of heat. *Annalen der Physik*, v. 322, n. 8, p. 549–560, 1905. Cited on page 17.
- Fainerman, V.; Lucassen-Reynders, E. Adsorption of single and mixed ionic surfactants at fluid interfaces. *Advances in colloid and interface science*, v. 96, p. 295–323, 03 2002. Cited on page 2.
- Fainerman, V.; Lucassen-Reynders, E.; Miller, R. Adsorption of surfactants and proteins at fluid interfaces. *Colloids and Surfaces A: Physicochemical and Engineering Aspects*, v. 143, p. 141–165, 1998. Cited on page 2.
- Fainerman, V.; Lucassen-Reynders, E.; Miller, R. Description of the adsorption behaviour of proteins at water/fluid interfaces in the framework of a two-dimensional solution model. *Advances in Colloid and Interface Science*, v. 106, n. 1, p. 237–259, 2003. ISSN 0001-8686. Available on: https://www.sciencedirect.com/science/article/pii/S000186860300112X. Cited on page 2.
- Feng, J. Q. Electrohydrodynamic behavior of a drop subjected to a steady uniform electric field at finite electric reynolds number. *Proceedings of the Royal Society of London. Series A: Mathematical, Physical and Engineering Sciences*, v. 455, p. 2245–2269, 1999. Cited on page 6.
- Feng, J. Q. A 2d electrohydrodynamic model for electrorotation of fluid drops. *Journal of Colloid and Interface Science*, v. 246, n. 1, p. 112–121, 2002. ISSN 0021-9797. Available on: https://www.sciencedirect.com/science/article/pii/S0021979701980373. Cited 5 times on pages 6, 71, 73, 75, and 80.
- Feng, J. Q.; Scott, T. C. A computational analysis of electrohydrodynamics of a leaky dielectric drop in an electric field. *Journal of Fluid Mechanics*, v. 311, p. 289–326, 1996. Cited on page 6.
- Firouznia, M.; Bryngelson, S. H.; Saintillan, D. A boundary integral method for electrohydrodynamics of drops with inertia. *Journal of Computational Physics*, v. 489, p. 112248, 2023. Cited on page 8.
- Frumkin, A. Die kapillarkurve der höheren fettsäuren und die zustandsgleichung der oberflächenschicht. Zeitschrift für physikalische Chemie, v. 116, p. 466–484, 1925. Cited on page 1.

- Gao, T.; Rosen, M. J. Dynamic surface tension of aqueous surfactant solutions: 7. physical significance of dynamic parameters and the induction period. *Journal of Colloid and Interface Science*, v. 172, n. 1, p. 242–248, 1995. ISSN 0021-9797. Available on: https://www.sciencedirect.com/science/article/pii/S0021979785712489. Cited on page 2.
- Gennes, P.-G. de; Brochard-Wyart, F.; Quéré, D. Capillarity and Wetting Phenomena: Drops, Bubbles, Pearls, Waves. New York: Springer, 2004. Cited on page 1.
- Gupta, B. D. Golden Numerical Analysis. 1. ed.: Laxmi Publications, 2005. 332 p. ISBN 978-8170080572. Cited on page 27.
- Haywood, R.; Renksizbulut, M.; Raithby, G. Transient deformation of freely-suspended liquid droplets in electrostatic fields. *AIChE Journal*, v. 37, p. 1305–1317, 1991. Cited on page 6.
- Hua, J.-S.; Lim, L.-K.; Wang, C.-H. Numerical simulation of deformation/motion of a droplet subjected to electric field in microchannels. *Physics of Fluids*, v. 20, p. 11302–11317, 2008. Cited on page 6.
- Israelachvili, J. *Intermolecular and Surface Forces.* 3rd. ed. : Academic Press, 2011. Cited on page 1.
- James, A.; Lowengrub, J. A surfactant-conserving volume-of-fluid method for interfacial flows with insoluble surfactant. *Journal of Computational Physics*, v. 201, p. 685–722, 12 2004. Cited on page 4.
- Jesus, W. et al. A 3d front-tracking approach for simulation of a two-phase fluid with insoluble surfactant. *Journal of Computational Physics*, v. 281, 01 2015. Cited on page 4
- Jones, T. B. Dielectrophoretic force calculation. *Journal of Electrostatics*, v. 6, p. 69–82, 1979. Cited on page 6.
- Jones, T. B.; Kallio, G. A. Dielectrophoretic levitation of spheres and shells. *Journal of Electrostatics*, v. 6, p. 207–224, 1979. Cited on page 6.
- Kang, M.; Fedkiw, R.; Liu, X.-d. A boundary condition capturing method for multiphase incompressible flow. *Journal of Scientific Computing*, v. 15, 11 2000. Cited 2 times on pages 4 and 38.
- Kim, J.; Moin, P. Application of a fractional-step method to incompressible navier-stokes equations. *Journal of Computational Physics*, v. 59, n. 2, p. 308–323, 1985. ISSN 0021-9991. Available on: https://www.sciencedirect.com/science/article/pii/0021999185901482. Cited 2 times on pages viii and 28.
- Lanauze, J. A.; Walker, L. M.; Khair, A. S. The influence of inertia and charge relaxation on electrohydrodynamic drop deformation. 2013. Cited on page 7.
- Lanauze, J. A.; Walker, L. M.; Khair, A. S. Nonlinear electrohydrodynamics of slightly deformed oblate drops. *Journal of Fluid Mechanics*, v. 774, p. 245–266, 2015. Cited 2 times on pages 7 and 24.
- Langevin, D.; Argillier, J.-F. Interfacial behavior of asphaltenes. *Advances in Colloid and Interface Science*, v. 233, p. 83–93, 2016. ISSN 0001-8686. Clayton Radke Festschrift. Available on: https://www.sciencedirect.com/science/article/pii/S0001868615001761. Cited on page 2.

- Langmuir, I. The distribution and orientation of molecules. In: *Colloid Symposium Monograph.* 1925. p. 48–75. Cited on page 1.
- Langmuir, I. Surface Chemistry. 1932. Nobel Lecture. Accessed: April 9, 2025. Available on: https://www.nobelprize.org/prizes/chemistry/1932/langmuir/lecture/. Cited on page 15.
- Lenz, M.; Nemadjieu, S.; Rumpf, M. A convergent finite volume scheme for diffusion on evolving surfaces. *SIAM J. Numerical Analysis*, v. 49, p. 15–37, 01 2011. Cited on page 4.
- Leung, S.; Zhao, H. A grid based particle method for moving interface problems. *J. Comput. Physics*, v. 228, p. 2993–3024, 05 2009. Cited on page 4.
- Li, X.; Pozrikidis, C. The effect of surfactants on drop deformation and on the rheology of dilute emulsions in stokes flow. *Journal of Fluid Mechanics*, v. 341, p. 165–194, 1997. Cited 4 times on pages 2, 3, 53, and 55.
- Li, Z.; Ito, K. The Immersed Interface Method: Numerical Solutions of PDEs Involving Interfaces and Irregular Domains (Frontiers in Applied Mathematics). USA: Society for Industrial and Applied Mathematics, 2006. ISBN 0898716098. Cited 2 times on pages 4 and 54.
- Liang, X. et al. Dynamic interfacial tension and adsorption kinetics of nonionic surfactants during microfluidic droplet formation process. *Chemical Engineering Journal*, v. 445, p. 136658, 2022. ISSN 1385-8947. Available on: https://www.sciencedirect.com/science/article/pii/S1385894722021532. Cited on page 3.
- Lin, S.-Y.; McKeigue, K.; Maldarelli, C. Diffusion-controlled surfactant adsorption studied by pendant drop digitization. *AIChE Journal*, v. 36, n. 12, p. 1785–1795, 1990. Available on: https://aiche.onlinelibrary.wiley.com/doi/abs/10.1002/aic.690361202. Cited on page 2.
- Lin, S.-Y.; McKeigue, K.; Maldarelli, C. Effect of cohesive energies between adsorbed molecules on surfactant exchange processes: Shifting from diffusion control for adsorption to kinetic-diffusive control for re-equilibration. *Langmuir*, v. 10, n. 10, p. 3442–3448, 1994. Available on: https://doi.org/10.1021/la00022a014. Cited on page 2.
- Lin, Y.; Skjetne, P.; Carlson, A. Numerical simulation of drop deformation in electric fields using a front-tracking method. *International Journal of Multiphase Flow*, v. 45, p. 1–11, 2012. Cited on page 7.
- Liu, X.-D.; Fedkiw, R. P.; Kang, M. A boundary condition capturing method for poisson's equation on irregular domains. *Journal of Computational Physics*, v. 160, n. 1, p. 151–178, 2000. ISSN 0021-9991. Available on: https://www.sciencedirect.com/science/article/pii/S0021999100964441. Cited 2 times on pages 33 and 35.
- Luo, K. et al. Numerical analysis of two-phase electrohydrodynamic flows in the presence of surface charge convection. *Physics of Fluids*, v. 32, n. 12, p. 123606, 12 2020. ISSN 1070-6631. Available on: https://doi.org/10.1063/5.0028635. Cited 2 times on pages 75 and 76.
- MacLeod, C.; Radke, C. J. Charge effects in the transient adsorption of ionic surfactants at fluid interfaces. Oct 1994. Cited on page 2.

- Masliyah, J. H.; Bhattacharjee, S. *Electrokinetic and Colloid Transport Phenomena*. : John Wiley & Sons, 2006. ISBN 9780471788829. Cited 2 times on pages 14 and 16.
- Mason, T. et al. Nanoemulsions: formation, structure, and physical properties. *Journal of Physics: Condensed Matter*, IOP Publishing, v. 8, n. 41, p. 9339–9366, 1996. Cited on page 1.
- McClements, D. Food Emulsions: Principles, Practices, and Techniques. : CRC Press, 2015. Cited on page 1.
- Melcher, J. R.; Taylor, G. I. Electrohydrodynamics: A review of the role of interfacial shear stresses. *Ann. Rev. Fluid Mech. 1: 111-46(1969).*, 1 1969. Available on: https://www.osti.gov/biblio/4731123. Cited 2 times on pages 6 and 22.
- Miller, R. et al. Dynamic surface tension and adsorption kinetics of beta-case at the solution/air interface. *Langmuir*: the ACS journal of surfaces and colloids, v. 20, p. 771–7, 03 2004. Cited on page 2.
- Miller, R.; Joos, P.; Fainerman, V. B. Dynamic surface and interfacial tensions of surfactant and polymer solutions. *Advances in Colloid and Interface Science*, v. 49, p. 249–302, 1994. ISSN 0001-8686. Available on: https://www.sciencedirect.com/science/article/pii/0001868694800170. Cited on page 2.
- Mora, J. F. de la. The fluid dynamics of taylor cone. *Annual Review of Fluid Mechanics*, v. 32, p. 265–297, 2000. Cited on page 5.
- Mori, Y.; Young, Y.-N. Electrohydrodynamics of leaky dielectrics as the weak electrolyte limit of an electrodiffusion model. *Journal of Fluid Mechanics*, v. 855, p. 67–130, 2018. Cited on page 7.
- Muradoglu, M.; Tryggvason, G. Simulations of soluble surfactants in 3d multiphase flow. *Journal of Computational Physics*, v. 274, p. 737–757, 10 2014. Cited on page 4.
- Osher, S.; Fedkiw, R. *The Level Set Methods and Dynamic Implicit Surfaces*. 2004. v. 57. xiv+273 p. ISBN 0-387-95482-1. Cited 2 times on pages 31 and 43.
- Paknemat, H.; Pishevar, A.; Pournaderi, P. Numerical simulation of drop deformations and breakup modes caused by direct current electric fields. *Physics of Fluids*, v. 24, 10 2012. Cited on page 8.
- Pal, A. Numerical Analysis. 2007. Course material. Department of Mathematics, National Institute of Technology Durgapur. Cited on page 26.
- Pan, R.; Green, J.; Maldarelli, C. Theory and experiment on the measurement of kinetic rate constants for surfactant exchange at an air/water interface. *Journal of Colloid and Interface Science*, v. 205, n. 2, p. 213–230, 1998. ISSN 0021-9797. Available on: https://www.sciencedirect.com/science/article/pii/S002197979895559X. Cited on page 2.
- Peng, D. et al. A pde-based fast local level set method. *Journal of Computational Physics*, v. 155, n. 2, p. 410–438, 1999. ISSN 0021-9991. Available on: https://www.sciencedirect.com/science/article/pii/S0021999199963453. Cited on page 30.
- Peng, G. G. et al. Equatorial blowup and polar caps in drop electrohydrodynamics. *Phys. Rev. Fluids*, American Physical Society, v. 9, p. 083701, Aug 2024. Available on: https://link.aps.org/doi/10.1103/PhysRevFluids.9.083701. Cited 2 times on pages 7 and 79.

- Petras, A.; Ruuth, S. Pdes on moving surfaces via the closest point method and a modified grid based particle method. *Journal of Computational Physics*, v. 312, 02 2016. Cited on page 4.
- Phan, C. Dissociation of ionic surfactants at air/water interface: Complete or partial? *The Journal of Physical Chemistry B*, v. 120, 07 2016. Cited on page 3.
- Pimenta, P.; Oliveira, T. Study on the rheology of a dilute emulsion of surfactant-covered droplets using the level set and closest point methods. *Physics of Fluids*, v. 33, p. 103306, 10 2021. Cited on page 4.
- Pimenta, P. H. N. Rheology and magnetization of dilute emulsions of surfactant-covered ferrofluid droplets. Tese de Doutorado em Ciências Mecânicas Universidade de Brasília (UnB), Brasília, DF, Brasil, 2023. Cited 2 times on pages ix and 51.
- Pohl, H. A. Dielectrophoresis: The Behavior of Neutral Matter in Nonuniform Electric Fields.: Cambridge University Press, 1978. Cited on page 5.
- Qazi, M. J. et al. Dynamic surface tension of surfactants in the presence of high salt concentrations. *Langmuir*, v. 36, n. 27, p. 7956–7964, 2020. PMID: 32545966. Available on: https://doi.org/10.1021/acs.langmuir.0c01211. Cited 2 times on pages 1 and 3.
- Quincke, G. Ueber rotationen im constanten electrischen felde. *Annalen der Physik*, v. 295, p. 417 486, 03 1896. Cited on page 80.
- Riechers, B. et al. Surfactant adsorption kinetics in microfluidics. *Proceedings of the National Academy of Sciences*, v. 113, n. 41, p. 11465–11470, 2016. Available on: https://www.pnas.org/doi/abs/10.1073/pnas.1604307113. Cited on page 3.
- Rosen, M. Surfactants and Interfacial Phenomena. 3rd. ed.: Wiley, 2004. Cited on page
- Ruuth, S.; Merriman, B. A simple embedding method for solving partial differential equations on surfaces. *Journal of Computational Physics*, v. 227, p. 1943–1961, 01 2008. Cited 4 times on pages 4, 31, 33, and 48.
- Salager, J.-L. Recent advances in oil/water emulsions. Current Opinion in Colloid & Interface Science, Elsevier, v. 7, n. 3–4, p. 275–286, 2002. Cited on page 1.
- Salipante, P. F.; Vlahovska, P. M. Electrohydrodynamics of drops in strong uniform dc electric fields. *Physics of Fluids*, v. 22, n. 11, p. 112110, 11 2010. ISSN 1070-6631. Available on: https://doi.org/10.1063/1.3507919. Cited 6 times on pages xi, xii, 7, 83, 84, and 85.
- Saville, D. A. Electrohydrodynamic stability: effects of charge relaxation at the interface of a liquid jet. *Journal of Fluid Mechanics*, v. 48, p. 815–827, 1971. Cited on page 6.
- Saville, D. A. Electrohydrodynamics: The taylor-melcher leaky dielectric model. *Annual Review of Fluid Mechanics*, v. 29, p. 27–64, 1997. Cited on page 23.
- Sengupta, S.; Walker, L. M.; Khair, A. S. The role of surface charge convection in the electrohydrodynamics and breakup of prolate drops. 2017. Cited 2 times on pages 7 and 8.
- Shinoda, K. et al. *Colloidal Surfactants*. New York and London: Academic Press, 1963. 319 p. Cited on page 2.

- Shu, C.-W.; Osher, S. Efficient implementation of essentially non-oscillatory shock-capturing schemes. *Journal of Computational Physics*, v. 77, n. 2, p. 439–471, 1988. ISSN 0021-9991. Available on: https://www.sciencedirect.com/science/article/pii/0021999188901775. Cited on page 31.
- Slattery, J.; Sagis, L.; Oh, E. *Interfacial Transport Phenomena (Second edition)*. Germany: Springer, 2007. F832. ISBN 9780387384382. Cited on page 102.
- Solans, C. et al. Nano-emulsions. Current Opinion in Colloid & Interface Science, Elsevier, v. 10, n. 3–4, p. 102–110, 2005. Cited on page 1.
- Sorgentone, C.; Tornberg, A.-K. A highly accurate boundary integral equation method for surfactant-laden drops in 3d. *Journal of Computational Physics*, v. 360, 07 2017. Cited on page 4.
- Sorgentone, C.; Vlahovska, P. M. Numerical and asymptotic analysis of the three-dimensional electrohydrodynamic interactions of drop pairs. *Journal of Fluid Mechanics*, v. 914, p. A24, 2021. Cited on page 8.
- Stone, H. A. A simple derivation of the time-dependent convective-diffusion equation for surfactant transport along a deforming interface. *Physics of Fluids A: Fluid Dynamics*, v. 2, n. 1, p. 111–112, 01 1990. ISSN 0899-8213. Available on: https://doi.org/10.1063/1.857686. Cited on page 2.
- Sussman, M.; Fatemi, E. An efficient, interface preserving level set re-distancing algorithm and its application to interfacial incompressible fluid flow. *SIAM Journal on Scientific Computing*, v. 20, 02 1999. Cited on page 30.
- Sussman, M.; Smereka, P.; Osher, S. A level set approach for computing solutions to incompressible two-phase flow. *Journal of Computational Physics*, v. 114, n. 1, p. 146–159, 1994. ISSN 0021-9991. Available on: https://www.sciencedirect.com/science/article/pii/S0021999184711557. Cited on page 29.
- Taylor, G. I. Disintegration of water drops in an electric field. *Proceedings of the Royal Society of London. Series A. Mathematical and Physical Sciences*, v. 280, p. 383–397, 1964. Cited on page 6.
- Taylor, G. I. Studies in electrohydrodynamics. i. the circulation produced in a drop by electrical field. *Proceedings of the Royal Society of London. Series A. Mathematical and Physical Sciences*, v. 291, p. 159–166, 1966. Cited 2 times on pages 6 and 75.
- Taylor, G. I. S. The formation of emulsions in definable fields of flow. *Proceedings of The Royal Society A: Mathematical, Physical and Engineering Sciences*, v. 146, p. 501–523, 1934. Cited on page 50.
- Tcholakova, S. et al. Adsorption kinetics of ionic surfactants: Influence of counterions. *Langmuir*, American Chemical Society, v. 24, n. 2, p. 705–711, 2008. Cited on page 1.
- Tomar, G. et al. Two-phase electrohydrodynamic simulations using a volume-of-fluid approach. *Journal of Computational Physics*, v. 227, p. 1267–1285, 2007. Cited on page 6.
- Torza, S.; Cox, R. G.; Mason, S. G. Electrohydrodynamic deformation and burst of liquid drops. *Philosophical Transactions of the Royal Society of London. Series A, Mathematical and Physical Sciences*, v. 269, p. 295–319, 1971. Cited on page 6.

- Tsukada, T. et al. Theoretical and experimental studies of circulations inside and outside a deformed drop under a uniform electric field. *Journal of Chemical Engineering of Japan*, v. 26, p. 698–703, 1993. Cited on page 6.
- Vizika, O.; Saville, D. A. The electrohydrodynamic deformation of drops suspended in liquids in steady and oscillatory electric fields. *Journal of Fluid Mechanics*, v. 239, p. 1–21, 1992. Cited on page 6.
- Vlahovska, P.; Loewenberg, M. Deformation of a surfactant-covered drop in a linear flow. *Physics of Fluids*, v. 17, 10 2005. Cited on page 3.
- Vlahovska, P. M. Electrohydrodynamics of drops and vesicles. *Annual Review of Fluid Mechanics*, v. 51, p. 305–330, 2019. Cited on page 7.
- Ward, A.; Tordai, L. Existence of time-dependence for interfacial tension of solutions. *Nature*, v. 154, p. 146–147, 1944. Cited on page 1.
- Xie, Z. et al. Self-propulsion of a quincke droplet on a superhydrophobic wall under low electric reynolds number ree *le* 1. *Physics of Fluids*, v. 36, p. 087131, 2024. Cited on page 8.
- Xu, J.; Shi, W.; Lai, M.-C. A level-set method for two-phase flows with soluble surfactant. *Journal of Computational Physics*, v. 353, 10 2017. Cited on page 4.
- Xu, J.-J. et al. A level-set method for interfacial flows with surfactant. *Journal of Computational Physics*, v. 212, p. 590–616, 03 2006. Cited on page 4.
- Xu, J.-J.; Yang, Y.; Lowengrub, J. A level-set continuum method for two-phase flows with insoluble surfactant. *Journal of Computational Physics*, v. 231, n. 17, p. 5897–5909, 2012. ISSN 0021-9991. Available on: https://www.sciencedirect.com/science/article/pii/S0021999112002562. Cited 4 times on pages 4, 41, 54, and 63.
- Xu, J.-J.; Yang, Y.; Lowengrub, J. A level-set continuum method for two-phase flows with insoluble surfactant. *Journal of Computational Physics*, v. 231, n. 17, p. 5897–5909, 2012. ISSN 0021-9991. Available on: https://www.sciencedirect.com/science/article/pii/S0021999112002562. Cited on page 53.
- Xu, J.-J.; Zhao, H.-k. An eulerian formulation for solving partial differential equations along a moving interface. *Journal of Scientific Computing*, v. 19, 02 2003. Cited 2 times on pages 4 and 48.
- Xu, S. An iterative two-fluid pressure solver based on the immersed interface method. *Communications in Computational Physics*, v. 12, n. 2, p. 528–543, 2012. Cited on page 43.
- Young, T. An essay on the cohesion of fluids. *Philosophical Transactions of the Royal Society of London*, v. 95, p. 65–87, 1805. Cited on page 1.

Appendix

A First derivative using central finite difference

The central derivative can be obtained by using writing the *shift* operator in terms of the central difference operator:

$$\Delta_0 = \xi^{1/2} - \xi^{-1/2} \quad \to \quad \xi = \left(\frac{1}{2}\Delta_0 + \sqrt{\mathcal{I} + \frac{1}{4}\Delta_0^2}\right)^2.$$
(A.1)

The differential operator, then, becomes

$$\mathcal{D} = \frac{1}{\Delta x} \ln \left(\frac{1}{2} \Delta_0 + \sqrt{\mathcal{I} + \frac{1}{4} \Delta_0^2} \right)^2. \tag{A.2}$$

Expanding the term $\sqrt{\mathcal{I} + \frac{1}{4}\Delta_0^2}$ in its Taylor's series at $\Delta_0 \to 0$:

$$\sqrt{\mathcal{I} + \frac{1}{4}\Delta_0^2} = 1 + \frac{1}{8}\Delta_0^2 + \mathcal{O}(\Delta_0^4). \tag{A.3}$$

Substituing Eq. (A.3) in Eq. (A.2), it gives

$$\mathcal{D} = \frac{2}{\Delta x} \ln \left(\frac{1}{2} \Delta_0 + 1 + \frac{1}{8} \Delta_0^2 + \mathcal{O}(\Delta_0^4) \right). \tag{A.4}$$

Expanding the natural logarithm $\ln \left(1 + \left[\frac{1}{2}\Delta_0 + \frac{1}{8}\Delta_0^2 + \mathcal{O}(\Delta_0^4)\right]\right)$ at $\Delta_0 \to 0$:

$$\mathcal{D} = \frac{2}{\Delta x} \left[\frac{1}{2} \Delta_0 + \frac{1}{8} \Delta_0^2 + \mathcal{O}(\Delta_0^4) - \frac{\left(\frac{1}{2} \Delta_0 + \frac{1}{8} \Delta_0^2 + \mathcal{O}(\Delta_0^4)\right)^2}{2} + \mathcal{O}(\Delta_0^3) \right]$$

$$= \frac{2}{\Delta x} \left[\frac{1}{2} \Delta_0 + \frac{1}{8} \Delta_0^2 - \frac{1}{8} \Delta_0^2 + \mathcal{O}(\Delta_0^3) \right]$$

$$= \frac{\Delta_0}{\Delta x} + \mathcal{O}(\Delta x^2). \tag{A.5}$$

Applying the operator in Eq. (A.5) in the sequence defined by $f(x_i)$, it gives

$$Df(x_i) = f'(x_i) = \frac{\Delta_0 z_i}{\Delta x^2} + \mathcal{O}(\Delta x^2) = \frac{z_{i+1/2} - z_{i-1/2}}{\Delta x} + \mathcal{O}(\Delta x^2)$$
(A.6)

As $f(x_i)$ is not defined at $x_{i+1/2}$ or $x_{i-1/2}$, a central finite difference approximation can be written as

$$f'(x_i) = \frac{z_{i+1} - z_{i-1}}{2\Delta x} + \mathcal{O}(\Delta x^2)$$
 (A.7)

without losing the order accuracy.

B Second derivative using central finite difference

Taking the square of Eq. (A.5), it gives a second derivative differential operator:

$$\mathcal{D}^{2} = \left[\frac{\Delta_{0}}{\Delta x} + \mathcal{O}(\Delta x^{2})\right]^{2}$$

$$= \frac{\Delta_{0}^{2}}{\Delta x^{2}} + \mathcal{O}(\Delta x^{2}). \tag{B.1}$$

Applying the operator in Eq. (B.1) in the sequence defined by $f(x_i)$, it gives

$$\mathcal{D}^{2}f(x_{i}) = f''(x_{i}) = \Delta_{0} \left(\frac{z_{i+1/2} - z_{i-1/2}}{\Delta x^{2}}\right) + \mathcal{O}(\Delta x^{2})$$

$$= \frac{\Delta_{0}z_{i+1/2} - \Delta_{0}z_{i-1/2}}{\Delta x^{2}} + \mathcal{O}(\Delta x^{2})$$

$$= \frac{z_{i+1} - z_{i} - z_{i} + z_{i-1}}{\Delta x} + \mathcal{O}(\Delta x^{2})$$

$$f''(x_{i}) = \frac{z_{i+1} - 2z_{i} + z_{i-1}}{\Delta x} + \mathcal{O}(\Delta x^{2}).$$
(B.2)

C Derivation of surfactant transport equation

The derivation of the surfactant transport equation can be continued from the mass balance in Eq. (2.27). Developing the left-side of it:

$$\int_{S} \left[\frac{\partial c}{\partial t} + \nabla_{s} \cdot (c\mathbf{u}) \right] dS = -\oint_{C} \hat{\mathbf{b}} \cdot \left[-D_{s} \nabla_{s} c + \frac{D_{s} z e}{k_{B} T} c \mathbf{E}_{s} \right] d\Gamma. \tag{C.1}$$

Using the surface divergence theorem (Slattery; Sagis; Oh, 2007):

$$\oint_C \mathbf{F} \cdot \hat{\mathbf{b}} d\Gamma = \int_S \nabla_s \cdot \mathbf{F} dS, \tag{C.2}$$

where $\mathbf{F} = \left[-D_s \nabla_s c + \frac{D_s ze}{k_B T} c \mathbf{E} \right]$. Then,

$$\int_{S} \left[\frac{\partial c}{\partial t} + \nabla_{s} \cdot (c\mathbf{u}) \right] dS = -\int_{S} \nabla_{s} \cdot \left[-D_{s} \nabla_{s} c + \frac{D_{s} z e}{k_{B} T} c \mathbf{E}_{s} \right] dS \tag{C.3}$$

Applying the Localization Theorem,

$$\frac{\partial c}{\partial t} + \nabla_s \cdot (c\mathbf{u}) = \nabla_s \cdot \left(D_s \nabla_s c - \frac{D_s z e}{k_B T} c \mathbf{E}_s \right). \tag{C.4}$$

D Droplet elongation prediction

To obtain a relation for droplet elongation, let assume that all charges are concentrated as two point charges at the tips, each with Q/2, where Q is the total electric charge as visualized in Fig. 50.

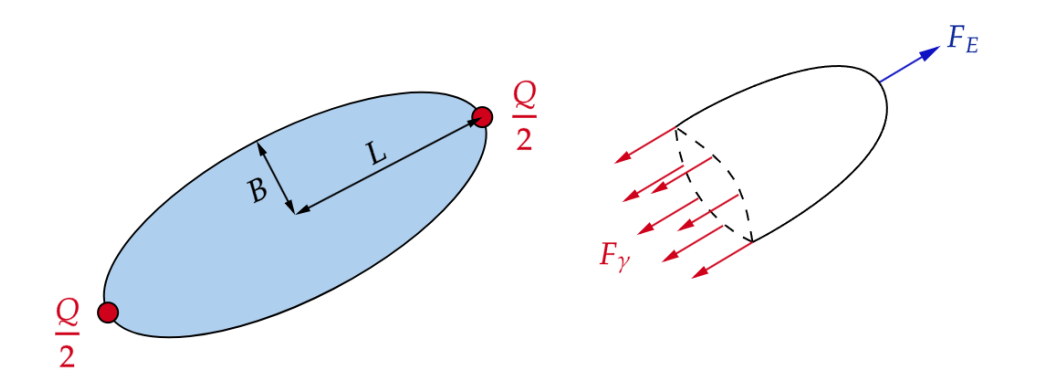


Figure 50 – Schematic representation of the droplet model under elongation, where the total electric charge Q is assumed to be concentrated as two point charges at the tips, each with Q/2. The resulting electric force is modeled as a Coulombic interaction between the charges.

The only force balance that arises from this simplified model is between the capillary force and the electric (Coulomb) force, yielding the expression:

$$2\pi\gamma_0 B = \frac{Q^2}{64\epsilon_0 L^2}. (D.1)$$

Since the balance involves capillary resistance competing with electrostatic effects, it is natural to consider the role of the *Capillary number* (Ca) and the *Mason number* (Mn). To explore this, we compute the ratio between them:

$$\frac{\text{Ca}}{\text{Mn}} = \frac{\mu_o \dot{\gamma} a}{\gamma_0} \cdot \frac{z_1^2 F^2 c_0^2}{\epsilon_0 \mu_o \dot{\gamma}}.$$
 (D.2)

Recognizing that the reference surface charge density is defined as

$$q_{s,0} = z_1^2 F^2 c_0^2, (D.3)$$

the expression simplifies to:

$$\frac{\text{Ca}}{\text{Mn}} = \frac{q_{s,0}^2 a}{\gamma_0 \epsilon_0}.$$
 (D.4)

The total electric charge Q is related to $q_{s,0}$ by:

$$q_{s,0} = \frac{Q}{4\pi a^2}.$$
 (D.5)

Substituting into the previous expression, we obtain:

$$\frac{\text{Ca}}{\text{Mn}} = \frac{Q^2}{16\pi^2 a^3 \gamma_0 \epsilon_0},\tag{D.6}$$

which can be rearranged as:

$$\frac{Q^2}{\gamma_0 \epsilon_0} = 16\pi^2 a^3 \frac{\text{Ca}}{\text{Mn}}.$$
 (D.7)

Next, we manipulate Eq. (D.1) algebraically:

$$BL^2 = \frac{Q^2}{128\pi\epsilon_0\gamma_0}. (D.8)$$

Substituting Eq. (D.7) into Eq. (D.8), we find:

$$BL^{2} = \frac{1}{128\pi^{2}} \cdot 16\pi^{2}a^{3} \frac{\mathrm{Ca}}{\mathrm{Mn}}$$

$$= \frac{1}{8}a^{3} \frac{\mathrm{Ca}}{\mathrm{Mn}}.$$
(D.9)

Since the droplet volume is conserved, the volume of the deformed (ellipsoidal) droplet must equal that of the original sphere. Assuming axisymmetry ellipsoid:

$$\frac{4}{3}\pi a^3 = \frac{4}{3}\pi L B^2 \quad \Rightarrow \quad a^3 = L B^2. \tag{D.10}$$

Substituting this into Eq. (D.9) gives:

$$BL^{2} = \frac{1}{8}LB^{2}\frac{\text{Ca}}{\text{Mn}}$$

$$L = \frac{1}{8}B\frac{\text{Ca}}{\text{Mn}}.$$
(D.11)

Therefore, the droplet elongation ratio is:

$$\frac{L}{B} = \frac{1}{8} \frac{\text{Ca}}{\text{Mn}},\tag{D.12}$$

indicating that the droplet elongates indefinitely as Mn decreases, due to the dominance of electrostatic forces over surface tension.

E Derivation of surface charge transport equation

Starting from the volumetric charge transport equation, one can proceed to evaluate the right-hand side of Eq. (3.6):

$$\nabla \cdot (\sigma \mathbf{E}) = \sigma \nabla \cdot \mathbf{E} + \nabla \sigma \cdot \mathbf{E}. \tag{E.1}$$

The Gauss's Law is invoked to obtain the divergence of the electric field as follows:

$$\nabla \cdot (\epsilon \mathbf{E}) = q_v$$

$$\epsilon \nabla \cdot \mathbf{E} + \nabla \epsilon \cdot \mathbf{E} = q_v$$

$$\nabla \cdot \mathbf{E} = \frac{q_v - \nabla \epsilon \cdot \mathbf{E}}{\epsilon}.$$
(E.2)

Substituing Eq. (E.2) in Eq. (E.1), it gives

$$\nabla \cdot (\sigma \mathbf{E}) = \sigma \left[\frac{q_v - \nabla \epsilon \cdot \mathbf{E}}{\epsilon} \right] + \nabla \sigma \cdot \mathbf{E}. \tag{E.3}$$

The gradient of dielectric permittivity and electric conductivity can be obtained by taking the gradient of the smoothed functions of material properties in Eq. (4.14) that gives

$$\nabla \epsilon = (\epsilon_o - \epsilon_i) \nabla H_{\varepsilon}(\phi)$$

$$\nabla \epsilon = (\epsilon_o - \epsilon_i) \frac{dH_{\varepsilon}(\phi)}{d\phi} \nabla \phi.$$
(E.4)

The derivative $\frac{dH_{\varepsilon}(\phi)}{d\phi}$ is precisely the smoothed Dirac delta and $\nabla \phi = \mathbf{n}|\nabla \phi|$, then

$$\nabla \epsilon = (\epsilon_o - \epsilon_i) \delta_{\varepsilon}(\phi) |\nabla \phi| \mathbf{n}$$
 (E.5)

and

$$\nabla \sigma = (\sigma_o - \sigma_i) \delta_{\varepsilon}(\phi) |\nabla \phi| \mathbf{n}. \tag{E.6}$$

Substituing Eqs. (E.5) and (E.6) in Eq. (E.3), the ohmic term can be written as:

$$\nabla \cdot (\sigma \mathbf{E}) = \frac{\sigma}{\epsilon} \left[q_v - (\epsilon_o - \epsilon_i) \delta_{\varepsilon}(\phi) | \nabla \phi | \mathbf{E} \cdot \mathbf{n} \right] + (\sigma_o - \sigma_i) \delta_{\varepsilon}(\phi) | \nabla \phi | \mathbf{E} \cdot \mathbf{n}.$$
 (E.7)

Substituting Eq. (E.7) into the right-hand side of Eq. (3.6), it gives:

$$\frac{\partial q_v}{\partial t} + \nabla \cdot (q_v \mathbf{u}) = \frac{\sigma}{\epsilon} \left[(\epsilon_o - \epsilon_i) \delta_{\varepsilon}(\phi) | \nabla \phi | \mathbf{E} \cdot \mathbf{n} - q_v \right] + (\sigma_o - \sigma_i) \delta_{\varepsilon}(\phi) | \nabla \phi | \mathbf{E} \cdot \mathbf{n}.$$
 (E.8)

Using the definition of the Dirac delta distribution, q_v is written in terms of q_s using Eq. (4.65). Thus, Eq. (E.8) becomes

$$\frac{\partial q_s}{\partial t} \delta_{\varepsilon}(\phi) |\nabla \phi| + \nabla \cdot (q_s \mathbf{u}) \delta_{\varepsilon}(\phi) |\nabla \phi| = -\left\{ \frac{\sigma}{\epsilon} \left[q_s - (\epsilon_o - \epsilon_i) \mathbf{E} \cdot \mathbf{n} \right] + (\sigma_o - \sigma_i) \mathbf{E} \cdot \mathbf{n} \right\} \delta_{\varepsilon}(\phi) |\nabla \phi|.$$
(E.9)

Dividing both sides by $\delta_{\varepsilon}(\phi)|\nabla\phi|$, it gives

$$\frac{\partial q_s}{\partial t} + \nabla \cdot (q_s \mathbf{u}) = -\left\{ \frac{\sigma}{\epsilon} \left[q_s - (\epsilon_o - \epsilon_i) \mathbf{E} \cdot \mathbf{n} \right] + (\sigma_o - \sigma_i) \mathbf{E} \cdot \mathbf{n} \right\}.$$
 (E.10)

As q_s is only defined on the interface, Eq. (E.10) should be solved only on the interface, i.e., $\forall \mathbf{x} \in \Gamma$, then all quantities are evaluated at the interface. Hence,

$$\frac{\partial q_s}{\partial t} + \nabla_s \cdot (q_s \mathbf{u}) = \frac{\sigma_s}{\epsilon_s} \left[(\epsilon_o - \epsilon_i) \mathbf{E}_s \cdot \mathbf{n} - q_s \right] + (\sigma_i - \sigma_o) \mathbf{E}_s \cdot \mathbf{n}. \tag{E.11}$$

F Derivation of Frumkin-Davies isotherm model for interfacial tension

Consider the Gibbs adsorption equation in the form of

$$\Gamma = -\frac{1}{nRT} \frac{\partial \gamma}{\partial (\ln C)}.$$
 (F.1)

This is a pseudo-PDE which can be solved separating it:

$$d\gamma = -nRT\Gamma d(\ln C). \tag{F.2}$$

In equilibrium, the relation between the surfactant coverage Γ and the bulk surfactant concentration C can be obtained by the Frumkin-Davies isotherm relation, which is given by

$$\frac{\Gamma}{\Gamma_{\infty}} = \frac{kC}{kC + \exp\left(\frac{K\Gamma}{\Gamma_{\infty}}\right) \exp\left(-\frac{z_1 F \psi_s}{RT}\right)},\tag{F.3}$$

where

Isolating the bulk surfactant concentration:

$$C = \frac{\exp\left(\frac{K\Gamma}{\Gamma_{\infty}}\right) \exp\left(-\frac{z_1 F \psi_s}{RT}\right)}{k\left(\frac{\Gamma_{\infty}}{\Gamma} - 1\right)}$$
 (F.4)

Taking the natural logarithm on both sides:

$$\ln C = \ln \left[\frac{\exp\left(\frac{K\Gamma}{\Gamma_{\infty}}\right) \exp\left(-\frac{z_1 F \psi_s}{RT}\right)}{k\left(\frac{\Gamma_{\infty}}{\Gamma} - 1\right)} \right]$$

$$= \ln \left[\exp\left(\frac{K\Gamma}{\Gamma_{\infty}}\right) \right] + \ln \left[\exp\left(-\frac{z_1 F \psi_s}{RT}\right) \right] - \ln k - \ln \left(\frac{\Gamma_{\infty}}{\Gamma} - 1\right)$$

$$= \frac{K\Gamma}{\Gamma_{\infty}} - \frac{z_1 F \psi_s}{RT} - \ln k - \ln \left(\frac{\Gamma_{\infty}}{\Gamma} - 1\right)$$
(F.5)

Since differentiation is a linear operator, it is possible to take the differential of $\ln C$ and apply the distributive property on the right-side :

$$d(\ln C) = d \left[\frac{K\Gamma}{\Gamma_{\infty}} - \frac{z_1 F \psi_s}{RT} - \ln k - \ln \left(\frac{\Gamma_{\infty}}{\Gamma} - 1 \right) \right]$$

$$= d \left(\frac{K\Gamma}{\Gamma_{\infty}} \right) - d \left(\frac{z_1 F \psi_s}{RT} \right) - d(\ln k) - d \left[\ln \left(\frac{\Gamma_{\infty}}{\Gamma} - 1 \right) \right]. \tag{F.6}$$

Since K, Γ_{∞} , z_1 , F, R, T, and k are all constants, the expression simplifies to:

$$d(\ln C) = \frac{K}{\Gamma_{\infty}} d\Gamma - \frac{z_1 F}{RT} d\psi_s + \frac{\Gamma_{\infty}}{\Gamma_{\infty} \Gamma - \Gamma^2} d\Gamma$$

$$= \left(\frac{K}{\Gamma_{\infty}} + \frac{\Gamma_{\infty}}{\Gamma_{\infty} \Gamma - \Gamma^2}\right) d\Gamma - \frac{z_1 F}{RT} d\psi_s. \tag{F.7}$$

Substituing Eq. (F.7) in Eq. (F.2):

$$d\gamma = -nRT\Gamma \left[\left(\frac{K}{\Gamma_{\infty}} + \frac{\Gamma_{\infty}}{\Gamma_{\infty}\Gamma - \Gamma^{2}} \right) d\Gamma - \frac{z_{1}F}{RT} d\psi_{s} \right]$$

$$= -nRT \left[\left(\frac{K}{\Gamma_{\infty}}\Gamma + \frac{\Gamma_{\infty}}{\Gamma_{\infty} - \Gamma} \right) d\Gamma - \frac{z_{1}F}{RT} \Gamma d\psi_{s} \right]. \tag{F.8}$$

Integrating both sides and manipulating it:

$$\gamma = -nRT \left[\frac{K}{\Gamma_{\infty}} \int \Gamma d\Gamma + \int \frac{\Gamma_{\infty}}{\Gamma_{\infty} - \Gamma} d\Gamma - \frac{z_1 F}{RT} \int \Gamma d\psi_s \right] + C_1$$

$$= -nRT \left[\frac{K\Gamma^2}{2\Gamma_{\infty}} - \Gamma_{\infty} \ln \left(\Gamma_{\infty} - \Gamma \right) - \frac{z_1 F}{RT} \int \Gamma d\psi_s \right] + C_1$$

$$= -nRT \left\{ \frac{K\Gamma^2}{2\Gamma_{\infty}} \frac{\Gamma_{\infty}}{\Gamma_{\infty}} - \Gamma_{\infty} \ln \left[\frac{\Gamma_{\infty}}{\Gamma_{\infty}} (\Gamma_{\infty} - \Gamma) \right] \right\} - nz_1 F \int \Gamma d\psi_s + C_1$$

$$= -nRT\Gamma_{\infty} \left[\frac{K}{2} \left(\frac{\Gamma}{\Gamma_{\infty}} \right)^2 - \ln \Gamma_{\infty} + \ln \left(1 - \frac{\Gamma}{\Gamma_{\infty}} \right) \right] - nz_1 F \int \Gamma d\psi_s + C_1$$

$$= -nRT\Gamma_{\infty} \left[\frac{K}{2} \left(\frac{\Gamma}{\Gamma_{\infty}} \right)^2 + \ln \left(1 - \frac{\Gamma}{\Gamma_{\infty}} \right) \right] - nz_1 F \int \Gamma d\psi_s + \underbrace{nRT\Gamma_{\infty} \ln \Gamma_{\infty} + C_1}_{C_2}$$

$$(F.9)$$

Rearranging we obtain the Frumkin-Davies isotherm:

$$\gamma = C_2 + nRT\Gamma_{\infty} \left[\ln \left(1 - \frac{\Gamma}{\Gamma_{\infty}} \right) - \frac{K}{2} \left(\frac{\Gamma}{\Gamma_{\infty}} \right)^2 \right] - nz_1 F \int \Gamma d\psi_s$$
 (F.10)

When $\Gamma = 0$ (no surfactant coverage), $\gamma = \gamma_0$:

$$\gamma_0 = C_2 + nRT\Gamma_\infty \ln 1 \to C_2 = \gamma_0. \tag{F.11}$$

On the other hand $q_s=z_1F\Gamma,$ leading to:

$$\gamma = \gamma_0 + nRT\Gamma_{\infty} \left[\ln \left(1 - \frac{\Gamma}{\Gamma_{\infty}} \right) - \frac{K}{2} \left(\frac{\Gamma}{\Gamma_{\infty}} \right)^2 \right] - n \int q_s d\psi_s$$
 (F.12)